Biosensing using long-range surface plasmon-polariton waveguides

By
Oleksiy Krupin

A thesis presented to the
Faculty of Graduate and Postdoctoral Studies
in partial fulfillment of the requirements for the degree of

Doctor of Philosophy in Chemical Engineering

Department of Chemical and Biological Engineering
Faculty of Engineering
University of Ottawa

Abstract

Specific detection of biological matter is one of the key elements in a wide range of modern fields such as food industry, medicine, environmental and pharmaceutical industries. Generally, current common methods of detection (*e.g.* ELISA) involve molecular labelling, requirements for well-trained personnel and lengthy experimental procedures such as bacteria culture. All of the above issues result in high costs for biological analysis, and consequently, high costs for medical service, therapeutic drugs and various food products. Biosensors, on the other hand, can provide quick and cheap solutions to these problems.

The field of optical biosensors is dominated by the method of *surface plasmon resonance*, which so far has attracted a lot of attention in the pharmaceutical industry. Investigation of *long-range* surface plasmon-polariton waveguides as an application for biosensing is still very novel, and most of it exists in the venue of theoretical discussions and modelling. The objective of this thesis is to demonstrate the capability of the novel optical biosensor based on plasmonic waveguides to selectively detect various biological entities in solutions.

The experiments were conducted on photolithographically fabricated sensors consisting of straight gold waveguides embedded in low-refractive index fluoropolymer CYTOP and a microfluidic channel. As a proof-of-concept, a demonstration of basic sensing experiments such as detection of change in refractive index of bulk solution and non-specific adsorption of bovine serum albumin is provided. Further investigation of the sensor capabilities involved specific detection of human red blood cells and leukemia markers. Red blood cell detection was based on ABO blood grouping and included the estimation of limit of detection and signal-to-noise ratio for single cell detection. Finally, a clinically relevant problem of B-cell leukemia marker detection was targeted. The sensor demonstrated the ability to detect the relative abundance of similar proteins (immunoglobulin kappa and lambda) in a complex fluid (human serum). In addition, an experimental study on the optimization of the sensor for sensitivity was conducted.

Acknowledgements

First I would like to express my deepest appreciation to my thesis advisor Dr. Pierre Berini, who let me work on this interesting and complex research topic. His guidance allowed me to complete this work, which at this point in life I can call my greatest achievement. Throughout these years I learned from him a number of general, but yet essential research skills such as research thinking, approach to experimental design, technical writing, oral presentations and many more. I also would like to thank Dr. Pierre Berini for his financial support that helped me complete the project.

I thank my parents, who supported me throughout my doctoral studies, who kept believing in me even during the toughest times of research.

I also would like to express my gratitude to my colleagues: Tony (Anthony) Oliviery, whose expertise in optics and desire to help significantly improved my understanding of lasers and laser equipment, and specifically I thank him for the case when I was stuck with the system instability for several months and his suggestions practically resolved the problem. I am thankful to Michal Tencer who helped me in understanding surface chemistry and electrolysis technique. I thank Ewa Lisicka-Skrzek for the initial training on optical setups, fibre alignment and taking measurements. I thank Israel De Leon for clear explanation of plasmonics fundamentals.

I would also like to thank Hamoudi Asiri and Sa'ad Hassan for manufacturing great quality sensors that allowed me to perform all the biosensing experiments.

I am thankful to Asad Khan, my colleague and friend, who also helped me in initial training on optical setups and getting a general understanding of Labview software.

Finally, I would like to thank all the people who worked in the research laboratory for their friendship, work support and fun times.

Publications

Papers published and accepted in refereed journals (included in the thesis)

O. Krupin, C. Wang, and P. Berini, "Detection of leukemia markers using long-range surface plasmon waveguides functionalized with protein G," *Lab on a Chip*, **15**, 4156-4165 (2015).

W. R. Wong, **O. Krupin**, F. R. M. Adikan, and P. Berini, "Optimization of long-range surface plasmon waveguides for attenuation-based biosensing," *Journal of Lightwave Technology*, **33**(15), 3234-3242 (2015).

O. Krupin, C. Wang, and P. Berini, "Selective capture of human red blood cells based on blood group using long-range surface plasmon waveguides," *Biosensors and Bioelectronics*, **53**, 117-122 (2013).

O. Krupin, H. Asiri, C. Wang, R. N. Tait, and P. Berini, "Biosensing using long-range surface plasmon waveguides," *Optics Express*, **21**, 698-709 (2013).

Book Chapters

O. Krupin and P. Berini, "Long-range plasmonic waveguide sensors" in *Biomedical Optical Sensors:* Springer Publishing Company, Richard M. De La Rue and Hans Peter Herzig, (Submitted). **Invited**.

Collaborative papers published and accepted in refereed journals

P. Beland, **O. Krupin**, and P. Berini, "Selective detection of bacteria in urine with a long-range surface plasmon waveguide biosensor," *Biomedical Optics* Express, **6**(8), 2908-2922 (2015).

W. R. Wong, **O. Krupin**, S. D. Sekaran, F. R. M. Adikan, and P. Berini, "Serological diagnosis of dengue infection in blood plasma using long-range surface plasmon waveguides," *Analytical Chemistry,* **86**, 1735-1743 (2014).

A. Khan, **O. Krupin**, E. Lisicka-Skrzek, and P. Berini, "Mach-Zehnder refractometric sensor using long-range surface plasmon waveguides," *Applied Physics Letters*, **103**, 111108 (1-4) (2013).

M. Tencer, **O. Krupin**, B. Tezel, and P. Berini, "Electrochemistry of Au-SAM-protein stacks," *Journal of the Electrochemistry Society*, **160**, H22-H27 (2012).

Invited papers at refereed conferences

O. Krupin and P. Berini, "Biosensing using long-range surface plasmon-polariton waveguides," *IEEE International Conference on Optical MEMS & Nanophotonics*, Banff, Canada, August 2012.

O. Krupin and P. Berini, "Biosensing using long-range surface plasmon-polariton waveguides," *SPIE Photonics North: Bio-Sensors*, Montréal, Canada, June 2012.

O. Krupin and P. Berini, "Biosensing using long-range surface plasmon-polaritons, "*Meta 2012–3rd International Conference on Metamaterials, Photonic Crystals and Plasmonics: Plasmonics and nanophotonics for sensing, imaging, and spectroscopy*," Paris, France, April 2012.

Papers published and accepted in refereed conferences

O. Krupin, C. Wang, and P. Berini, "Long-range surface plasmon waveguides for leukemia detection," *Photonics North-2015*, Ottawa, Canada, June 2015.

O. Krupin, C. Wang, and P. Berini, "Strategies for leukemic biomarker detection using long-range surface plasmon-polaritons," *Photonics North-2014*, Ottawa, Canada, June 2014.

O. Krupin, C. Wang, and P. Berini, "Selective Biosensing using Straight Long-Range Surface Plasmon waveguides," *Photonics North-2013*, Ottawa, Canada, June 2013.

O. Krupin, C. Wang, and P. Berini, "Biosensing using Straight Long-Range Surface Plasmon waveguides,"*6th International Conference on Surface Plasmon Photonics*, Ottawa, Canada, May 2013.

O. Krupin, C. Wang, and P. Berini, "Long-Range Surface Plasmon Polariton (LRSPP) Waveguides as (Bio)Chemical and Biological Sensors," *Nano-ONTARIO Conference-2012*, University of Waterloo, Waterloo, Canada, October 2012.

A. Khan, **O. Krupin**, E. Lisicka-Skrzek, and P. Berini, "Sensing of bacteria immobilised under static conditions using long-range surface plasmon waveguides in Cytop," *SPIE Photonics North-2011*, Ottawa, Canada, May 2011.

O. Krupin, M. Tencer, and P. Berini, "Selective Functionalization of a Surface Plasmon Polariton Mach-Zehnder Interferometer for Biosensing," *93rd Canadian Chemistry Conference*, Toronto, Canada, May 2010.

Acronyms

16-MHA	16-mercaptohexadecanoic acid
Ab	Antibody
AFM	Atomic Force Microscopy
AK	Goat Anti-human Kappa IgG light chain
AL	Goat Anti-human Lambda IgG light chain
BSA	Bovine Serum Albumin
CTC	Circulating Tumor Cell
DDI	Distilled/deionized
DNA	Deoxyribonucleic acid
EDC	N-(3-Dimethylaminopropyl)-N′-ethylcarbodiimide hydrochloride
ELISA	Enzyme-Linked Immunosorbent Assay
Fab	Fragment Antigen Binding site
Fc	Fragment Crystallizable region
Gly	Glycerol
hCG	human Chorionic Gonadotropin
HKS	High Kappa Serum
HLS	High Lambda Serum
HSV	Herpes Simplex Virus
IFE	Immunofixation Electrophoresis
IgG	Immunoglobulin G
IL	Insertion Loss

IMI	Insulator-Metal-Insulator
IPA	2-Isopropanol
IR	Infra-Red
LOD	Limit of Detection
LRSP	Long-Range Surface Plasmon
LRSPP	Long-Range Surface Plasmon Polariton
MPA	Mode Power Attenuation
MZI	Mach-Zehnder Interferometer
MW	Molecular Weight
NHS	N-Hydroxysuccinimide Sodium Salt
NS	Normal Serum
PBS	Phosphate buffer saline
PEG	Polyethylene Glycol
PG	Protein G
PM	Polarization Maintaining
QCM	Quartz Crystal Microbalance
RI	Refractive Index
RIU	Refractive Index Units
RBC	Red Blood Cell
SAM	Self-Assembled Monolayer
SDS	Sodium Dodecyl Sulfate
SPP	Surface Plasmon Polariton
SPR	Surface Plasmon Resonance

SWG Straight Waveguide

TM Transverse Magnetic

TNT 2,4,6-Trinitrotoluene

T-PEG Triethylene glycol mono-11 mercaptoundecyl ether

VEGF Vascular Endothelial Growth Factor

Table of Contents

Abstract ii

Acknowledgments iii

Publications iv

Acronyms vi

Table of Content ix

1. Introduction 1

1.1. Biosensors and biosensing....1

1.2. Optical (plasmonic) biosensors....3

1.2.1. Surface Plasmon Resonance (SPR)....3

1.2.2. Long-Range Surface Plasmon Polariton (LRSPP)....5

1.3. Straight waveguide LRSPP sensor....6

1.3.1. Sensor structure....6

1.3.2. Integration with optics....7

1.3.3. Sensitivity of a straight waveguide sensor....8

1.4. Analyte recognition systems....11

1.5. Surface functionalization strategies....13

1.5.1. Self-assembled monolayer (SAM) approach....14

1.5.2. Protein G approach....15

1.6. Literature Review....16

1.7. Thesis Scope and Outline....21

2. Biosensing using straight LRSPP waveguides (Proof of Concept) 23

2.1. Summary....23

2.2. Contribution....23

2.3. Article....24

2.4. Additional Corrections and Comments....37

3. Detection of human red blood cells using straight LRSPP waveguides 38

3.1. Summary....38

3.2. Contribution....39

3.3. Article....39

4. Detection of leukemia markers in patient serum using LRSPP SWG sensors 50

4.1. Summary....50

4.2. Contribution....51

4.3. Article....51

5. Optimization of LRSPP waveguides for biosensing 72

5.1. Summary....72

5.2. Contribution....72

5.3. Article....73

6. Conclusions 91

6.1. Summary and contributions....91

6.2. Suggestions for future work....93

Bibliography 94

Chapter 1

Introduction

This chapter presents an introduction into biosensing using long-range surface plasmon waveguides. Biosensing is a multidisciplinary field, which combines physics, chemical engineering, chemistry, biochemistry and nanotechnology. Therefore, in order to assist a reader, a brief description of the concepts of biosensing focusing on plasmonic sensors is provided. In addition, the basics of surface functionalization and analyte recognition systems relevant to the work are discussed. Finally, a literature review of the relevant work and thesis scope are presented.

1.1. Biosensors and biosensing

Many fields such as medicine, pharmaceuticals and the food industry to a large extent are dependent on the detection of certain biomolecules in samples as well as investigation of biomolecular interactions. One of the means to target these needs is a *biosensor* - a device that uses specific (bio)chemical interactions to detect a biological entity or analyze these interactions by electrical, thermal or optical signals [1]. Biosensors are becoming more important in a wide range of applications requiring real-time analysis of specific binding phenomena including antigen-antibody, protein-protein, and small molecule-protein interaction, among others.

Figure 1 presents the general principle of biosensing. In order to selectively capture the analyte of interest in the sample, a recognition element is required. A transducer converts this binding process into an electrical signal that can be recorded and analyzed. Generally, the set of recognition system and a transducer is referred to as a *biosensor* [2]. Depending on the application and type of transducer, a large variety of recognition

elements can be used. Three main types of biosensors that are being widely investigated and utilized are electrochemical, optical and piezoelectric sensors.

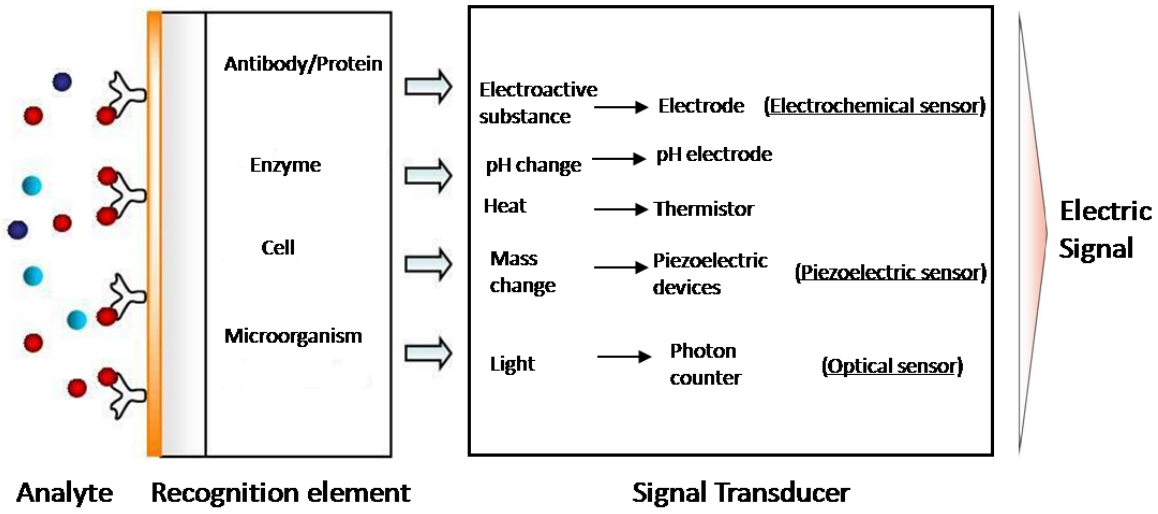

Figure 1. Biosensor operating principle.

Biosensors based on electrochemical transducers are the most common and historically most studied. In fact, the initial development of biosensors originated around 50 years ago with a glucose sensor [3]. Electrochemical biosensors utilize the ability of certain electroactive species to undergo a redox reaction. Consequently, one of the limitations of these sensors is that they are confined to employ enzyme-substrate interaction in order to create an electron transport chain. For example, DNA detection has to be amplified with enzymes such as peroxidases [4].

Optical biosensors have a more recent history and are very attractive for their real-time, label-free and non-destructive detection. In addition, various kinetics studies of biochemical interaction such as association and dissociation constants (Ka and Kd), Gibbs energy activation ($\Delta G^{\ddagger}$), enthalpy activation ($\Delta H^{\ddagger}$) and entropy activation ($\Delta S^{\ddagger}$) can be performed [5]. Optical biosensors primarily utilize the interaction of metal and light, the field called *plasmonics*. The principle of detection is based on the difference of the refractive indices (RI) of water (n~ 1.330) and biological molecules (n~1.5). The reaction occurs at the surface of the functionalized transducer creating changes in the properties of light along which the surface is exposed. The signal change can be further converted into a mass load on the surface, which is related to the concentration of the analyte in the sample. Compared to electrochemical transducers, no enzymatic reaction is required for the optical

transducer; thus it broadens the range of possible biochemical interaction studies. However, the disadvantage of the optical sensor is its sensitivity to the refractive index (RI) of the bulk solution, where a mismatch of RI of pure buffer and solution containing analyte may result in confusing binding curves. Currently, the most common optical sensor is a Surface Plasmon Resonance (SPR) sensor. This work describes optical biosensors based on *long-range surface plasmons* and a more detailed description follows.

Piezoelectric transducers (also called acoustic sensors) are newer than the two described above and also possess great potential in investigating biochemical interactions including kinetics studies. Acoustic waves propagate within the solid, and as material binds, time-dependent deformations of the solid substrate cause changes in the properties of acoustic waves. These changes can be further converted into a mass load on the surface. The most common piezoelectric sensor is a Quartz Crystal Microbalance (QCM), where quartz is employed as an acoustic-sensitive solid [1].

1.2. Optical (plasmonic) biosensors

1.2.1. Surface Plasmon Resonance (SPR)

Electrons in metals are in a quasi-free state, as they are loosely bound to metal atoms, so they can freely move along the metal lattice. These free electrons are responsible for high electric conductivity and high optical reflectivity. At optical frequencies, the behaviour of electrons in metals is very much like that of a gas of free charge carriers (plasma) and can be excited to sustain propagating plasma waves (resonate). Plasma waves are longitudinal electromagnetic charge density waves and their quanta are referred to as *plasmons*. They exist in two forms: *bulk plasmons* in the volume of the metal and *surface plasmons*, which are bound to the interface of the plasma and a dielectric. Surface plasmons exist in many metals including Au, Ag, Al and Cu and can be excited by either electron or light beam [6].

Conventional SPR sensors use a glass prism (Kretschmann-Raether configuration) in order to excite surface plasmons (Fig. 2). At a certain angle (denoted as SPR angle, θ), plasmon excitation occurs and the incident light energy is coupled (transferred) to the surface plasmons thereby decreasing the intensity of the reflected beam. The SPR angle is

determined by the refractive indices of the metal film and the sensing solution, and by the presence of an adlayer at the metal/solution interface. As the thickness of the adlayer changes due to a biochemical interaction, the SPR angle θ changes as well in order to maintain the excitation of surface plasmons. Tracking the change in θ with time leads to a *sensogram* from which binding kinetics can be extracted. Figure 2 demonstrates a typical SPR immunoassay between an antibody and an antigen. This technique has a number of substantial advantages: it is label-free (no need for fluorescence or any other kind of labelling), the detection can be performed in real-time (allows for extraction of kinetics of a bio-interaction) and it requires a low amount of ligand on the surface (*e.g.* costly antibodies). All of these characteristics make SPR technology very appealing for a number of fields that require quick and real-time analysis, in particular for the pharmaceutical sector [7].

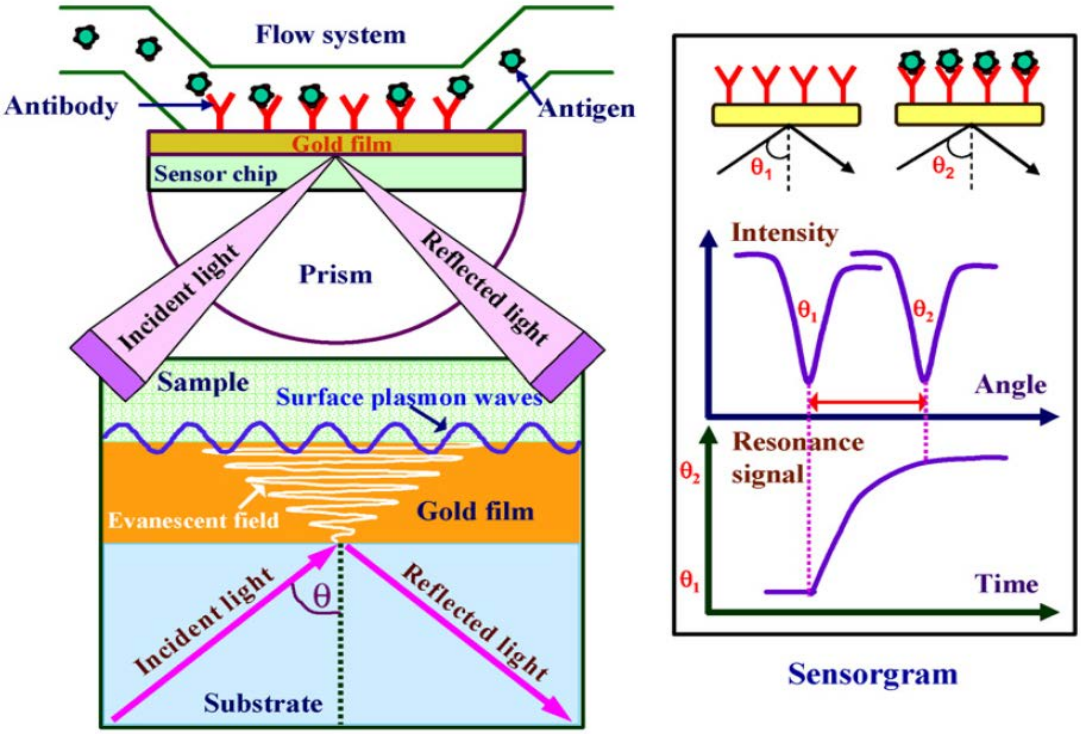

Figure 2. Schematic view of the SPR immunoassay technique. Reproduced with permission from [6], *licence number* 3774911257386.

1.2.2. Long-Range Surface Plasmon Polariton (LRSPP)

LRSPPs are transverse magnetic (TM) surface plasmon waves that can propagate over considerable lengths along a metal slab or stripe bounded by dielectric. The LRSPP is a symmetric mode, which is formed by coupled single-interface surface plasmon polariton waves (SPPs) on the slab or stripe. The mode is confined at the metal-dielectric interfaces in the plane transverse to the direction of propagation, which leads to the possibility of creating various structures such as S-bends, Y-junctions, Mach-Zehnder Interferometers (MZIs) and couplers [8,9].

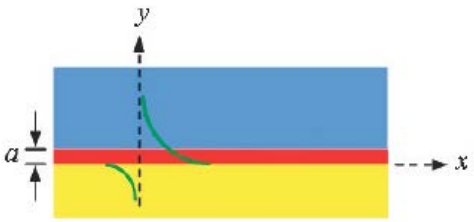

Figure 3. A sketch of a single-interface SPP waveguide.

The simplest SPP waveguide is the single metal-dielectric interface presented in Figure 3, where the SPP on the Au surface (yellow) can be excited using the Kretschmann configuration of Fig. 2. The dielectric adlayer (red) has a thickness *a* and the blue region represents dielectric bulk (sensing solution). As the thickness of the adlayer increases, the characteristics of the SPP wave such as its velocity and attenuation change. The green curves show the distribution of the electric field along the *y* axis. The field decays evanescently into the dielectric region to a distance of about ½ λ (where λ is the excitation wavelength) which defines the probing depth of the wave [10].

The waveguide configuration that is relevant to biosensing using LRSPPs is the insulator-metal-insulator (IMI) structure with a thin metal film of a thickness *t* (Fig. 4a). In this case, two single-interface SPPs couple to create symmetric and asymmetric *supermodes*. Based on theory, the symmetric supermode is sustained over a much longer distance and thus is termed as the *long-range* SPP: the propagation length of the SPP on the single-interface is 82.9 μm, whereas that for the LRSPP on the IMI it is ~2000 μm for the same operating parameters

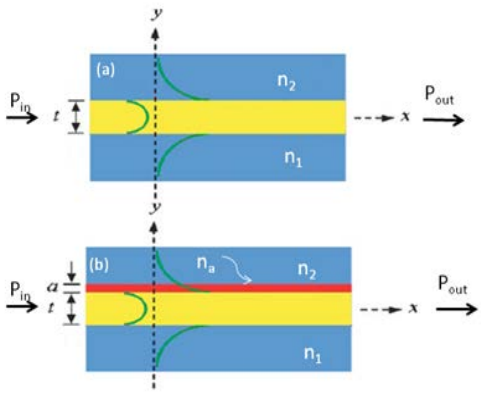

Figure 4. Sketch of Insulator-Metal-Insulator (IMI) 1D surface plasmon waveguides. The waveguides have a thickness *t*. (a) IMI without adlayer, when $n_1 = n_2$ then $P_{out} \approx P_{in}$ (provided negligible inherent attenuation). (b) IMI with adlayer of thickness *a*, if $n_a \neq n_2$ then $P_{out} < P_{in}$.

[10]. The penetration depth of the LRSPP wave is ~2 μm, and is much larger than that of the conventional SPR sensor (~200 nm). The optimum condition for LRSPP propagation on an IMI waveguide is the equal refractive indices of the top and the bottom dielectrics ($n_1 = n_2$). Under these conditions the supermode is undistorted. Presence of an adlayer with a different refractive index (n_a) results in perturbations in the phase and attenuation coefficients of the LRSPP (Fig. 4b). This forms the basis for sensing using LRSPP waveguides.

For sensing purposes, one surface of the waveguide has to be exposed to the surrounding medium, where receptor chemistries would be applied and sensing occurs. Biologically compatible fluids such as phosphate buffered saline (PBS) have a refractive index close to that of water (n~1.330). Thus, for maintaining the RI symmetry around the waveguide, certain considerations for choosing a proper dielectric underneath the stripe have to be taken into account. Generally, dielectric polymers have a much higher RI, and the choice is limited to a few fluoropolymers with low index, such as Teflon (Dupont) or CYTOP (Asahi) [11]. All the biosensing experiments presented in the project were performed with sensors comprising CYTOP (Poly[perfluoro(4-vinyloxy-1-butene)]) as dielectric claddings (Fig. 5).

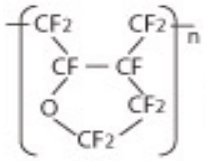

Figure 5. Chemical formula of a CYTOP monomer.

There are a number of different configurations of plasmonic waveguides that could be implemented for biosensing; however this project is involved in testing straight waveguides (SWGs) only.

1.3. Straight waveguide LRSPP sensor

1.3.1. Sensor structure

The sensors are fabricated using photolithography, and the process is described in [12, 13]. After fabrication, the entire wafer (4" diameter) hosting ~300 devices, is covered with dicing photoresist and diced into individual sensors. Each device contains 8 or 16 SWGs (5 μm wide, ~22-35 nm thick Au stripes) embedded in CYTOP (Fig.6). The top cladding of CYTOP is etched down to the Au waveguide level creating a fluidic channel,

where the waveguide surface is exposed to the fluid. The active sensing length of the waveguide is ~1.65 mm.

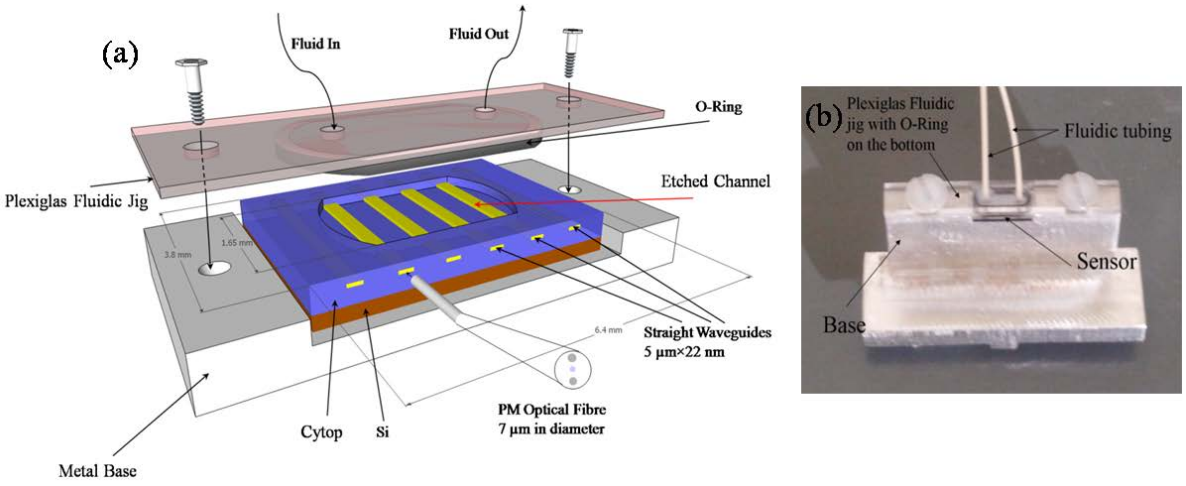

Figure 6. Sensing device with integrated fluidics: a) A schematic diagram of the sensor resting on the metal base, with Plexiglas jig prior to assembly; b) Image of the sensor after integration with fluidics;. Reproduced by permission from [14].

The non-etched (cladded) parts on the ends of the sensing section serve as supports for the integration with fluidics. A custom-made Plexiglas jig with a fluorocarbon O-ring attached to the bottom was designed so that the O-ring rests on the cladded part providing a seal for the fluid in the channel. Tubing is attached to two holes for fluid injection by a syringe pump. The device is integrated into the fluidic cell by placing it onto the custom-made metal base and affixing the Plexiglas jig. The LRSPP wave is generated by butt-coupling a polarization-maintaining (PM) optical fibre to the waveguide at the input facet.

1.3.2. Integration with Optics

The optical setup (Fig.7) includes the light source, which is a diode laser emitting at λ_0 =1310 nm, connected to an optical polarization-maintaining (PM) fibre with a core diameter of 7 µm. The diode parameters (current and temperature) are controlled by a laser diode controller. There are two multi-axis positioning stages that are used in the setup. A six-axis stage is used to hold and manipulate the fibre for alignment to the waveguide. After the device is incorporated into the fluidic cell, it is placed and fixed onto a 3-axis stage. By manipulating the two stages, the fibre is butt-coupled to the waveguide at the

input facet and aligned to produce a maximum output power with lowest background radiation. A 25× collimating lens that is firmly fixed to the optical table is used to approximately collimate the beam exiting the device and to maintain collimation throughout the whole optical path. The syringe pump is setup on the side and provides fluids to the system. An aperture is used to remove background radiation that in some cases can be strong enough to cause either signal instability or mask the sensing event. In order to read the output power and visually monitor the mode quality at the same time, a beam splitter is installed in the optical path, which splits the signal into two parts (~ 50:50). One part enters the power meter, which is connected to the computer and the data is recorded using Labview. The second portion of the output signal enters the infra-red (IR) camera connected to the monitor.

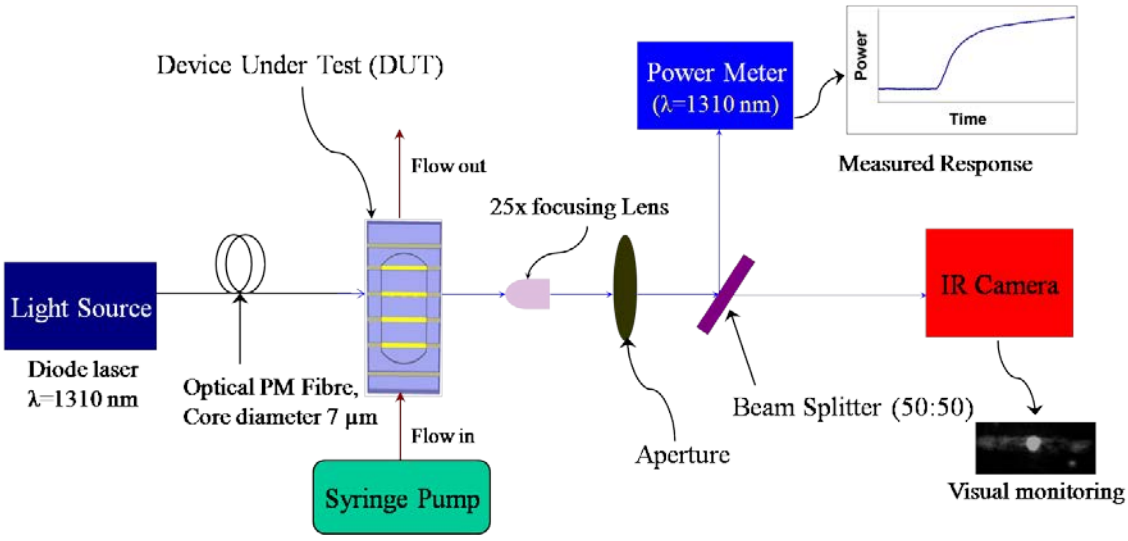

Figure 7. Schematic representation of the optical setup for biosensing using an LRSPP sensor. Reproduced by permission from [14].

1.3.3. Sensitivity of a Straight Waveguide Sensor

A straight waveguide sensor with an etched channel is presented in Figure 8, where L_0 represents the fully cladded part of the waveguide and L is the etched part [15].

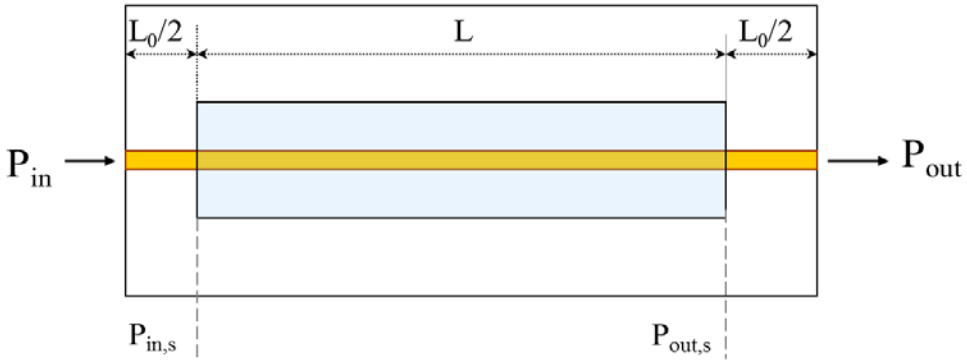

Figure 8. Schematic of the straight plasmonic waveguide embedded in CYTOP with an etched fluidic channel.

The expression that relates the input and output powers is:

$$P_{out} = P_{in} C_i^2 e^{-2\alpha L_0} C^2 e^{-2\alpha_s L} \quad (1)$$

where C_i is a field coupling factor at the input and output facets, C is the cladded waveguide to sensing waveguide field coupling factor, α is the mode field attenuation coefficient on the access lines and α_s is the mode field attenuation coefficient on the sensing section of the length L. α_s and C depend on the thickness *a* of an adlayer that grows on the surface of the metal stripe:

$$P_{out}(a) = P_{in} C_i^2 e^{-2\alpha L_0} C(a)^2 e^{-2\alpha_s(a) L} \quad (2)$$

Relative to reference planes at the fluidic channel:

$$P_{out,s}(a) = P_{in,s} C(a)^2 e^{-2\alpha_s(a) L} \quad (3)$$

A sketch of a typical binding timeline trace is presented in Figure 9.

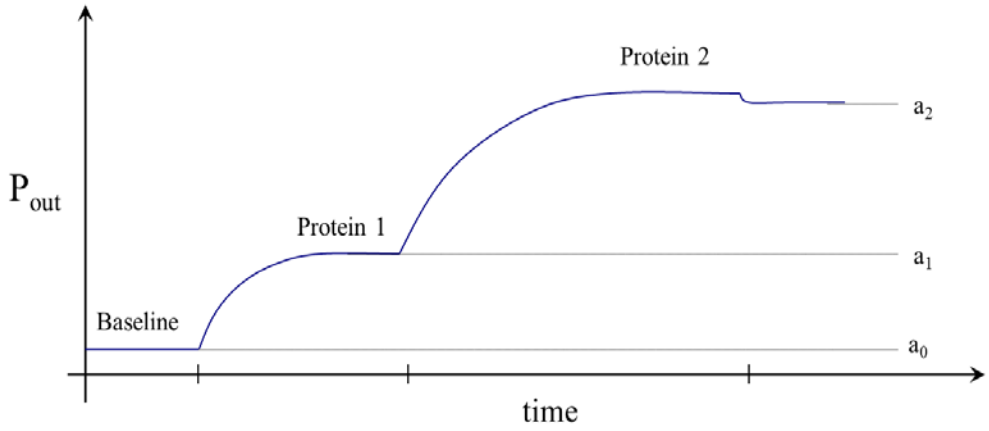

Figure 9. A schematic response of consecutive protein binding on a straight Au waveguide, where a_0 is the adlayer thickness (nm) at the baseline (equal to zero), a_1 is the adlayer thickness (nm) of protein 1 and a_2 is the adlayer thickness (nm) of protein 2.

In Figure 9 the response of protein binding on the waveguide is shown to be positive. However, the response can also be negative and the direction of the response depends on the refractive index of the sensing buffer. The sensing buffer with $n < n_{CYTOP}$ produces positive and $n > n_{CYTOP}$ produces negative responses. More discussion is available in Chapter 5.

ILs(a) is the insertion loss in the sensing channel as a function of adlayer thickness and $\frac{1}{IL(a)}$ varies linearly with adlayer thickness *a* [14]:

$$IL_s(a) = \frac{P_{in,s}}{P_{out,s}(a)} = C(a)^{-2} e^{2\alpha_s(a)L} \simeq \frac{1}{ma+b} \quad \text{for } 0 \leq a \leq 10 \text{ nm} \tag{4}$$

From equation (2), since $P_{in} C_i^2 e^{-2\alpha L_0}$ is constant (k) and $C(a)^2 e^{-2\alpha_s(a)L} \cong (ma + b)$, then

$$P_{out}(a_0) = k(ma_0 + b) \text{ and } P_{out}(a_1) = k(ma_1 + b) \tag{5}$$

From equations (5) $\frac{P_{out}(a_1) - P_{out}(a_0)}{P_{out}(a_0)} = \frac{m(a_1 - a_0)}{ma_0 + b} = \frac{m\Delta a}{ma_0 + b}$, and if we let $\frac{m}{ma_0 + b} = k_2$, then the relationship between changes in adlayer thickness and power changes can be written as:

$$\Delta a = \frac{1}{k_2}\left(\frac{P_{out}(a_1)}{P_{out}(a_0)} - 1\right) \tag{6}$$

The change in surface mass density($\Delta\Gamma, \mathrm{g/m^2}$) can be related to the change in adlayer thickness ($\Delta\mathrm{a}, \mathrm{nm}$) by the following expression [16]:

$$\Delta\Gamma = \frac{\Delta\mathrm{a}(n_a - n_c)}{\partial n/\partial c} \quad (7)$$

where n_a and n_c are refractive indices of the adlayer material and the sensing fluid respectively, and $\partial n/\partial c$ is a partial change of refractive index relative to a change in concentration of the adlayer matter in fluid. For proteins $n_a \sim 1.5$ and $\partial n/\partial c$ is relatively constant and equal to 0.185 $\mathrm{mm^3/mg}$ [16]. By rearranging equations (6) and (7), the final expression relating surface mass density and power change due to adlayer formation on a straight waveguide is:

$$\Delta\Gamma = \frac{1}{k_2}\frac{(n_a - n_c)}{\partial n/\partial c}\left(\frac{\mathrm{P_{out}}(\mathrm{a_1})}{\mathrm{P_{out}}(\mathrm{a_0})} - 1\right) \quad (8)$$

The only unknown k_2 can be found either analytically for the known sensor parameters (*e.g.* waveguide design) or experimentally by performing a simple BSA adsorption test on a bare Au waveguide [17]. Extensive use of equation 8 was made for the detection of leukemia markers in patient sera (Chapter 4).

1.4. Analyte recognition systems

There are three common biorecognition systems: a) biocatalytic, which employs enzyme-substrate catalytic reactions, b) affinity binding systems, that use specific biomolecular interactions (protein-protein, DNA-protein, *etc.*), and c) synthetic biomimetic systems, where analyte is imprinted into the polymer and the mimetic structure serves as a recognition platform. Biocatalytic systems are mostly used in electrochemical sensors to create an electron transport chain. Affinity binding systems are most common and can be employed in a variety of biosensors. Antibody-antigen interaction is commonly used for a specific analyte recognition and capture. Novel types of recognition elements such as aptamers and peptides are also under extensive research and development. Aptamers are oligonucleotides of 40-100 bps length that can posses affinities and selectivities comparable to that of antibodies. Aptamers are also considered to be a possible replacement for antibodies in the future. Biomimetic systems are relatively new and

presently show a number of disadvantages such as lack of specificity [1]. All the biosensing work in this thesis has been done using affinity binding, particularly exploiting antibody-antigen interactions (immunological sensing).

Proteins are biological polymers that consist of ~20 various types of amino-acids (AA). Biologically synthesized, depending on the types and sequence of AA, proteins express very different properties. A post-synthetic 3D folding of the long-chain AA polymer is of high importance since only in a non-denatured 3D configuration will the protein be functional. Antibody, also known as immunoglobulin, is a protein that recognizes and binds to a specific analyte (antigen). Antibodies are synthesized by B-Cells, a type of white blood cell (lymphocyte) involved in immune response, and secreted into the blood stream. Immunoglobulin G (IgG) is the predominant antibody in humans and is comprised of approximately 1200 amino acids, Y-shaped, 8×10×14 nm^3 in size, and weighs ~150 kDa (Fig. 10) [18].

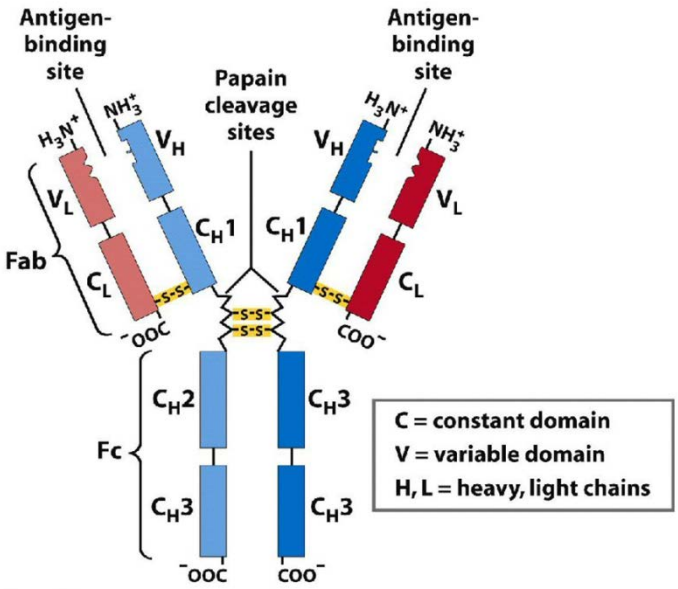

Figure 10. Schematic diagram of immunoglobulin G (IgG) molecule. Reproduced with permission from [19].

There are three main structural components to IgGs, pertinent to this thesis:

1. *Fragment Antigen Binding* sites (Fabs) that selectively recognize and non-covalently bind to the antigen. The binding is reversible by modifying the ionic strength of the

environment. There are only two Fabs per IgG molecule and they are the most variable regions.

2. *Fragment Crystallizable* region (Fc) is a relatively constant in composition and conformation throughout the whole variety of IgGs in single species; involved in immune response and is recognized by immune cells of the same organism.

3. *Light Chains* are covalently attached to the heavy chains of IgG. Two types of light chains exist in mammals: kappa (IgGκ) and lambda (IgGλ). Each IgG molecule possesses only one type. In healthy individuals the kappa to lambda ratio ranges from 1.4 to 2.0.

1.5. Surface Functionalization strategies

One of the key elements for designing a proper biosensing experiment is choosing the right functionalization strategy, and this concern is common for most biosensors. Depending on the substrate, proteins can be attached to the surface via a number of different methods. Generally these methods can be subdivided into three categories: functionalization by adsorption, by covalent, or non-covalent attachment. All three methods have advantages and disadvantages. Protein adsorption on gold often results in protein denaturation, but on the other hand, it does not require any prior surface treatment. Covalent attachment is considered to be favourable due to the absence of protein denaturation, but steric hindrance and epitope blocking due to its attachment to the surface are significant issues. Non-covalent attachment is also favourable (*e.g.* Protein G-IgG affinity), but in case when surface regeneration is desired, additional re-functionalization steps are required.

Plasmonic sensors including LRSPPs primarily utilize gold as a substrate. For functionalization purposes Au is considered to be favourable for a number of reasons: a) it is historically well studied, b) a formation of alkane self-assembled monolayer (SAM) can be easily achieved for further attachment of protein receptor (*e.g.* antibody), and c) SAMs can be formed quickly and remain stable for a long period of time [20]. Two functionalization strategies have been explored in this thesis: through SAM formation and Protein G-IgG affinity.

1.5.1. Self-assembled monolayer (SAM) approach

Formation of the SAM occurs through a covalent bonding of thiol groups of alkanethiols and gold: $2Au + 2HS\text{-}R \rightarrow 2Au\text{-}S\text{-}R + H_2$. Provided that a good quality gold film is available (preferably Au (111)), a tight and uniform packing of the SAM on the surface can be achieved (Fig.11).

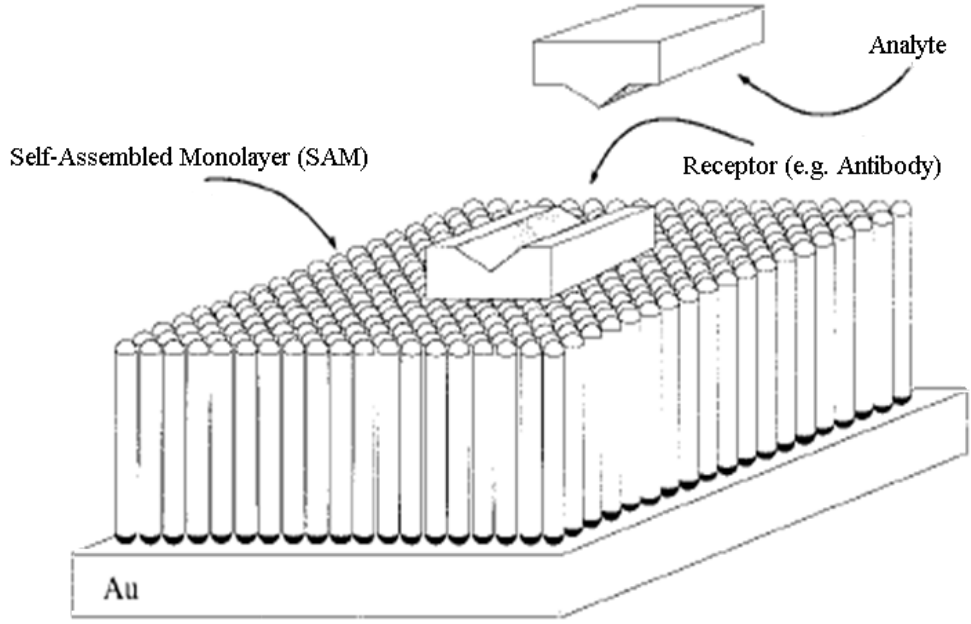

Figure 11. Schematic representation of a system for the study of molecular recognition events between analyte in solution and a receptor on a functionalized alkanethiolate monolayer on gold. Reproduced with permission from [21].

Depending on the terminal group of the SAM (R), the modified surface can express different unique properties. For example, SAM consisting of repeated polyethelene glycol (PEG) groups within a chain provides a blocking surface that mitigates protein physisorption. Alternatively, charged surfaces such as amine- or carboxyl-terminated surfaces promote water-soluble protein adsorption since these proteins are also charged [22]. After the formation of a SAM on the surface, protein of interest is attached to the terminal group through a process called *bioconjugation*. There are a number of different strategies that have been developed to functionalize gold surface via different combinations of SAMs and chemistries, for example “click chemistry” and Diels–Alder reaction [23]. However, the most frequently implemented procedure in biosensing consists

of a covalent attachment of proteins to carboxyl-terminated SAM. One of the protein constituents is amino-acid Lysine and has a primary amine as a terminal group. Carboxylic acid can undergo a zero-length coupling to a primary amine via a *carbodiimide chemistry* (Fig.12). The reaction is catalyzed by *N*-(3-Dimethylaminopropyl)-*N'*-ethylcarbodiimide hydrochloride (EDC) and N-ydroxysuccinimide sodium salt (NHS) in an aqueous solvent and, if required, by unsalted forms of EDC and NHS in an organic solvent. EDC/NHS coupling is extensively implemented in this thesis for IgG attachment to carboxyl-terminated SAM (Chapters 2 and 3).

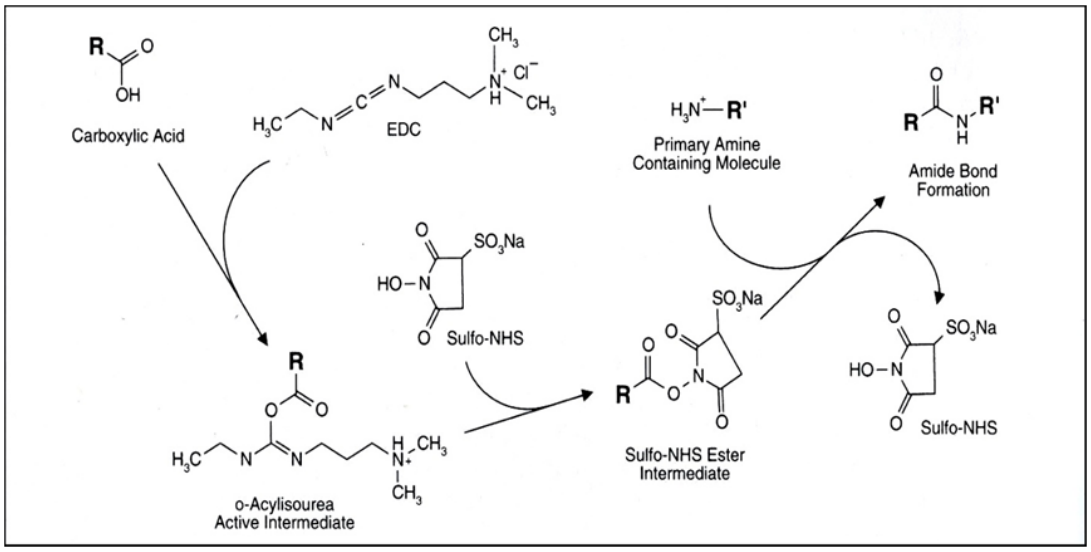

Figure 12. EDC- and NHS-mediated two-step process of amine-carboxylic acid coupling. Reproduced with permission of Academic Press [24].

1.5.2. Protein G approach

Protein G (~65 kDa) is a cell wall protein found in most species of bacterium *Streptococci* and is known to have a high affinity for the Fc region of IgG [25]. It is commonly used for purification and detection of immunoglobulins, for example as Protein G beads in protein separation columns. For planar biosensors it has an additional appeal since adsorbed immunoglobulins orient themselves in an upward orientation allowing Fabs to be fully exposed to capture analytes in solution. This is a significant advantage over covalent IgG conjugation (*e.g*. EDC/NHS chemistry), since in the latter, IgG molecules are reacted to SAM in random orientation thus potentially decreasing surface avidity (Fig. 13). Mostly two approaches for Protein G immobilization on planar Au sensors have been

investigated using SPR [26] and QCM [27]: covalent attachment [28], and simple adsorption [27]. Successful attempts to properly orient Protein G on Au were performed by genetic modification with addition of cysteine residues [29]. Adsorption of Protein G on Au was optimized for orientation by investigating the effect of temperature and pH, where pH=7.2 exhibited the best orientation [27].

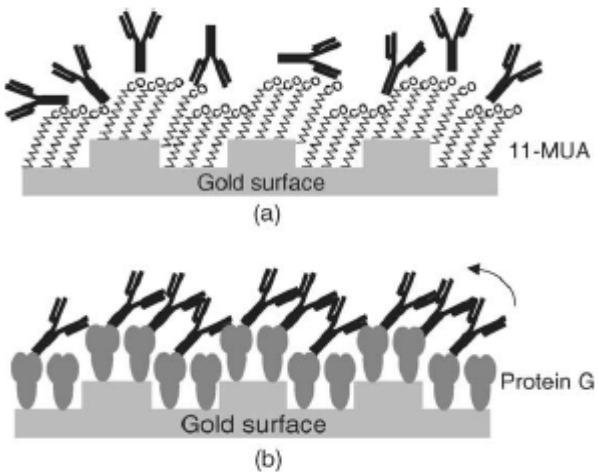

Figure 13. Schemes of the configuration of IgG immobilized on the two types of base layer: (a) the IgG layer immobilized covalently on 11-mercaptoundecanoic acid (11-MUA) layer with disordered-orientation, (b) the IgG layer on the Protein G layer with a constant-ordered orientation. Reproduced with permission from [26], *licence number* 3774931102112.

Protein G functionalization in this thesis was applied for leukemia marker (IgG lambda and IgG kappa) detection in patient serum (Chapter 4). This approach was intentionally chosen also because it provided an additional advantage of selectivity by capturing only human IgGs from a pool of serum proteins, thus performing an "immunological filtering" function. Au surface functionalization was performed by Protein G adsorption.

1.6. Literature Review

Biosensing using LRSPP waveguides is a new field of study, and particularly our group advanced far into fabrication, characterization and actual experimental testing of LRSPP waveguides. However, SPR is a well known sensing platform which closely resembles LRSPP sensing and protocols, and therefore is discussed in this section. Non-metallic waveguides have also been utilized for biosensing and are discussed. One of the key elements in biosensing is surface functionalization with recognition chemistries, which has been studied using SPR, and is discussed in details in this section. Finally, some theoretical and minor experimental work that has been done with LRSPP waveguides is also presented.

The first observation of plasmon wave phenomena on a metal surface originates in the early 20th century, when Robert W. Woods discovered anomalies in diffraction on metal gratings [30]. However, there was no appropriate explanation of the phenomenon until 1960s when Kretschmann [31] and Otto [32] were able to excite plasmon waves by means of attenuated total reflection. Actual research in the application of SPR for sensing started in the beginning of the 1980s at Uppsala University, Sweden. They were the first to demonstrate gas detection in 1983, where a plasmon wave was excited using a prism with a deposited thin layer of silver [33]. Different concentrations of halothane gas were detected through its adsorption to silicon oil on a Ag layer. The same group also demonstrated the first protein-protein interaction with SPR using the same Ag-deposited prism method. In 1983 they adsorbed human IgG onto a Ag layer following immunological detection of anti-human IgG [34]. Since then, the SPR prism-based sensor was patented and manufactured by Biacore (Uppsala, Sweden), who later became a part of GE Healthcare, and nowadays numerous SPR sensors are commercially available. Applications of SPR sensors are wide and range from pathogen to DNA and toxin detection. A great deal of studies with SPR sensors have been published in the past several decades, thus, only some prominent recent work of various applications of the sensor are reviewed.

A number of common food pathogens have been detected by SPR systems through capture of whole bacteria on the sensor surface. *E. coli* O157:H7 was detected in milk, apple juice, and ground beef with a limit of detection (LOD) of 10^2-10^3 cfu/ml [35]. Biotinylated *E.coli* O157:H7 antibodies were attached to the sensor through neutravidin adsorbed to Au surface [35]. A very low LOD of 23 cfu/ml was achieved for *Salmonella enterica* detection in pasteurized milk by Waswa *et al.* [36]. Polyclonal anti-*S.enterica* antibodies were functionalized on the SPR sensor surface by attaching the latter to Protein A covalently linked to a dextran matrix and further detection of whole *Salmonella* cells [36]. *Listeria monocytogenes* was detected in buffer with a LOD of 20 cfu/ml using SPR by Lee *et al*. [37]. A specific aptamer (oligonucleotide) was synthesized and attached to the Au surface for whole *L. monocytogenes* bacteria capture [37].

Proteins are considerably smaller in dimensions compared to bacterial cells (~5-40 nm *versus* ~1000 nm) and thus the SPR's high sensitivity becomes more significant. In

addition, protein detection is very common in medical diagnostics. Such as, vascular endothelial growth factor (VEGF), which plays a role in breast cancer, lung cancer, and colorectal cancer, was detected with LOD of 100 pg/ml using SPR by Chen *et al*. [38]. Two different aptamers were functionalized on the sensor surface to recognize two different domains of VEGF [38]. In order to enhance the SPR signal for protein detection, various sensing assays common to ELISA method, such as sandwich, competitive and inhibition assays, are also often employed in SPR detection protocols. As an application for medical diagnostics, picomolar detection of interlukin-8 using sandwich assay was achieved by Yang *et al*. [39]. Interleukin-8 (IL-8) is a cytokine, elevated levels of which can be indicative of several types of cancer. Two monoclonal antibodies recognizing different epitopes on interleukin-8 were used to detect IL-8 in oropharyngeal squamous cell carcinoma patient saliva with LOD of 185 pM. Primary antibodies were attached to the SPR sensor through covalent conjugation with dextran matrix [39]. Detection of antibodies against viruses in patient plasma or serum can suggest an ongoing viral infection. Direct detection of Epstein–Barr virus antibodies in clinical patients using SPR was reported by Riedel *et al*. [40]. Streptavidin was attached to the sensor surface via polyoligo(ethyleneglycol) methacrylate, where the latter was used to reduce fouling from undiluted patient serum. Biotinylated oligonucleotides carrying an antigen were then immobilized to the streptavidin-functionalized surface. A successful regeneration of the surface down to the streptavidin level with repeated subsequent serum testing was also reported [40]. In the pharmaceutical sector SPR is widely used to assess the efficiency of therapeutic agents. Such that, He *et al.* developed five therapeutic antibodies (Abs) against West Nile virus and determined the optimum Ab based on their binding strengths to envelope protein E of the virus [41]. Several analytical techniques were used, including SPR.

Small organic molecule detection is a fair challenge and has a great importance in a variety of fields. Detection of melamine (126 Da molecule) in milk products became an issue when manufacturers started adding it to increase protein content. Recently Lu *et al.* demonstrated the detection of melamine in different milk products with LOD of ~25 ng/ml [42]. BSA-conjugated melamine was functionalized on an SPR sensor surface via carbodiimide chemistry to an alkanethiol self-assembled monolayer (SAM). An inhibition

assay was applied by introducing a solution with anti-melamine antibodies and melamine molecules [42]. 2,4,6-Trinitrotoluene (TNT) is a well-known toxin that exhibits mutagenic and carcinogenic effects, and is a prime constituent of landmines. Highly sensitive TNT detection was demonstrated by functionalizing a SPR sensor surface with a complex poly-(vinylamine-co-N-vinylformamide) (poly-(vinylamine-co-vinylformamide)) matrix which allowed for multiple attachment of TNT molecules, and LOD of 28 ppt was determined by inhibition assay [43].

The first experimental work demonstrating long-range surface plasmon (LRSP) sensing was reported in 1983. A Kretschmann prism-based sensor was modified by creating two dielectric layers: a solid fused silica substrate at the interface between the prism and a Ag thin film, and liquid refractive index-matching Cargille oil at the exposed surface [44]. Since then, few studies have been done in this direction and no commercially available instruments exist. Slavík and Homola [45] modified conventional SPR (cSPR) with a low-refractive index fluoropolymer Teflon by depositing the latter at the interface between the glass prism and a Au thin film. Compared to cSPR, a Teflon-modified SPR was demonstrated to have LOD to be twice lower for bulk refractive index measurements (2.5×10^{-8} RIU), and was claimed to be the lowest value reported for SPR-based instrumentation [45]. The same Teflon-modified cSPR was tested for *E. coli* (HB101P) detection. Polyclonal antibodies against *E. coli* were immobilized to the sensor surface via alkanethiol SAM and carbodiimide chemistry. Direct sensing assays for *E. coli* detection in buffer were applied to both cSPR and LRSP, where LRSP-based sensor demonstrated a 5.5-fold higher response than cSPR [46]. Another comparative study was performed using CYTOP- and Teflon-modified cSPR sensor. Fluorescently labeled streptavidin was immobilized on the sensor surface via carbodiimide chemistry on carboxyl-terminated SAM. Biotinylated anti-rabbit IgG was detected and compared to cSPR to have a 4.4-fold enhancement of the measured response [47].

Non-metallic optical waveguides have also been used for biosensing and are mostly comprised of silicon and its derivatives. Structurally, non-metallic optical sensors do not utilize straight waveguides, but rather different types of interferometers. Interferometric sensing theoretically is more sensitive since it involves detection of phase difference between sensing and reference arms [48]. Biotin-streptavidin interactions have been

studied by Weisser *et al*. using a Mach-Zehnder Interferometer (MZI) [49]. AnSiO_2 MZI waveguide was functionalized with biotin-terminated PEG following streptavidin injection. The authors claimed the detection of 1% of a streptavidin monolayer on the MZI sensing arm, which translates to a protein LOD of 20 pg/mm^2 for the device. A Young's Interferometer (YI) SiO_2-based sensor was used for the detection of herpes simplex virus type 1 (HSV-1). Waveguides were functionalized with antibodies against HSV-1 and serum doped with HSV-1 particles was injected. The sensor demonstrated a LOD of 105 virions/ml within 30 minutes [50]. A Hartman interferometer with Si_3N_4 waveguides was also used to detect human chorionic gonadotropin (hCG) in whole blood. Avidin-biotin coupling was used to functionalize the sensor surface with anti-hCG, colloidal Au nanoparticles were used to amplify the signal, and 5 kDa PEG was immobilized on the reference waveguide to block non-specific binding. The authors were able to demonstrate detection of 0.1 ng/ml of hCG in whole blood [51].

Application of LRSPP waveguides for biosensing, on the other hand, has mostly been theorized for various waveguide configurations and very little actual experimental work has been done. Descriptive theory and modeling of LRSPP SWGs for sensing applications can be found in [10, 52]. A brief description of some of the theoretical studies performed with other plasmonic waveguide structures follows. Theoretical investigation of metal-insulator-silicon MZI waveguides has been performed by Kwon *et al.* [53]. A waveguide metal-insulator-metal configuration with a resonator ring separating two waveguides was proposed by Diniz *et al.* [54]. So far, only one experimental study of sensing using LRSPP waveguides has been found in literature, where a double-electrode LRSPP biosensor with a Bragg grating on the bottom of the sensing channel was demonstrated to detect changes in refractive index in solution with a LOD of 10^{-6} RIU [55].

1.7. Thesis Scope and Outline

The aim of this thesis is to demonstrate the capability of the novel long-range surface plasmon-polariton waveguide biosensor for various sensing applications. The scope of this thesis consists of four main points:

- *Proof-of-concept for LRSPP SWG sensing*: In the context of biosensing using LRSPP waveguides, only one study reported actual experimental work [55]. However, this study involved the detection of refractive index changes in bulk only. This thesis presents the capability of LRSPP SWGs to detect changes of RI in bulk, detect large biological objects such as cells and small objects such as proteins.

- *Immunological capture and detection of large biological entities with LRSPP SWG sensor*: Previous studies with SPR biosensor reported numerous cases of whole cell detection using antibodies against a certain protein present on the cell membrane. This thesis presents the experimental demonstration of plasmonic SWGs to detect human red blood cells in clear buffer. In addition, by functionalizing the surface with antibodies against A-antigen, a differentiation between groups containing A-antigen (A and AB) and lacking the latter (O and B) is also demonstrated.

- *Immunological capture and detection of small biological entities with LRSPP SWG sensors*: Detection of proteins, as well as protein-protein interaction is highly important for clinical and pharmaceutical sectors. This thesis presents the demonstration of immunoglobulin G detection in patient serum as a potential application for B-cell leukemia diagnostics. Furthermore, relative abundance of IgG kappa and lambda light chains was detected.

- *Optimization for sensitivity of LRSPP SWG sensor*: Investigation on improving sensor performance is also a necessary study in order to carry out detections that require higher sensitivity. This thesis presents a theoretical and experimental study on improving LRSPP SWG sensor sensitivity.

This thesis consists of a collection of scientific articles, each of them presented as a chapter. The remainder of this thesis is organized as follows. Chapter 2 reports the first successful demonstration of LRSPP SWG sensing through: a) detection of refractive index changes in solution, b) specific detection of human red blood cells (RBCs of blood group A), and c) non-specific detection of bovine serum albumin by adsorption. Chapter 3 focuses on cell detection demonstrating the LOD for RBC sensing and a signal-to-noise ratio for single cell detection. Chapter 4 reports specific sensing of relative abundance of immunoglobulin kappa and lambda light chains as an application for B-cell leukemia detection. Chapter 5 describes theoretical and experimental approaches for maximizing the LRSPP waveguide sensitivity for biosensing applications. Finally, Chapter 6 presents the conclusions and suggestions for future work.

Chapter 2

Biosensing using straight LRSPP waveguides (Proof of Concept)

2.1. Summary

This chapter provides first extensive (bio)sensing experiments using LRSPP SWGs. The sensitivity of the sensor to refractive index change in bulk was experimentally determined by injecting six solutions of different refractive indices in 2×10^{-3} RIU increments. The LOD was found to be 2.3×10^{-6} RIU and was comparable to that of conventional SPR. The specific cell detection was demonstrated by injecting O-RBCs and A-RBCs onto the sensors surface functionalized with anti-A antibodies. After O-RBC injection and cell settling on the waveguide, the signal was easily regenerated back to the initial baseline level. However regeneration with buffer of A-RBCs was unsuccessful suggesting a strong specific attachment of A-RBCs to the anti-A functionalized waveguide. Protein sensing was demonstrated by injection of BSA onto carboxyl-terminated SAM (to promote adsorption) and PEG-terminated SAM (protein blocking surface). Signal-to-noise ratios were ~300 for carboxyl- and ~45 for PEG-functionalized surfaces respectively. This suggested the ability of the sensor to detect proteins, as well as confirmed surface functionalization protocols for SAM formation.

2.2. Contribution

The results provided in this chapter were published as an article in the journal *Optics Express*. The setup was designed and built with the help of Ewa Lisicka-Skrzek and Asad Khan. The sensors were fabricated by Hamoudi Asiri. I designed and performed all the

experiments, partially analyzed the data and wrote the manuscript. Dr. Berini performed the theoretical analysis of waveguide responses, contributed to the design of experiments and revised the manuscript. Dr. Chen Wang and Dr. R. Niall Tait also revised the manuscript.

2.3. Article

The published article is adapted by permission from [14] and follows verbatim.

Biosensing using straight long-range surface plasmon waveguides

Oleksiy Krupin,[1] Hamoudi Asiri,[1] Chen Wang,[2] R. Niall Tait,[3] and Pierre Berini,[4,5,]

[1]*Department of Chemical and Biological Engineering, University of Ottawa, Ottawa, Ontario, Canada*
[2]*Department of Pathology and Laboratory Medicine, Mount Sinai Hospital, University of Toronto, Toronto, Canada*
[3]*Department of Electronics, Carleton University, Ottawa, Ontario, Canada*
[4]*School of Electrical Engineering and Computer Science, University of Ottawa, Ottawa, Ontario, Canada*
[5]*Department of Physics, University of Ottawa, Ottawa, Ontario, Canada*

Abstract: Straight long-range surface plasmon waveguides are demonstrated as biosensors for the detection of cells, proteins and changes in the bulk refractive index of solutions. The sensors consist of 5 μm wide 22 nm thick Au stripes embedded in polymer (CYTOP^{TM}) with microfluidic channels etched into the top cladding. Bulk sensing is demonstrated by sequentially injecting six solutions of different refractive indices in 2×10^{-3} RIU increments; such index steps were detected with a signal-to-noise ratio of ~1000. Selective capture of cells is demonstrated using Au waveguides functionalized with antibodies against blood group A, and red blood cells of group A and O in buffer as positive and negative analyte. Bovine serum albumin in buffer was used to demonstrate protein sensing. A monolayer of bovine serum albumin physisorbed on a carboxyl-terminated self-assembled monolayer on Au was detected with a signal-to-noise ratio of ~300. Overall, the biosensor demonstrated a good capability for detecting bulk changes in solution and for sensing analyte over a very wide range of mass (from cells to proteins). The biosensors are compact, inexpensive to fabricate, and may find use over a wide range of cost-sensitive sensing and detection applications.

OCIS codes: (280.1415) Biological sensing and sensors; (240.6680) Surface plasmons; (130.3120) Integrated optics devices; (230.7390) Waveguides, planar; (250.5403) Plasmonics.

14 January 2013 / Vol. 21, No. 1 / OPTICS EXPRESS 698

References and links

1. J. Homola, "Surface plasmon resonance sensors for detection of chemical and biological species," Chem. Rev. **108**(2), 462–493 (2008).
2. S. Löfås, "Optimizing the hit-to-lead process using SPR analysis," Assay Drug Dev. Technol. **2**(4), 407–415 (2004).

3. P. Berini, "Long-range surface plasmon polaritons," Adv. Opt. Photonics **1**(3), 484–588 (2009).
4. R. Charbonneau, C. Scales, I. Breukelaar, S. Fafard, N. Lahoud, G. Mattiussi, and P. Berini, "Passive integrated optics elements based on long-range surface plasmon polaritons," J. Lightwave Technol. **24**(1), 477–494 (2006).
5. A. Boltasseva, T. Nikolajsen, K. Leosson, K. Kjaer, M. S. Larsen, and S. I. Bozhevolnyi, "Integrated optical components utilizing long-range surface plasmon polaritons," J. Lightwave Technol. **23**(1), 413–422 (2005).
6. P. Berini, "Bulk and surface sensitivities of surface plasmon waveguides," New J. Phys. **10**(10), 105010 (2008).
7. S. Löfås and B. Johnsson, "A novel hydrogel matrix on gold surfaces in surface plasmon resonance sensors for fast and efficient covalent immobilization of ligands," J. Chem. Soc. Chem. Commun. 1526–1528 (1990).
8. I. Breukelaar, R. Charbonneau, and P. Berini, "Long-range surface plasmon-polariton mode cutoff and radiation in embedded strip waveguides," J. Appl. Phys. **100**(4), 043104 (2006).
9. R. Slavík and J. Homola, "Ultrahigh resolution long range surface plasmon-based sensor," Sens. Act. B Chem. **123**(1), 10–12 (2007).
10. A. W. Wark, H. J. Lee, and R. M. Corn, "Long-range surface plasmon resonance imaging for bioaffinity sensors," Anal. Chem. **77**(13), 3904–3907 (2005).
11. Y. H. Joo, S. Song, and R. Magnusson, "Demonstration of long-range surface plasmon-polariton waveguide sensors with asymmetric double-electrode structures," Appl. Phys. Lett. **97**(20), 201105 (2010).
12. J. Dostálek, A. Kasry, and W. Knoll, "Long range surface plasmons for observation of biomolecular binding events at metallic surfaces," Plasmonics **2**(3), 97–106 (2007).
13. J. Guo, P. D. Keathley, and J. T. Hastings, "Dual-mode surface-plasmon-resonance sensors using angular interrogation," Opt. Lett. **33**(5), 512–514 (2008).
14. M. Vala, S. Etheridge, J. A. Roach, and J. Homola, "Long-range surface plasmons for sensitive detection of bacterial analytes," Sens. Actuators B Chem. **139**(1), 59–63 (2009).
15. B. Agnarsson, J. Halldorsson, N. Arnfinnsdottir, S. Ingthorsson, T. Gudjonsson, and K. Leosson, "Fabrication of planar polymer waveguides for evanescent-wave sensing in aqueous environments," Microelectron. Eng. **87**(1), 56–61 (2010).
16. N. Kinrot, "Analysis of bulk material sensing using a periodically segmented waveguide Mach–Zehnder Interferometer for biosensing," J. Lightwave Technol. **22**(10), 2296–2301 (2004).
17. B. Y. Shew, Y. C. Cheng, and Y. H. Tsai, "Monolithic SU-8 micro-interferometer for biochemical detections," Sens. Actuators A Phys. **141**(2), 299–306 (2008).
18. R. G. Heideman and P. V. Lambeck, "Remote opto-chemical sensing with extreme sensitivity: design, fabrication and performance of a pigtailed integrated optical phase-modulated Mach–Zehnder interferometer system," Sens. Actuators B Chem. **61**(1-3), 100–127 (1999).
19. D. X. Xu, A. Densmore, A. Delâge, P. Waldron, R. McKinnon, S. Janz, J. Lapointe, G. Lopinski, T. Mischki, E. Post, P. Cheben, and J. H. Schmid, "Folded cavity SOI microring sensors for high sensitivity and real time measurement of biomolecular binding," Opt. Express **16**(19), 15137–15148 (2008).
20. J. C. Love, L. A. Estroff, J. K. Kriebel, R. G. Nuzzo, and G. M. Whitesides, "Self-assembled monolayers of thiolates on metals as a form of nanotechnology," Chem. Rev. **105**(4), 1103–1170 (2005).
21. M. Tencer, H.-Y. Nie, and P. Berini, "Electrochemical differentiation and TOF-SIMS characterization of thiolcoated gold features for (bio)chemical sensor applications," J. Electrochem. Soc. **156**(12), J386–J392 (2009).
22. M. Tencer, A. Olivieri, B. Tezel, H.-Y. Nie, and P. Berini, "Chip-scale electrochemical differentiation of SAM-coated gold features using a probe array," J. Electrochem. Soc. **159**(3), J77–J82 (2012).
23. G. Gagnon, N. Lahoud, G. A. Mattiussi, and P. Berini, "Thermally activated variable attenuation of long-range surface plasmon-polariton waves," J. Lightwave Technol. **24**(11), 4391–4402 (2006).
24. T. Nikolajsen, K. Leosson, and S. I. Bozhevolnyi, "Surface plasmon polariton based modulators and switches operating at telecom wavelengths," Appl. Phys. Lett. **85**(24), 5833–5835 (2004).
25. D. F. Hayes, M. Cristofanilli, G. T. Budd, M. J. Ellis, A. Stopeck, M. C. Miller, J. Matera, W. J. Allard, G. V. Doyle, and L. W. W. M. Terstappen, "Circulating tumor cells at each follow-up time point during therapy of metastatic breast cancer patients predict progression-free and overall survival," Clin. Cancer Res. **12**(14), 4218–4224 (2006).

26. H. Asiri, “Fabrication of surface plasmon biosensors in cytop,” Master’s Thesis, Department of Chemical and Biological Engineering, University of Ottawa, Ottawa (2012).
27. C. Chiu, E. Lisicka-Skrzek, R. N. Tait, and P. Berini, “Fabrication of surface plasmon waveguides and devices in cytop with integrated microfluidic channels,” J. Vac. Sci. Technol. B **28**(4), 729–735 (2010).
28. L. M. Fischer, M. Tenje, A. R. Heiskanen, N. Masuda, J. Castillo, A. Bentien, J. Émneus, M. H. Jakobsen, and A. Boisen, “Gold cleaning methods for electrochemical detection applications,” Microelectron. Eng. **86**(4-6), 1282–1285 (2009).
29. T. Greg, Hermanson, *Bioconjugate Techniques*, 2nd ed.(Academic, 2008), Chap. II(3).
30. J. G. Quinn, R. O’Kennedy, M. Smyth, J. Moulds, and T. Frame, “Detection of blood group antigens utilising immobilised antibodies and surface plasmon resonance,” J. Immunol. Methods **206**(1-2), 87–96 (1997).
31. V. Silin, H. Weetall, and D. J. Vanderah, “SPR studies of the nonspecific adsorption kinetics of human IgG and BSA on gold surfaces modified by self-assembled monolayers (SAMs),” J. Colloid Interface Sci. **185**(1), 94–103 (1997).
32. J. A. De Feijter, J. Benjamins, and F. A. Veer, “Ellipsometry as a tool to study the adsorption behavior of synthetic and biopolymers at the air-water interface,” Biopolymers **17**(7), 1759–1772 (1978).
33. M. J. Felipe, P. Dutta, R. Pernites, R. Ponnapati, and R. C. Advincula, “Electropolymerized bioresistant coatings of OEGylated dendroncarbazoles: design parameters and protein resistance SPR studies,” Polymer (Guildf.) **53**(2), 427–437 (2012).
34. P. Berini, “Plasmon-polariton modes guided by a metal film of finite width bounded by different dielectrics,” Opt. Express **7**(10), 329–335 (2000).
35. R. Charbonneau, M. Tencer, N. Lahoud, and P. Berini, “Demonstration of surface sensing using long-range surface plasmon waveguides on silica,” Sens. Actuators B Chem. **134**(2), 455–461 (2008).
36. M. Tencer, R. Charbonneau, N. Lahoud, and P. Berini, “AFM study of BSA adlayers on Au stripes,” Appl. Surf. Sci. **253**(23), 9209–9214 (2007).

1. Introduction

The field of optical biosensors is currently dominated by the methods of Surface Plasmon Resonance (SPR). Conventional SPR systems utilize a Kretschmann-Raether configuration, where a prism with a thin layer of Au is interrogated with a transverse magnetic (TM) polarized beam [1]. Real-time and label-free detection, and the small amount of required [2]. Real-time monitoring of reactions allows the extraction of biochemical interaction kinetics, while label-free sensing avoids unnecessary chemical manipulation of analyte or/and receptor molecules.

This paper presents a novel optical biosensor based on long-range surface plasmon-polariton (LRSPP) waveguides. LRSPPs are propagating plasmon waves that can be excited by TM-polarized light on thin symmetric metal stripes or slabs, and that can propagate over appreciable lengths [3]. The LRSPP is a symmetric coupled mode formed by the coupling of single-interface SPPs through the thin metal film. The metal stripe provides optical confinement in the plane transverse to the direction of propagation, leading to the realization of a number of different integrated components such as S-bends, Y-junctions, couplers and Mach-Zehnder Interferometers (MZIs) [4,5]. LRSPP excitation can be easily achieved by butt-coupling an optical single-mode fiber to the metal stripe, which can lead to compact structures and miniaturization of biosensors.

Although, LRSPPs are less confined and less surface sensitive than single-interface SPPs, they propagate much farther so long-interaction length sensors providing greater adlayer sensitivity and a lower detection limits are possible [6]. Also, the sensing depth is greater (~1μm *vs.* ~200 nm) so greater loading is possible, say via the use of a dextran hydrogel matrix to capture more proteins along this dimension [7]. Finally, LRSPPs are also useful for sensing large biological entities such as cells which cause strong scattering of loosely bound LRSPPs into radiative modes.

In a butt-coupling arrangement, the lowest insertion loss for an LRSPP waveguide occurs when the refractive index around the metal stripe is homogeneous [8] (the insertion loss depends on the coupling efficiency and the attenuation of the mode). In order to match the refractive index of

biologically compatible fluids, which have n≈1.33, low index claddings are needed. An advantage of using low index claddings is that fluidic channels become optically less invasive once filled with sensing solution. Cytop (Asahi) and Teflon (Dupont) are suitable and both have been used in sensing experiments involving LRSPPs on metal slabs in prism-coupled geometries [9–14]. Cytop has also been used as a dielectric waveguide sensor [15], as have other dielectric materials such as silicon nitride [16–18] and silicon on insulator [19].

The sensors presented in this work consist of straight Au waveguides embedded in Cytop with an etched microfluidic channel providing access to the Au surfaces. These structures differ from previous ones involving LRSPPs in that the latter are based on metal slabs which provide no lateral confinement. They also differ from dielectric waveguides in that the mode of operation is a surface plasmon and a metal stripe is used as the "core". One rationale behind using Au waveguides instead of dielectric waveguides is the easy integration of surface chemistries for well-controlled functionalization. Generally Au is considered a preferable material for functionalization for a number of reasons: *i*) it is historically most studied, *ii*) organized packing of an alkanethiol self-assembled monolayer (SAM) can be easily achieved (organization and packing improves as the Au surface tends toward single crystal 111), *iii*) SAMs formed on Au from thiols are stable for long periods of time, *iv*) SAMs form quickly through a simple incubation process: 80-90% of the SAM forms in a matter of minutes, and *v*) Au is a relatively inert material that does not oxidize below its melting temperature and does not react with most chemicals [20]. SAM formation on SiO2, for example, requires alkylsilanes, which are harder to use and process due to their moisture sensitivity. Other rationale for the use of Au waveguides is the provision of additional functionality, such as electrochemical desorption for topo-selective functionalization [21,22], and thermo-optic modulation [23,24] such that signal processing techniques could be used to improve the signal-to-noise ratio.

The purpose of this paper is to demonstrate the capabilities of straight LRSPP waveguides for sensing large biological objects such as cells as well as small biochemical entities such as proteins. We also investigate the effects of bulk refractive index changes on the performance of the waveguides. Selective capture of cells is important in a number of applications in medicine, for example, for rare circulating tumor cell (CTC) detection in blood [25]. Protein sensing is the most common strategy used for pathogen detection and drug discovery. Bulk sensing can be implemented for the precise determination of the refractive index of solutions, and its effects must be known in order to avoid them during biochemical sensing.

2. Materials and methods

2.1 Sensing platform

The sensors were fabricated as described in [26,27]. Cytop was spin-coated and cured on a 4" Si wafer to form the bottom cladding. Au features were defined lithographically by Au evaporation and lift-off. The Cytop upper cladding was then spin-coated and microfluidic channels were defined lithographically and etched down to the Au stripe surface. The wafer was then covered with resist for protection and diced into ~300 dies, each die containing 16 straight waveguides.

A sensing die (6.5 mm wide by 3.8 mm long) is sketched in Fig. 1 and consists of LRSPP waveguides each formed from 5 μm wide ~22 nm thick Au stripes embedded in Cytop with a large fluidic channel etched into the top cladding. The sensing length (etched part) of a waveguide is L = 1.65 mm. Other waveguide structures which are not shown were also present on the die interspersed between the straight waveguides.

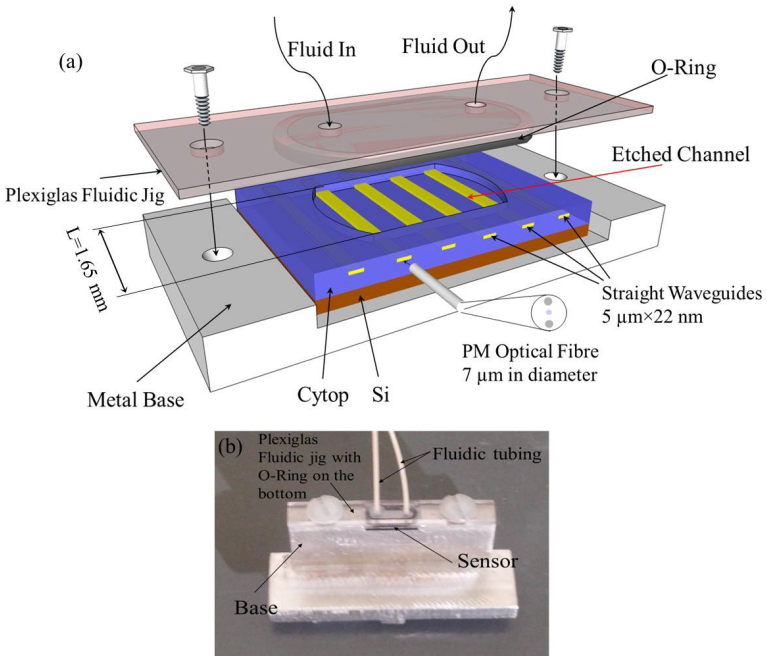

Fig. 1. Sensing device with integrated fluidics: a) schematic of the device placed on the metal base with a Plexiglas jig on top; the volume of the fluidic cell is 20 μL; b) image of the device with fluidics fixed on the metal base.

A custom made fluidic jig consisting of a Plexiglas slide, with two holes for fluidic tubing, and an O-Ring (Apple Rubber Products Inc.) matched in dimensions to the etched channel and attached on the bottom surface of the slide, provides a good seal and fluid exchange within the fluidic channel. A machined metal base (Al) is used to support the die and to integrate the sensor/fluidic assembly into the interrogation setup (Sec 2.2). The fluidic jig and the metal base are fixed together with screws leaving space at the front of the assembly to insert the optical fiber used to excite a waveguide sensor.

2.2 Interrogation setup

As a light source, a laser diode (NLK1356STG, λ_0 = 1310 nm, NTT Electronics) was used to provide an optical signal, carried by a polarization-maintaining (PM) optical fiber with a core diameter of 7 μm (PMJ-3AX-1300-7/125-1-1-1, OZ Optics). The diode output was controlled by a laser diode controller (LDC 3724B, ILX Lightwave). Two multi-axis positioning stages (Thorlabs Inc.) were used to align the fiber to the waveguide: a 6-axis stage to manipulate the fiber holder with the fiber and a 3-axis stage to manipulate the device under test (DUT) (*i.e.*, the sensor/fluidics assembly). A 25× objective lens (Melles Griot) was permanently fixed to the table, defining the optical axis of the output portion of the setup and used to magnify and collimate the optical signal emerging from the DUT. The background light was removed by an aperture and the beam split into two portions, one sent to an infrared camera to visually monitor the alignment procedure and observe changes in output during an experiment, and the other to a power meter (81618A, Hewlett Packard). Labview was used to control the setup and perform data acquisition. The fluid was supplied by a syringe pump (PicoPlus, Harvard Apparatus) through pico tubing (550 μm outer diameter, 250 μm inner diameter, IDEX), connected to the fluidic holes of the plexiglas jig. The setup is sketched in Fig. 2.

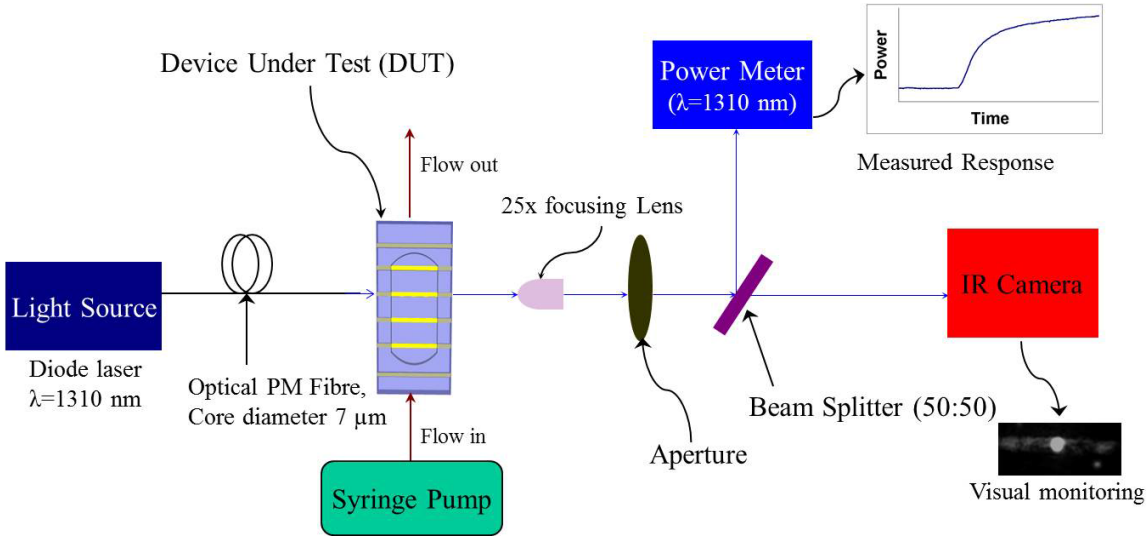

Fig. 2. Schematic representation of the interrogation setup with the sensing device.

2.3 Materials

2-Isopropanol semiconductor grade (IPA), 16-Mercaptohexadecanioc acid (HS(CH2)15COOH), triethylene glycol mono-11 mercaptoundecyl ether (HS(CH2)11(OC2H4)3OH), *N*-(3-Dimethylaminopropyl)-*N*′-ethylcarbodiimide hydrochloride (EDC), N-Hydroxysuccinimide sodium salt (NHS), acetone HPLC grade≥99.9%, Bovine Serum Albumin (BSA) and glycerol (electrophoresis grade), Phosphate buffer saline 0.01 M, pH 7.4 (PBS) were obtained from Sigma-Aldrich. PBS solution was prepared from the package by dissolving containing salts in 1 L of deionized water producing a buffer of the following constitution: 0.01 M phosphate buffer saline, 0.138 M NaCl and 0.0027 M KCl (according to the manufacturer). Packed human red blood cells (groups A and O) and antibodies against blood group A (Anti-A, Murine Monoclonal, Series 1, Immucor) were donated by Mount Sinai Hospital (Toronto). Distilled water was deionized using Millipore filtering membranes (Millipore, Milli-Q water system at 16 MΩ·cm).

2.4 Device cleaning and functionalization

The dicing photoresist was removed from an individual die by two sequential acetone baths (5 and 30 min), then by thoroughly washing in IPA. The cleanliness of the facets is of great importance to optical input and output coupling. Particulate matter, deposited during dicing, was removed by acetone and IPA ultrasonic baths (FS20H, Fisher Scientific) each of 1 min in duration. The sample was dried under N_2. Further removal of possible organic matter on Au stripes was performed in a 1:1 solution of 50 mM KOH:H_2O_2 (30%) [28] for 2 min followed by an intense wash in distilled/deionized water (DDI H_2O), then in IPA, followed by drying with N_2. Two types of alkanethiols were used in experiments to form SAMs: 16-mercaptohexadecanoic acid (16-MHA) for antibody functionalization or protein physisorption, and triethylene glycol mono-11 mercaptoundecyl ether (T-PEG) for avoiding non-specific adsorption. In both cases, the device was placed in a 2 mM IPA alkanethiol solution allowing the SAM formation to proceed for 12-18 hours.

For analysis of the BSA adsorption on different surfaces, a device after incubation in an alkanethiol solution was washed with plenty of IPA, dried under N_2 and assembled into the setup. Sensing of the refractive index of the bulk was performed with Au stripes functionalized with 16-

MHA. For selective capture of RBCs, prior to the device integration into the setup, Anti-A antibodies were attached to the 16-MHA SAM using NHS/EDC amine coupling chemistry [29]. The carboxyl group of 16-MHA was activated by placing the device in a DDI H_2O solution of 0.1M EDC/NHS (1:1) for 15 minutes. After rinsing with DDI H_2O the chip was placed into the solution of Anti-A (in PBS) for ~2 hrs. Upon completion of the conjugation reaction, the device was washed with plenty of PBS (pH 7.4, 0.01M phosphate) and assembled into the setup.

2.5 Analyte preparation

To investigate the effects of the refractive index of bulk solutions, six DDI H_2O/Glycerol (DDI/Gly) mixtures were prepared with index increments of $\pm 2\times10^{-3}$ RIU, about n=1.3348, which is the refractive index of Cytop; the index of the solutions were 1.3282, 1.3303, 1.3325, 1.3346, 1.3367 and 1.3409 as measured at λ_0 = 1312 nm using a prism-coupler based instrument (Model 2010, Metricon, Prism 200-P1). For all biosensing experiments, a mixture of biological buffer (PBS, pH = 7.4, 0.01 M phosphate) doped with 7.235% w/w glycerol (PBS/Gly) having an index of n = 1.3303 was used; the reason for using a sensing solution with an index slightly lower than that of Cytop will become apparent in Section 3.1.

Packed RBCs (group A and O), stored at 4 °C, were diluted with filtered PBS/Gly buffer and washed in a micro-centrifuge (Micromax, Thermo Electric Corp.) 3 times for 2 minutes (400 g) discarding the supernatant each time. Cells were counted using Hemacytometer (1483, Hausser Scientific).

BSA solutions were prepared by mixing lyophilized BSA with PBS/Gly buffer to a concentration of 100 μg/ml.

2.6 Sensing assay using the platform

Prior to device installation into the setup, the TM-polarization alignment of the fiber was ensured and the stability of the setup was verified over a period of 10 minutes with the beam emerging from the fiber and propagating directly through the output portion of the setup (***i.e.***, no DUT). The device was then assembled with fluidics, PBS/Gly buffer (n = 1.3303) was introduced into the channel and tubing, and the device/fluidic assembly was inserted into the setup. The fiber was butt-coupled to a waveguide of good quality based on the symmetry of the emerging mode (as observed with the IR camera) and the measured power output. In order to avoid Fabry-Perot interferences between the fiber and the input facet, a glass index-matching oil was used between the two surfaces (Series AA, n = 1.456, Cargille). Every time before introducing a solution with analyte, a baseline with flowing PBS/Gly buffer was established for 10 minutes to ensure stability and extract the noise level. Flow-rates and input powers varied for different experiments, but the wavelength was kept constant at λ_0 = 1310 nm. All solutions were filtered through Millex-GP filters (PES membrane 0.22 μm).

3. Results and discussion

3.1 Bulk sensing

In order to find the detection limit for bulk refractive index changes and generally see how the index of a solution affects LRSPP propagation along the Au stripe, the six DDI H_2O/Gly solutions with a 2×10^{-3} RIU increment were sequentially injected into the sensor with 16-MHA (-COOH) covered waveguides (Fig. 3).

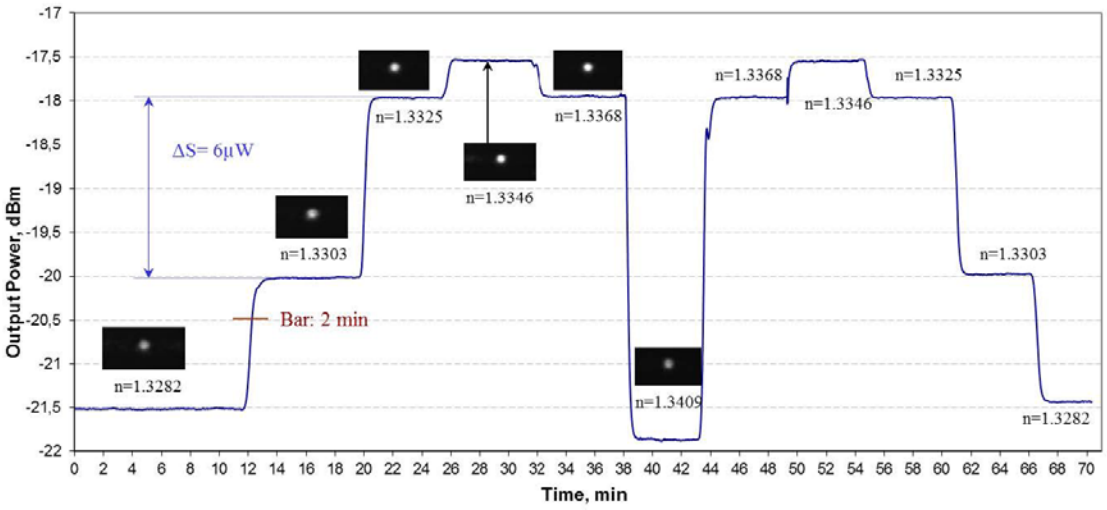

Fig. 3. Response of a Au stripe sensor functionalized with 16-MHA to H_2O/Glycerol solutions with different refractive indices in 2×10^{-3} RIU increments at λ_0 = 1310 nm and a continuous flow-rate of 20 μl /min. The cycle is repeated once.

Two cycles of solution exchange were performed to observe repeatability, ensure stability and the validity of the experiment. Experiments were performed with λ_0 = 1310 nm, an input power of 5 dBm, and a continuous flow-rate of 20 μl/min for all solutions. An image of the mode was taken for each solution to visually compare the intensity of the mode relative to the background. As is evident from Fig. 3, even though the step in refractive index is constant, the corresponding change in output power is not. This is expected as the insertion loss does not vary linearly with the index (or asymmetry - see Fig. 8 of [8]).

The maximum output power is observed for the solution with n = 1.3346, which is closest to the refractive index of Cytop (1.3348), and thus corresponds to the symmetric waveguide case [8]. The largest signal change of ΔS = 6 μW was observed for the step from n = 1.3303 to 1.3325, suggesting a solution with n = 1.3303 as a good choice for the biosensing buffer. The standard deviation of the output power was δ = 6.4 nW over 9 min, yielding a corresponding signal-to-noise ratio ($\Delta S/\delta$) of 942 and implying a detection limit of 2.3×10^{-6} RIU near n = 1.3303 (for $\Delta S/\delta$=1).

In terms of the stability of the system, a slight mismatch in power levels is observed only for the solution injected last (n = 1.3282) and is most likely due to a sudden mild disturbance within the system since the previous solution with n = 1.3303 produces the same output power as in the previous cycle. Overall, a complete regeneration of the signal during the second cycle along with the same output powers for n = 1.3325 and n = 1.3368 indicate very good precision and system stability over at least 65 minutes. Fluid exchange in the channel requires <2 min and which is important to note in order to differentiate signal changes due to bulk effects from those due to binding during biosensing experiments.

3.2 Cell sensing

Red blood cell sensing has been previously demonstrated with a commercial SPR system [30]. The purpose of our experiment is to demonstrate the capability of Au LRSPP waveguides to selectively sense cells based on their cell membrane properties. The Au surface was functionalized with Anti-A antibodies specific to blood cells carrying an A antigen (A-RBCs). The refractive index of PBS/Gly sensing buffer was chosen based on the bulk sensing measurements (Sec.3.1) to be n = 1.3303. The experiment was performed with a concentration of 5×10^7 cells/ml of either A-

or O-RBCs (the latter used as a control) in PBS/Gly buffer, at λ_0 = 1310 nm, an input power of 5 dBm and a varying flow-rate (Fig. 4).

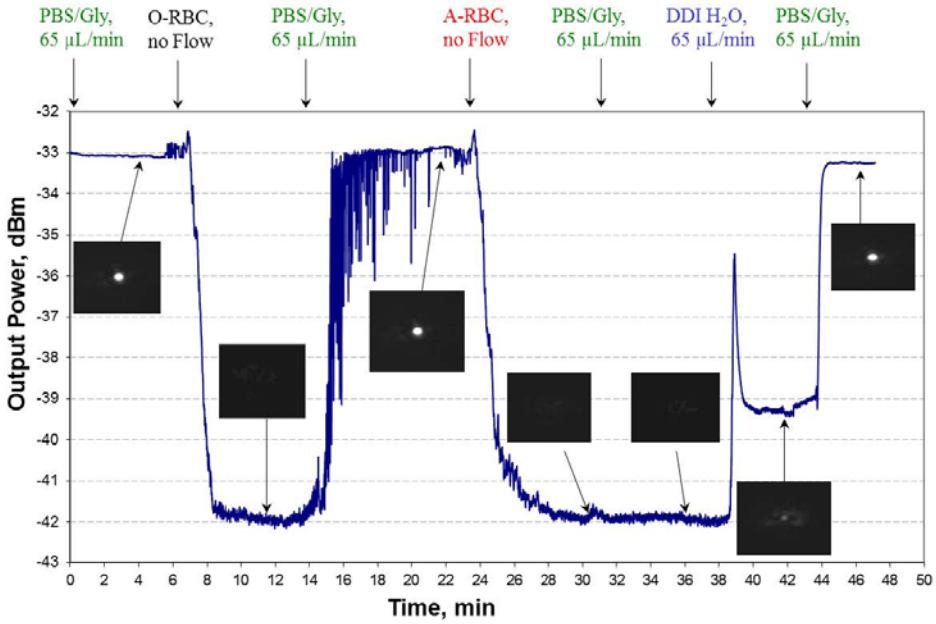

Fig. 4. Response of a Au stripe sensor for selective capture of human red blood cells (RBCs). Surface functionalization: antibodies against blood group A (Anti-A) conjugated to a 16-MHA through a EDC/NHS reaction. O-type RBCs are injected at 7 min and removed at 14 min; A type RBCs are injected at 24 min. Experimental conditions: λ_0 = 1310 nm, input power: 5 dBm and the flow-rate is variable.

A baseline with the PBS/Gly buffer was established over 5 minutes at a flow-rate of 65 µl/min to ensure the stability of the system. At ~6 min, O-RBCs were injected and the flow was stopped to let the cells settle. Due to cells settling on the Au waveguide the output power dropped from −33 dBm to −42 dBm within one minute and the mode practically disappeared. The loss of signal caused by the presence of cells is due to scattering and cut-off of the LRSPP because of the large index asymmetry relative to CYTOP that is induced by the cell membrane (n ~1.5) and the cytoplasm of the cell ($1.33 < n < 1.5$). The cells were allowed to stay on the surface for another 5 minutes under no flow, followed by a 65 µl/min PBS/Gly wash to remove the cells (15 min). At the beginning of the wash high noise is observed which is due to cells lifting from the Au surface, passing close to the Au stripe and briefly blocking the optical pathway. Once the signal was completely recovered and all of the O-RBCs were flushed from the channel (22 min), A-RBCs were injected into the system and allowed to settle for about 8 min (23-31 min). Again, as in the case with O-RBCs, the output power dropped down to −42 dBm due to the formation of a layer of cells on the waveguide. Excess A-RBCs were then flushed under a 65 µl/min flow of PBS/Gly without recovery of the signal, suggesting strong cell binding to the Au surface. Unsuccessful regeneration of the surface with A-RBCs and complete regeneration of the surface with O-RBCs indicates that the Au stripe was effectively functionalized with Anti-A antibodies to capture A-RBCs specifically. Also, because the signal did not change after the wash, a layer of cells is evidently enough to completely block the optical pathway. In order to ensure that the signal loss was only due to the presence of cells on the waveguide and to exclude the possibilities of a drift, or a failure in the interrogation system, the cells were lysed by injecting DDI H_2O (38 min), and the signal recovered by injecting PBS/Gly buffer (44 min).

3.3 Protein sensing

A number of studies have been done on conventional SPR systems to investigate protein adsorption on surfaces functionalized with different SAMs [31]. In particular, a carboxyl-terminated surface was found to be a good adherent for BSA, whereas poly(ethylene glycol)-OH SAM is often used as a protein blocking surface. In this study, a 16-carbon carboxyl-terminated (16-MHA) SAM was used for BSA physisorption and 11-carbon with 3PEG unit hydroxyl-terminated (T-PEG) was used to investigate the prevention of BSA adsorption on PEG-terminated surface. Both responses for BSA adsorption on COOH- and PEG-terminated surfaces are presented in Fig. 5.

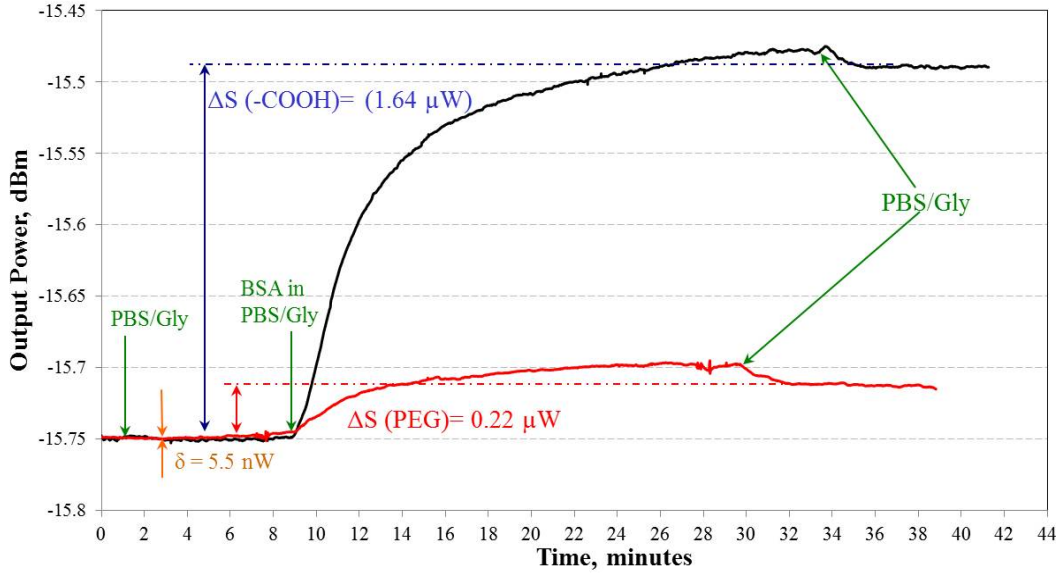

Fig. 5. Response of a Au stripe sensor for BSA physisorption on two surfaces: 16-MHA (carboxyl-terminated, adsorptive surface shown in blue) and PEG (non-specific adsorption preventing surface, shown in red). Experimental conditions: λ_0 = 1310 nm, and a continuous flow-rate of 20 μl/min.

The experiment was performed under the following conditions: λ_0 = 1310 nm, input power = 10 dBm and a continuous flow-rate of 20 μl/min. The refractive index of the sensing PBS/Gly buffer was chosen as n =1.3303 based on the data from Sec.3.1, where the waveguide was found to be most sensitive to refractive index changes. The concentration of BSA (100 μg/ml) was chosen to cause a minimum bulk refractive index change in the buffer, while simultaneously keeping the concentration high enough to avoid diffusion/concentration dependencies. Taking into account our limit of detection for bulk refractive index changes (2.3×10^{-6} RIU) and an index increment of $\partial n/\partial c$=0.185 mm^3/mg (1.85×10^{-7} ml/μg) [32] for proteins, our concentration of 100 μg/ml BSA should only produce a mild change of about 0.02 dBm in output power (bulk step) due to the presence of BSA in the buffer. The experiments were performed on two different devices, one functionalized with 16-MHA and the other with T-PEG.

A baseline under PBS/Gly buffer flow was established for 8 minutes followed by injection of the BSA solution. The excess BSA was washed after a plateau in the response was reached for the –COOH (33 min) and PEG (29 min) surfaces. A mild decrease in signal after the wash is observed which can be attributed to both protein dissociation and a bulk refractive index change. For both surfaces the response follows a typical binding curve (although small bulk refractive index steps during the first two minutes after fluid exchange cannot be neglected). Adsorbed BSA

on the –COOH surface after the wash produced a signal change of ΔS = 1.64 μW with a signal-to-noise ratio of $\Delta S/\delta$ = 297 for δ = 5.5 nW. For the PEG surface, smaller but still significant adsorption was observed with ΔS = 0.29 μW for $\Delta S/\delta$ = 45 and δ = 6.5 nW. BSA physisorption on PEG is not unexpected because a 16-carbon PEG SAM is not considered to be an optimal surface for preventing non-specific adsorption (oligoethylene glycol SAMs for example are known to perform better in this regard [33].).

In both cases (-COOH and PEG terminated surfaces), the power is observed to increase as BSA adsorbs onto the surface. This is consistent with Fig. 4, and the observations in [8]: the sensing fluid (buffer + BSA) has an index that is lower than that of Cytop making the waveguide slightly asymmetric; as BSA adsorbs on the stripe, the high index of the adlayer (n_a ~1.5) formed thereon pulls the waveguide into symmetry thus lowering its insertion loss. Mode computations were carried out on a waveguide within a flow channel in order to verify the aforementioned sensing operation. AFM measurements obtained on an exposed Au stripe within the sensing channel reveal an Au thickness of ~22 nm with a root-mean-squared roughness of ~2.5 nm and a width of ~5 μm. The stripe is located on a Cytop pedestal ~400 nm in height due to slight over-etching during the formation of the channels [27]. The thickness of the lower Cytop cladding is ~8μm and that of the top cladding is ~6.7 μm; the thickness of the fluidic channel is optically infinite due to the comparatively large thickness of the O-ring (Fig. 1). Except for the roughness, all of these features were modeled. The index of Cytop was taken as 1.3348, the index of the sensing fluid as 1.3303, the relative permittivity of Au as −86.06 - j8.322, and the index of Si as 3.5029. The adlayer was modeled as a uniform plane parallel dielectric layer of thickness a and refractive index n_a=1.5 (a and n_a are the equivalent optical parameters of the biochemical adlayer). The characteristics of the LRSPP mode (ssb^0 mode [34]) were computed following [6] as a function of a, with the adlayer located along the top surface of the Au stripe. The coupling factor C (C < 1) was computed following [4] as the overlap between the LRSPP in the fluidic channel and the LRSPP in the fully cladded section.

The power emerging from the sensing waveguide at a reference plane just inside the fully cladded output waveguide is written:

$$\mathrm{P_{out,s}(a) = P_{in,s} C(a)^2 e^{-2\alpha_s(a)L}} \tag{1}$$

where $P_{in,s}$ is the power input into the sensing waveguide at a reference plane just inside the fully cladded input waveguide, and α_s [m^{-1}] is the LRSPP field attenuation coefficient. Both C and α_s depend on the adlayer thickness a. From Eq. (1), the insertion loss (in dB) of the sensing waveguide is written:

$$IL(a) = 2C_L(a) + L \cdot MPA(a) \tag{2}$$

where C_L = $-10\log_{10}(C)$ [dB] and MPA = $20\alpha_s\log_{10}(e)$ [dB/m] is the LRSPP mode power attenuation. Figure 6(a) plots the change in insertion loss $\Delta(a) = IL(a) - IL(0)$ as a function of the adlayer thickness a, along with the change in coupling ($2C_L(a) - 2C_L(0)$) and propagation (L•MPA(a) - L•MPA(0)) losses. Although the change in coupling loss is larger than the change in propagation loss, the latter cannot be neglected and both changes are additive. The coupling loss remains low, from 0.47 to 0.27 dB as a ranges from 0 to 10 nm, indicating that most of the power is flowing as the LRSPP along the metal stripe in the sensing channel. Although Eq. (1) describes a complex dependence on a, P_{out} varies approximately linearly with a over a small range of a; indeed, we have found that the linear model $P_{out,s}(a)/P_{in,s}$=0.0064a + 0.38 represents very well the waveguide modeled for $0 \le a \le 10$ nm (R^2 = 0.9997).

From Fig. 6(a) a decrease in insertion loss of 0.27 dB is noted for a = 4 nm. Returning to Fig. 5 it is noted that the output power increased by 0.26 dB (*i.e.*, the insertion loss of the sensing waveguide decreased by the same amount) due to exposure to BSA on the -COOH terminated surface, suggesting that a BSA adlayer ~4 nm thick was formed on the stripe; this thickness is

consistent with the formation of a close-packed monolayer of BSA [35,36]. By comparison, the output power increase of 0.036 dB observed in the case of the PEG-terminated surface (Fig. 5) suggests that a sub-monolayer of BSA of equivalent thickness ~0.5 nm (plane parallel, homogeneous equivalent layer) was formed thereon (Fig. 6(a)); this is consistent with the protein blocking abilities of such a layer.

The distribution of the E_y field component of the mode is given in Fig. 6(b) for an adlayer thickness of a = 4 nm. The field is observed to penetrate the sensing medium (region above the stripe) to a distance of about 2 μm.

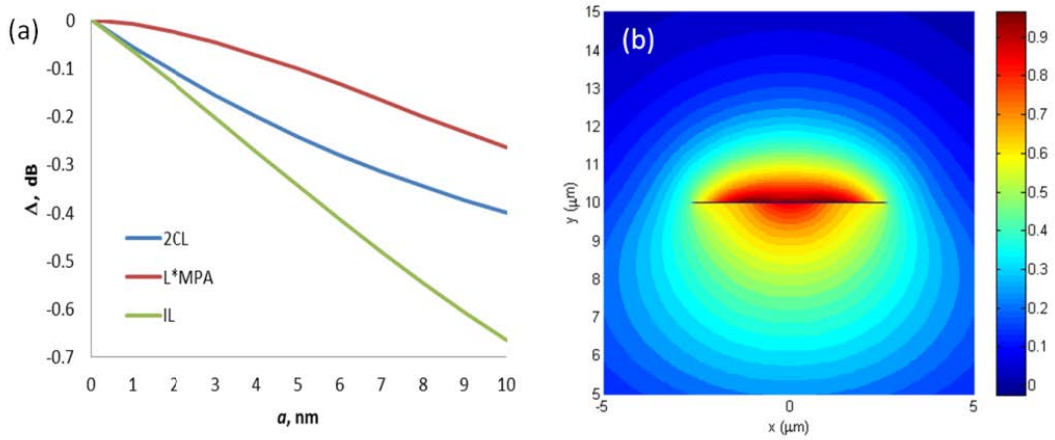

Fig. 6. Theoretical response of the waveguide due to adlayer formation: a) Modeled loss response of a straight waveguide due to the formation of an adlayer thereon of thickness a and refractive index n_a = 1.5. b) Distribution of the E_y field component of the LRSPP (ssb^0 [3]) mode used for sensing.

The surface mass density of the adlayer Γ (in g/m^2) is related to its equivalent optical parameters (n_a, a) via [32]:

$$\Gamma = \frac{a(n_a - n_c)}{\partial n / \partial c} \tag{3}$$

where n_c = 1.3303 is the index of the sensing fluid (buffer + BSA). Using a = 4 nm, n_a = 1.5 and $\partial n/\partial c$ = 0.185 mm^3/mg in Eq. (3) yields Γ = 3669 pg/mm^2 which is consistent with a close-packed monolayer of BSA in a random mixture of side-on (Γ = 1975 pg/mm^2) and end-on adsorption (Γ = 6910 pg/mm^2) [36]. Given that this adlayer was detected with a signal-to-noise ratio of $\Delta S/\delta$ = 297, we estimate the detection limit of our setup in terms of surface mass density to be ΔΓ ~12 pg/mm^2 (for $\Delta S/\delta$ = 1).

4. Conclusion

A novel optical biosensor based on LRSPP waveguides has been demonstrated. Straight Au stripes have been shown to successfully respond to changes in the bulk refractive index of a solution with a detection limit of 2.3×10^{-6} RIU. The selective capture of human RBCs based on type has also been demonstrated where the complete disappearance of the signal due to the formation of cell layer on a waveguide was observed. Protein sensing was carried out with BSA by physisorption on two different surfaces: carboxyl-terminated (protein adsorptive) and PEGylated (preventing non-specific adsorption). For the carboxyl-terminated surface, detection of a close-packed monolayer of BSA was demonstrated with a signal-to-noise ratio of ~300. The detection limit for surface mass density was found to be ~12 pg/mm^2. The experimental results for BSA adsorption are consistent with theoretical modeling. It is expected that these detection limits for bulk and surface sensing can be further reduced as the baseline noise in the interrogating system is

reduced. The biosensors provide a competitive (low-cost, compact) solution for detecting bulk index changes and for sensing biological material over a large range of mass (from cells to proteins).

2.4. Additional Corrections and Comments

The response of the waveguide to the bulk RI changes is non-linear as seen in the Figure 3. This fact is of importance in the case of protein sensing for a valid understanding of binding events. Theoretical response of the waveguide to the adlayer formation shows a linear response for up to a 10 nm adlayer thickness (Figure 6), and is enough to reliably interpret interactions of small to medium proteins. However, in order to understand the response of larger protein interactions, additional modeling of the waveguide response to the adlayer formation would be required.

In Figure 4, RBC cells were allowed to settle and the sensor was washed with PBS/Gly after 5 minutes to allow cells to react with the surface. The timeframe of 5 minutes was chosen based on preliminary experiments with non-structured Au chips (~10 mm×10 mm). Fully gold-covered chip was functionalized with Anti-A using the same protocol as for sensing experiments (*i.e.* carbodiimide chemistry) and placed in a vial with A-RBCs, the cells were allowed to settle and then washed with PBS/Gly buffer using mild agitation. It was experimentally established that 5 minute period was enough for the cells to firmly attach to the surface.

The signal spike that is observed after DDI H_2O injection into the sensor (Figure 4, ~39 min) is due to several factors. Initially the signal is completely blocked by the attached cells, however, when the water is introduced, the RBCs lyse while the water/buffer exchange in the fluidic chamber is incomplete, thus the cells do not block the signal anymore and the total bulk RI is between 1.330 (PBS/Gly) and 1.320 (DDI H_2O). In addition, the released haemoglobin (n~1.55) also increases a total RI in the fluidic chamber, and hence the output power is increased. However, when the fluid exchange is complete, the fluidic chamber is filled with DDI H_2O only, thus the overall RI drops down to ~1.320 decreasing the output power.

Chapter 3

Detection of human red blood cells using straight LRSPP waveguides

3.1. Summary

This chapter provides further investigation into cell sensing encouraged by successful RBC detection in Chapter 2. Four blood groups based on ABO grouping (A, B, AB and O) were tested against anti-A functionalized surface. Each sample of RBCs was injected into the sensor and cells were allowed to settle on the waveguide. Unsuccessful regeneration to the initial baseline by flowing buffer suggested the specific attachment of A- and AB-RBCs, whereas the baseline was easily regenerated for O- and B-RBCs. The LOD for RBC detection was determined by varying A-RBC concentrations and was found to be 3×10^5 cells/ml. Single cell detection was performed by letting a few A-RBCs react to the anti-A waveguide, the cells were counted and based on the signal change, the signal-to-noise ratio was computed to be ~95/cell. The demonstration of surface regeneration up to 10 times was carried out by lysing cells with distilled/deionized water and subsequent re-injection of the sample.

3.2. Contribution

The results provided in this chapter were published as an article in the journal *Biosensors and Bioelectronics*. I rebuilt the setup to improve the stability. The sensors were fabricated by Hamoudi Asiri. I designed and performed all the experiments, analyzed the data and wrote the manuscript. Dr. Berini contributed to the design of the experiments. Dr.Berini and Dr. Chen Wang revised the manuscript.

3.3. Article

The published article is adapted with permission of Elsevier B.V.(*licence number 3713741431933.)* and follows verbatim.

Selective capture of human red blood cells based on blood group using long-range surface plasmon waveguides

Oleksiy Krupin[a], Chen Wang[b] and Pierre Berini[c,d]

[a]Department of Biological and Chemical Engineering, University of Ottawa, 161 Louis Pasteur, Ottawa, Ontario, K1N 6N5, Canada
[b]Department of Pathology and Laboratory Medicine, Mount Sinai Hospital, University of Toronto, 600 University Ave., Toronto, M5G1X5, Canada
[c]School of Electrical Engineering and Computer Science, University of Ottawa, 800 King Edward Ave., Ottawa, K1N6N5, Canada
[d]Department of Physics, University of Ottawa, 150 Louis Pasteur, Ottawa, K1N 6N5, Canada

Abstract

An optical biosensor based on long-range surface plasmon-polariton waveguides is applied to the detection of blood group antigen A on whole erythrocytes. The biosensor consists of straight gold waveguides embedded in CYTOP with an etched fluidic channel. The gold waveguides were functionalized with immunoglobulin G against blood group A (anti-A IgG) by forming a self-assembled monolayer (SAM) of 16-mercaptohexadecanoic acid (16-MHA) and then conjugating the anti-A IgG through carbodiimide chemistry. In order to demonstrate anti-A surface selectivity, solutions of O-type, B-type, A-type and AB-type red blood cells (RBCs) were sequentially injected over an anti-A functionalized waveguide. Surfaces were regenerated by lysing attached cells with distilled/deionized water (DDI H_2O). The efficiency of surface regeneration with DDI H_2O was very high as determined by performing six sequential binding/regeneration cycles of A RBC capture on the same anti-A surface. Also, five solutions of different A RBC concentrations, ranging from 1.14×10^5 cells/ml to 1.83×10^6 cells/ml, were injected over an anti-A surface to determine the limit of detection (LOD), which was found to be less than 3×10^5 cells/ml. Finally, the response produced by a single cell bound to a waveguide was determined by relating the number of bound cells to the response produced, from which the signal-to-noise ratio for single cell detection was determined to be ~95. The waveguides are promising as simple, low-cost and compact transducers, functionalized using standard thiol-based chemistries, for the selective detection of cells.

Keywords: optical biosensor; long-range surface plasmon-polariton; waveguide; human red blood cells; CYTOP; blood group detection.

O. Krupin et al. / Biosensors and Bioelectronics 53 (2014) 117–122

1. Introduction

Major appealing features of optical biosensors are their ability to perform analyte detection without labelling biomolecules and monitoring binding events in real-time (Cooper, 2002). Non-labelled detection (*e.g.* no fluorescent dyes) helps in reducing labour and provides a native environment for molecular interaction. Real-time detection allows for extracting binding kinetics from the data, which is of interest for drug discovery and the pharmaceutical sector. Only a monolayer of a ligand on the surface is required for capturing analyte, substantially reducing the demand for expensive biochemicals, such as antibodies.

Surface plasmon resonance (SPR) biosensors are currently the most common optical sensors on the market. SPR typically utilizes the Kretschmann-Raether configuration, which consists of a prism with a thin layer of gold deposited on one face. A transverse magnetic (TM) optical beam is incident onto the prism at an angle of incidence such that surface plasmons are excited on the gold film at its interface with the sensing solution (SPR angle), and as a result, the intensity of the reflected beam is lowest. The SPR angle is dependent on the local refractive index along the gold-solution interface. Upon analyte binding to the surface, the SPR angle changes producing changes in reflected power which can be tracked and real-time binding events followed (Homola *et al.*, 1999; Lofas, 2004).

Long-range surface plasmon-polaritons (LRSPPs) are surface plasmon waves that can propagate over appreciable lengths along metal slabs or stripes bounded by similar dielectrics (insulator-metal-insulator configuration). The propagation length of LRSPPs is ~2000 μm compared to that of single-interface SPPs which is ~80 μm (Berini, 2009). The penetration depth of the LRSPP fields is ~1 μm, thus significantly larger than that of single-interface SPPs used in conventional SPR (~200 nm), which is advantageous if large objects such as cells must be sensed, or if a dextran matrix is used to increase the loading of small molecules along this dimension (Berini, 2009). LRSPPs have been shown to improve performance in modified SPR prism-based sensors, where higher sensitivity to refractive index changes and bacterial sensing have been demonstrated (Slavik and Homola, 2007; Vala *et al.*, 2009). Furthermore, the detection of changes in induced cellular morphology has been investigated using LRSPPs (modified prism-based SPR) and found to be more sensitive than conventional SPR (Chabot *et al.*, 2012). For LRSPPs to propagate, the refractive index (RI) of the dielectrics along the top and bottom surfaces of the metal slab or stripe must be similar (Breukelaar *et al.*, 2006). Thus, polymers of low RI (CYTOP and Teflon) are usually employed in LRSPP sensors as the bottom cladding, in order to match the RI of biologically compatible fluids which are aqueous and have $n \approx 1.33$ (Slavik and Homola, 2007; Vala *et al.*, 2009; Joo *et al.*, 2010; Dostalek *et al.*, 2007; Guo *et al.*, 2008). Due to the optical confinement of LRSPPs on metal stripes in the plane transverse to the direction of propagation, different integrated circuits such as Mach-Zehnder interferometers, Y-junctions, S-bends and couplers are possible (Charbonneau *et al.*, 2006; Boltasseva *et al.*, 2005). Although single-interface SPPs are more surface sensitive, the increased propagation length of LRSPPs more than compensates for a lower sensitivity in an integrated circuit (Berini, 2008). Furthermore, LRSPPs can be excited by butt-coupling a polarization-maintaining (PM) fibre to the waveguide, allowing for miniaturisation and lower costs. Dielectric waveguides have also been explored for biosensing using silicon nitride (Kinrot, 2004; Shew *et al.*, 2008; Heideman and Lambeck, 1999) and silicon-on-insulator (Xu, 2008).

The sensor, discussed in this paper, consists of Au straight waveguides embedded in CYTOP with an etched fluidic channel to provide fluid access to the waveguide surface. The sensor differs from prism-based LRSPP sensors in that the latter does not provide lateral confinement of the mode and requires a prism-coupling scheme for excitation. Compared to dielectric waveguides, the sensor utilizes Au stripes, and the mode of operation is a surface plasmon. As an application for biosensing, the rationale for using Au is the availability of well-known and well-controlled surface chemistries for functionalization with receptors. Generally, Au

has following advantages: 1) it is historically the most studied surface for functionalization; 2) SAMs using alkane-thiols are quickly formed (80-90% within the first few minutes) and gives a good organized packing, which improves as gold 111 crystallinity increases; 3) it is chemically inert and does not oxidize; 4) the SAM formed on a Au surface is relatively stable and can last for a long period of time (Love *et al.*, 2005); and 5) A complete regeneration down to the Au surface is possible (Balasubramanian *et al.*, 2006). Other advantages of using Au as the sensing surface include the ability to perform electrochemical desorption of SAMs for toposelective functionalization (Tencer *et al.*, 2009, 2012), and the availability of thermo-optical modulation (Gagnon *et al.*, 2006; Nikolajsen *et al.*, 2004), which could be exploited to improve the detection limit. Alternatively, SAM formation on SiO_2 requires alkylsalines which are moisture sensitive and harder to process.

We have shown previously the ability of such (bio)sensing waveguides to detect changes in bulk refractive index, the adsorption of Bovine Serum Albumin on carboxyl- and polyethylene glycol-terminated surfaces, and the selective capture of human red blood cells (Krupin *et al.*, 2013). Conventional SPR sensors have also been used to detect human RBCs based on blood group (Quinn *et al.*, 1997, 2000), and to extract binding kinetics of cells interacting with the functionalized surface (Li *et al.*, 2008). The purpose of this paper is to provide deeper insight into human RBC detection based on blood group A antigen using LRSPP straight waveguides. Au waveguides were functionalized with antibodies against A antigen using carbodiimide chemistry on a 16-MHA formed SAM. Both A and AB RBCs contain A antigen incorporated into the cell membrane while B and O RBCs do not, providing a basis for differentiation between the blood groups. We also perform an A RBC concentration response to determine our limit of detection (LOD), we investigate surface regeneration at the A antibody level, and we demonstrate the detection of a few cells captured by the waveguide. Surface regeneration is important in order to reuse the same sensing device, which results in a reduction of costs for blood grouping. Single cell detection is important in cancer detection, *e.g.*, for detecting rare circulating tumour cells (CTC), when at an early and aggressive stage of cancer, tumour cells leach into the blood stream (Hayes *et al.*, 2006).

2. Materials and methods

2.1 Chemicals

2-Isopropanol semiconductor grade (IPA), 16-Mercaptohexadecanioc acid (HS(CH2)15COOH), *N*-(3-Dimethylaminopropyl)-*N*'-ethylcarbodiimide hydrochloride (EDC), N-Hydroxysuccinimide sodium salt (NHS), acetone HPLC grade ≥ 99.9% and glycerol (electrophoresis grade), Phosphate buffered saline (PBS) 0.01 M, pH 7.4 were obtained from Sigma-Aldrich. PBS solution was prepared by dissolving packaged salts in 1 L of distilled/deionized (DDI H_2O) water. Distilled water was deionized using Millipore filtering membranes (Millipore, Milli-Q water system at 16 MΩ·cm). Packed human red blood cells (groups A, B, O and AB) and antibodies against blood group A (Anti-A, Murine Monoclonal, Series 1, Immucor) were donated by Mount Sinai Hospital (Toronto).

2. 2 Sensing device and fluidic integration

The sensing chip (3.8 mm×6.4 mm) incorporates straight Au waveguides (5 μm wide, 35 nm thick) embedded in CYTOP. The etched fluidic channel is located in the middle of the chip, setting the sensing length to 1.65 mm as sketched in Figure 1.

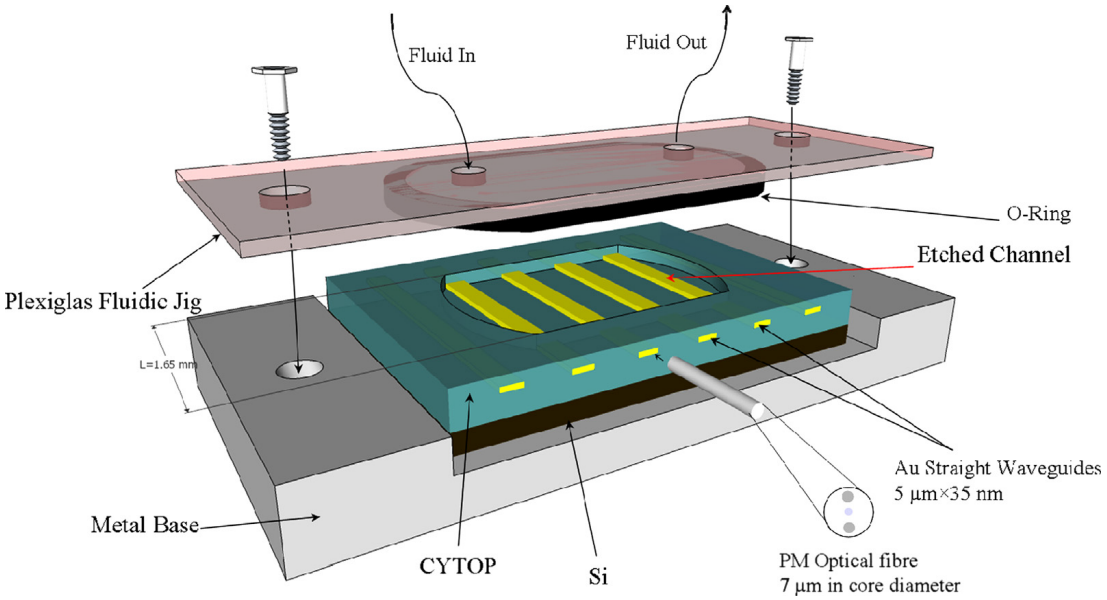

Fig. 1. Schematic representation of the sensor on the metal base with fluidic jig; the volume of the fluidic cell is 20 µL. (Adapted from Krupin *et al.*, 2013.)

For fluidic integration, the device is placed on a metal base and a Plexiglas jig with two holes and an O-ring (fluorocarbon, Apple Rubber Products Inc.), is attached by two Teflon screws to the metal base. Both the Plexiglas jig and the metal base are custom-made. This assembly provides a seal along with fluid access to the etched channel through Pico tubing (550 µm outer diameter, 250 µm inner diameter, IDEX) attached to the holes in the jig. The fluid was supplied by a syringe pump (PicoPlus, Harvard Apparatus).

The device was fabricated by spinning CYTOP on a 4" Si wafer. Au features were lithographically defined thereon, and then another cladding of CYTOP was deposited. Fluidic channels were produced by etching down to the Au surface. The wafer was covered with photoresist and diced resulting in ~300 DIEs per wafer. Fabrication details can be found elsewhere (Asiri, 2012; Chiu *et al.*, 2010). The optical interrogation setup and the general sensing approach are described in (Krupin *et al.*, 2013). The flowrate for cell injection was investigated experimentally and selected as 20 µL/min. Slower flowrates resulted in cells settling and agglomerating in the fluidic tubing, whereas higher flowrates resulted in cells passing over the waveguide without binding (in the case of positive samples).The images of cells on a waveguide during experiment were taken by camera (FMA050, AmScope) installed on a microscope (SMZ645, Nikon).

2.3 Device preparation and functionalization

The dicing photoresist (SPR 220) was removed from the device by two sequential acetone baths (5 min and 30 min) followed by a thorough DDI H_2O and IPA wash. After N_2 drying, the device was cleaned again using an ultrasonic bath (FS20H, Fisher Scientific) in acetone for 30 seconds and then in IPA for 30 seconds to remove any possible debris that could have been formed during dicing. The device was dried with N_2 and placed in a UV/Ozone chamber (PSD-UV, Novascan) to remove any possible organic monolayer from the Au surface.

Prior to device integration with fluidics, the Au waveguides were functionalized with anti-A antibodies. A cleaned device was placed in a 2 mM IPA solution of 16-MHA for 2-24 hours to allow a packed carboxyl-terminated SAM to form. After IPA washing and N_2 drying, the device

was incubated in a DDI H_2O solution of 0.1M EDC/NHS (1:1) for 15 minutes to activate the carboxyl group (Hermanson, 2008). In the final step, the device was cleaned with DDI H_2O, placed immediately into anti-A IgG (used as provided) for ~2 hours to covalently attach IgGs to the surface, then washed with PBS and incorporated into the fluidic setup.

2.4 Analyte preparation

Previously we showed that the highest sensitivity to changes in RI at the waveguide surface occurs with a sensing solution of n = 1.3305 (Krupin *et al.*, 2013). Standard PBS buffer was doped with glycerol (7.235 % w/w) and the RI of the buffer was measured with a prism-coupler based instrument at λ_0 = 1312 nm (Model 2010, Metricon, Prism 200-P1) to be n = 1.3305. Packed RBCs were diluted with working buffer (PBS/Gly) and stored at 4 ^oC. Prior to an experiment, the cells were washed at 400 g in PBS/Gly using a micro-centrifuge (Micromax, Thermo Electric Corp.) 3 times for 2 min. The number of cells was counted using a haemocytometer (1483, Hausser Scientific) and the concentration of RBCs was worked out accordingly. All the solutions except for the ones containing cells were filtered through Millex-GP filters (PES membrane 0.22 µm).

3. Results and Discussion

3.1 Anti-A surface selectivity

The sensing device and RBC solutions (4×10^7 cells/ml for all groups) were prepared as described above. All four blood groups (A, B, AB and O) were used independently as analyte and injected sequentially on the same anti-A functionalized waveguide. A typical response is shown in Figure 2. The flow-rate was set to 65 µL/min during the entire experiment, except when the flow was stopped.

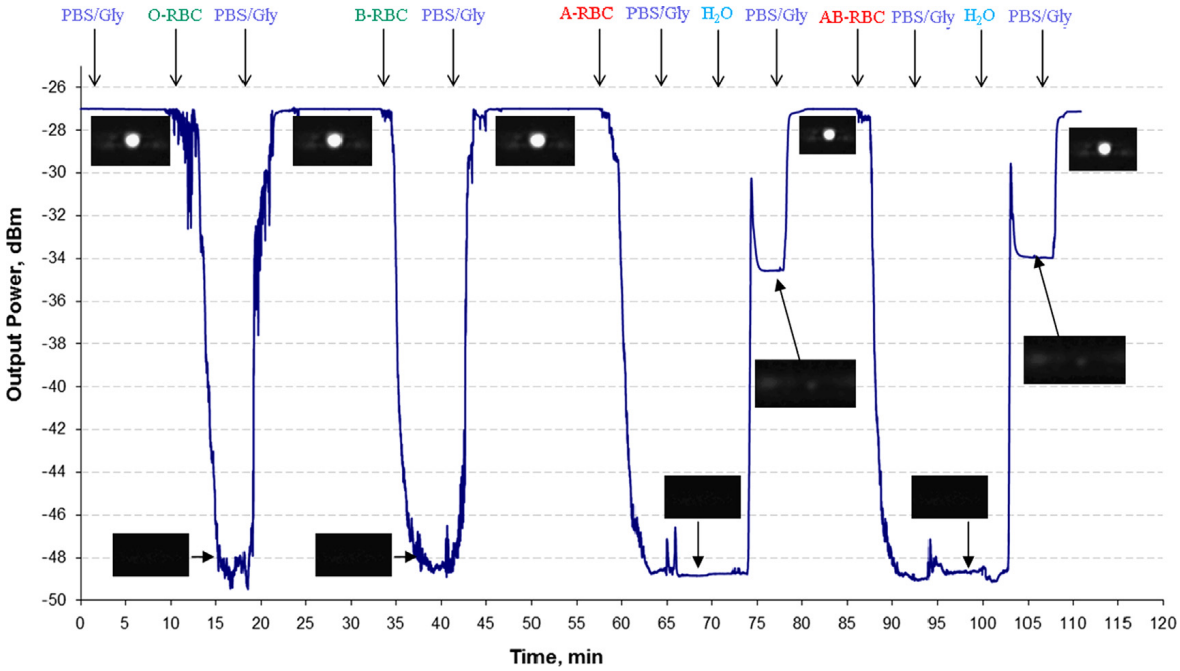

Fig. 2. Response of Au waveguides functionalized with anti-A IgG to RBCs belonging to the four blood groups (O, B, A and AB).

The baseline at -27 dBm output power level was established for 10 minutes, then O RBCs were injected and the flow was stopped to let the cells settle. Upon cell settling the mode

disappeared completely and the power dropped to -49 dBm due to scattering and cut-off of the LRSPP induced by the cells on the waveguide. After 5 min the fluidic cell was flushed with PBS/Gly buffer to remove the erythrocytes and leading to recovery of the initial signal (25 min). The same procedure was performed with B RBCs: the cells were injected, the flow was stopped and after 5 minutes of signal loss, the buffer was re-injected to remove the cells (~35-45 min). Since the signal easily returned to the baseline level upon buffer injection, we conclude that both O and B RBCs did not specifically bind to the surface, and the signal loss was due to cells simply resting on the waveguide.

A RBCs were injected (55 min) and allowed to settle and react with the anti-A surface for 5 minutes. Afterwards, the fluidic cell was flushed with PBS/Gly buffer for ~8 minutes, but the power remained unchanged at -49 dBm throughout this time, indicating specific A RBC binding to the anti-A surface. The cells were lysed with DDI H_2O, and then the signal returned to the baseline level upon injection of PBS/Gly buffer (73-81 min). Lastly, the experiment was repeated with AB RBCs, also indicating specific cell binding (85-110 min). The noise spikes that are observed on O and B RBCs curves during injection/washing steps are due to cells passing across the waveguide and thus interrupting optical (LRSPP) power flow. The spikes that are present right after DDI H_2O injection are due to mixing of PBS/Gly solution and water.

3.2 Surface regeneration

An important property of any biosensor is its ability to be reused. In the present case, regeneration to the anti-A functionalized surface is of interest. DDI H_2O was used as a regeneration fluid, by lysing bound cells (due to low osmotic pressure), and possibly disrupting the antigen-antibody interaction, without damaging anti-A IgGs. We have performed several sequential binding/regeneration cycles in order to assess the potential of this simple regeneration approach - Figure 3 summarizes the results.

Before testing sensors, a large patch of Au (5 cm×5 cm) deposited on CYTOP using the same fabrication method as for the sensors, was tested for regeneration. The patch was functionalized with anti-A in the same way as the sensors, and then the chip was placed in an A RBC solution (6×10^7 cells/ml) and allowed to incubate for ~15 min. The chip was removed from the A RBC solution and placed in clean PBS/Gly buffer (under gentle agitation) until only a monolayer of cells remained. Images were taken using a microscope (BH2-4MA, Olympus) at 50× magnification. Then the chip was washed with DDI H_2O to remove the attached cells (confirmed by microscope inspections) and returned to the container with A RBCs, thus completing one cycle. Nine such binding/regeneration cycles were performed sequentially on the same surface, with images being taken after the first and last A RBC binding, as shown in Figures 3a and 3b. Both images show a high and indistinguishable density of cells per unit area suggesting successful DDI H_2O regeneration.

An anti-A functionalized sensor was tested using the same regeneration strategy applied to six binding/regeneration cycles. All cycles were performed sequentially under a 20 μL/min flow-rate and using a concentration of A RBCs of 4×10^6 cells/ml. A baseline was established over ~5 min, and then A RBCs were introduced. The first and last (6^{th}) binding curves, shown as Figures 3c and 3d, saturate at a similar power level of -39 and -38 dBm, respectively, indicating successful regenerations. To rule out non-specific binding, O RBCs (4×10^6 cells/ml) were injected after the last regeneration and allowed to settle for ~3 min. Subsequent injection of PBS/Gly buffer removed the cells from the waveguide, as indicated by recovery of the signal to the baseline level of -32 dBm in Figure 3e.

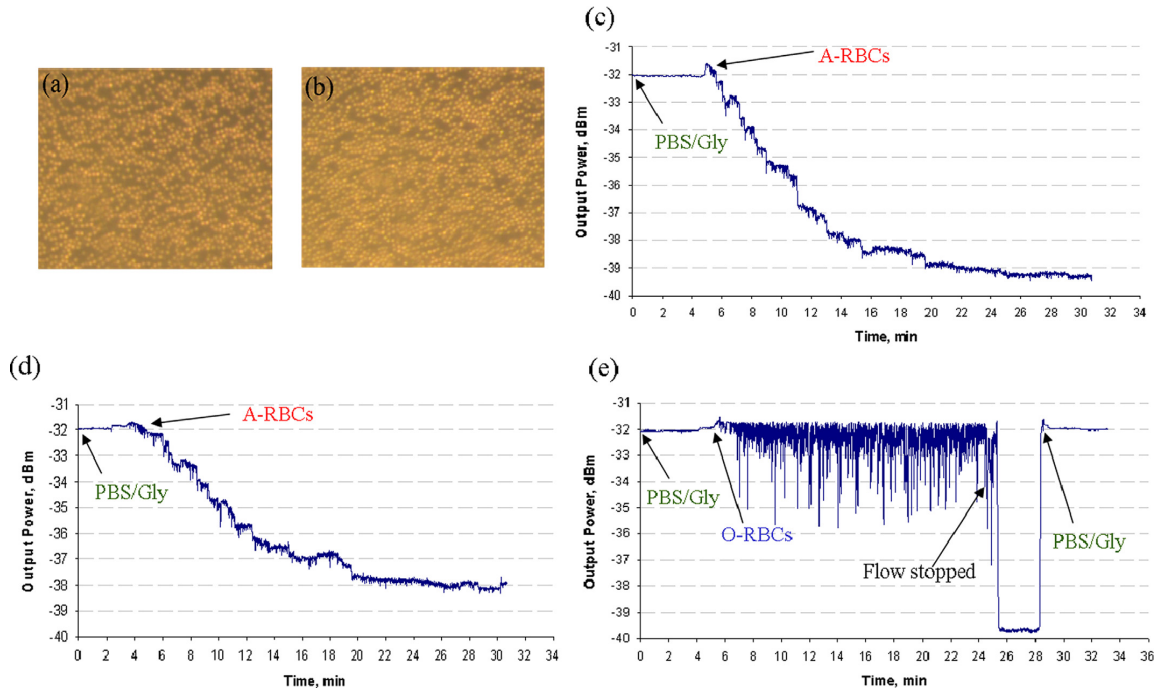

Fig. 3. Regeneration of anti-A IgG functionalized surfaces with DDI H_2O: (a) Large Au patch on CYTOP, 1st binding of A RBCs; (b) Large Au patch on CYTOP, 9th binding of A RBCs; (c) 1st binding curve of A RBCs to a sensor; (d) 6th binding curve of A RBCs to a sensor; (e) Final O RBC injection. All injection flow-rates were 20 µL/min. The concentration of cells used in Parts (a) and (b) was 6×10^7 cells/ml and that used in Parts (c) and (d) was 4×10^6 cells/ml.

3.3 Concentration limit of detection

In order to determine the concentration LOD for our biosensing scheme, solutions having different concentrations of A RBCs in buffer were injected on the same anti-A functionalized waveguide, using the DDI H_2O regeneration scheme of Sec. 3.2 between runs to regenerate the surface.

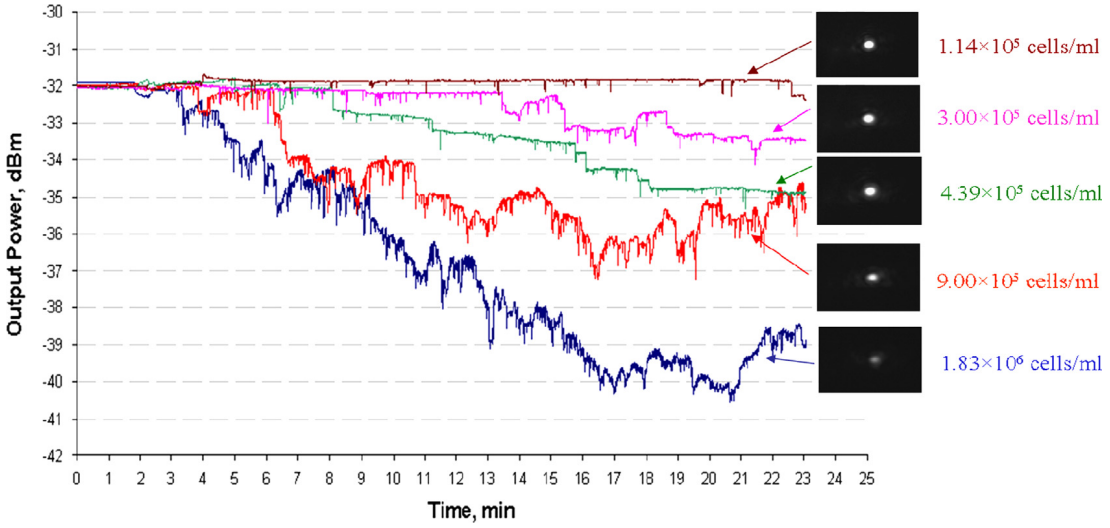

Fig. 4. Concentration responses of A RBC solutions on the same Au waveguide functionalized with anti-A IgG. All flow-rates were 20 µL/min.

The experiments were performed in a sequence of decreasing concentrations starting from 1.83×10^6 cells/ml with the last one being 1.14×10^5 cells/ml, which produced no response within a 20 minute period; Figure 4 summarizes the results. Thus, the LOD can be estimated to be less than 3×10^5 cells/ml, which is several orders of magnitude lower than has been found for SPR (0.33×10^9 cells/ml) (Quinn *et al.*, 1997). The observed noise spikes are due to cells drifting along the waveguide with a velocity higher than required for attachment. The step-like response is likely to be indicative of a single or few cells attaching to the surface. The most vivid example is the curve with 4.39×10^5 cells/ml concentration, where the downward step-like response is observed.

3.4 Single cell detection

The step-like binding response under flow observed in the concentration response (Sec 3.3) suggests that single cell detection is possible. An anti-A functionalized waveguide was exposed to an A RBC solution (8×10^5 cells/ml) under flow (20 μL/min) until a reasonable, but not complete, drop in signal was observed, as shown in Figure 5a. At this point (~23 min) the fluidic cell was flushed with PBS/Gly buffer for 7 min at a flow-rate of 40 μL/min. Microscope images of the waveguide were taken before and after the experiment, as shown in Figure 5b, and the number of bound cells after the experiment was counted. Seven bound cells produced a signal change of 3.05 μW, yielding a 0.43 μW power drop per cell. The baseline noise, taken as the standard deviation of the output power over time, was $\sigma = 4.5$ nW, so the signal-to-noise ratio for capturing a single cell on the waveguide is S/N ~ 95.

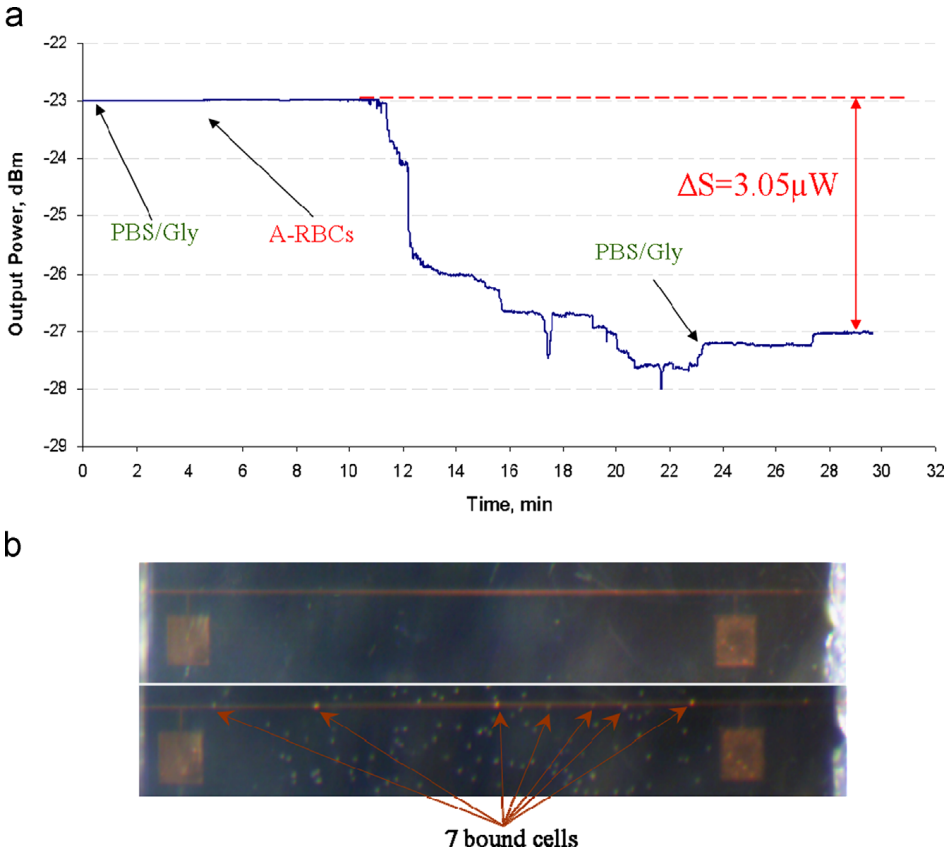

Fig. 5. Detection of single cells on a Au waveguide: (a) binding response of a A RBC solution (8×10^5 cells/ml) injected over an anti-A functionalized sensor; (b) images of the waveguide before (top) and after (bottom) the experiment.

4. Conclusion

An optical biosensor based on straight Au waveguides operating with LRSPPs was applied to the selective detection of human red blood cells. Cells bearing A-antigen (A and AB RBCs) were successfully detected, whereas cells without this antigen (O and B RBCs) served as negative controls. The sensor thus demonstrated an ability to differentiate between blood groups containing A-antigen and blood groups lacking the antigen. Regeneration of the anti-A functionalized surface by injecting DDI H_2O to lyse bound cells was also demonstrated for several sequential binding cycles on the same surface with no significant changes being observed between the first and the last binding responses. The concentration LOD for A RBC detection was found to be less than 3×10^5 cells/ml. Finally, few-cell capture was demonstrated, and the signal-to-noise ratio for single-cell capture estimated as S/N ~ 95.

An advantage of this sensing technique over a standard clinical procedure based on an agglutination test is reduced antibody usage, which is practically insignificant in the sensor compared to an agglutination test. Miniaturization of the sensor is an advantage over conventional SPR sensors. Both of these features can lead potentially to cheap blood grouping procedures. The ability to sense a single captured cell can be of interest in other applications such as environmental sensing of bacteria, or for the detection of rare cells in medical applications.

5. Acknowledgments

The authors gratefully acknowledge NSERC (BiopSys Network) for funding, Ewa Lisicka-Skrzek, Michal Tencer, Asad Khan, Hamoudi Asiri, and Anthony Olivieri for assistance in carrying out the experiments.

References

Asiri, H., 2012. Master's Thesis, Dept. of Chem. and Biological Engineering, Univ. of Ottawa, Ottawa.

Balasubramanian, S., Revzin, A., Sirnonian, A., 2006. Electroanalysis 18, 1885–1892.

Berini, P., 2008. New J. Phys. 10, 105010.

Berini, P., 2009. Adv. Opt. Phot. 1, 484-588.

Boltasseva, A., T. Nikolajsen, Leosson, K., Kjaer, K., Larsen, M.S., Bozhevolnyi, S.I., 2005. J. Lightwave Technol. 23(1), 413–422.

Breukelaar, I., Charbonneau, R., Berini, P., 2006. J. Appl. Phys. 100(4), 43-104.

Chabot, V., Miron, Y., Grandbois, M., Charettea, P.G., 2012. Sens. Actuators B Chem. 174, 94– 101.

Charbonneau, R., Scales, C., Breukelaar, I., Fafard, S., Lahoud, N., Mattiussi, G., Berini, P., 2006. J. Lightwave Technol. 24(1), 477–494.

Chiu, C., Lisicka-Skrzek, E., Tait, R.N., Berini, P., 2010. J. Vac. Sci. Technol. B 28(4), 729–735.

Cooper, M. A., 2002. Nat. Rev. Drug Discov. 1, 515–527.

Dostálek, J., Kasry, A., Knoll, W., 2007. Plasmonics. 2(3), 97–106.

Doyle, G.V., Terstappen, L.W.W.M. 2006. Clin. Cancer Res. 12(14), 4218–4224.

Gagnon, G., Lahoud, N., Mattiussi, G.A., Berini, P., 2006. J. Lightwave Technol. 24(11), 4391–4402.

Guo, J., Keathley, P.D., Hastings, J.T., 2008. Opt. Lett. 33(5), 512–514.

Hayes, D.F., Cristofanilli, M., Budd, G.T., Ellis, M.J., Stopeck, A., Miller, M.C., Matera, J., Allard, W.J., Heideman, R.G., Lambeck, P.V., 1999. Sens. Actuators B Chem. 61(1-3), 100–127.

Hermanson, T.G., 2008. Bioconjugate Techniques, 2nd ed., Rockford, USA.

Homola, J, Yee, S. S., Gauglitz, G., 1999. Sens. Actuators B Chem. 54, 3-15.

Joo, Y. H., Song, S., Magnusson, R., 2010. Appl. Phys. Lett. 97(20), 201105.

Kinrot, N., 2004. J. Lightwave Technol. 22(10), 2296–2301.

Krupin, O., Asiri, H., Wang, C., Tait, R.N., Berini, P., 2013. Opt. Express 21, 698–709.

Li, B., Chen, J., Long, M., 2008. Anal. Biochem. 377, 195–201.

Lofas, S., 2004. Assay Drug Dev. Technol. 2(4), 407–415.

Love, J.C., Estroff, L.A., Kriebel, J.K., Nuzzo, R.G., Whitesides, G.M., 2005. Chem. Rev. 105(4), 1103–1170.

Nikolajsen, T., Leosson, K., Bozhevolnyi, S.I., 2004. Appl. Phys. Lett. 85(24), 5833–5835.

Quinn, J.G., O'Kennedy, R., Smyth, M., Moulds, J., Frame, T., 1997. J. Immunol. Methods 206, 87–96.

Quinn, J.G., O'Neill, S., Doyle, A., McAtamney, C., Diamond, D., MacCraith, B.D., O'Kennedy, R., 2000. Anal. Biochem. 281, 135–143.

Shew, B.Y., Cheng, Y.C., Tsai, Y.H., 2008. Sens. Actuators A Phys. 141(2), 299–306.

Slavík, R., and Homola, J., 2007. Sens. Actuators B Chem., 123, 10-12.

Tencer, M., Nie, H.Y., Berini, P., 2009. J. Electrochem. Soc. 156(12), J386–J392.

Tencer, M., Olivieri, A., Tezel, B., Nie, H.Y., Berini, P., 2012. J. Electrochem. Soc. 159(3), J77–J82.

Vala, M., Etheridge, S., Roach, J. A., Homola, J., 2009. Sens. Actuators B Chem. 139, 59–63.

Xu, D.X., Densmore, A., Delâge, A., Waldron, P., McKinnon, R., Janz, S., Lapointe, J., Lopinski, G., Mischki, T., Post, E., Cheben, P., Schmid, J.H., 2008. Opt. Express 16(19), 15137–15148.

Chapter 4

Detection of leukemia markers in patient serum using LRSPP SWG sensors

4.1. Summary

This chapter presents the demonstration of LRSPP SWG sensors to detect proteins in complex fluid. In particular, the relative abundance of immunoglobulins kappa and lambda light chains was detected in three samples: normal, high kappa content and high lambda content patient sera. Human IgGκ and IgGλ were detected by the corresponding goat anti-human IgGκ and IgGλ. Immunoglobulins were captured by Protein G-functionalized waveguides. Prior to experiments with patient serum, interactions of pure analytes were studied to determine the binding strength of goat anti-human IgGs and their corresponding cross-reactivities. Two sensing approaches were employed in regards of immunoglobulin immobilization on Protein G surface: a) Protein G was functionalized with patient serum first (reverse approach) and b) Protein G was functionalized with goat anti-human IgGs first (direct approach). The kappa-lambda ratios were computed by converting the actual optical responses to the surface mass density. Experiments with pure analyte demonstrated a reasonable binding-strength/cross-reactivity ratio of 15.2 for kappa and 9.0 for lambda in the reverse approach, and 6.4 (kappa) and 3.3 (lambda) in the direct approach. The results for normal patient serum (κ:λ=1.8) agreed with the expected value (κ:λ≈1.7), for high kappa serum the obtained results were lower (κ:λ=3.7) compared to the densitometric data (κ:λ≈12.7) but still out of the normal range, and for the high lambda patient serum the results were λ:κ =9.5, which is higher compared the densitometric data (λ:κ ≈7.0), and also out of normal range. Overall, the LRSPP SWG sensor demonstrated the ability to detect leukemic abnormalities in serum, also showing the reverse approach to be more sensitive.

4.2. Contribution

The results provided in this chapter were submitted as an article to the journal *Lab on a Chip*. The sensors were fabricated by Sa'ad Hassan. I designed and performed all the experiments, analyzed the data and wrote the manuscript. Dr. Berini and Dr. Chen Wang revised the manuscript.

4.3. Article

The submitted article is adapted by permission of The Royal Society of Chemistry and follows verbatim.

Detection of leukemia markers using long-range surface plasmon waveguides functionalized with protein G

Oleksiy Krupin[a], Chen Wang[b] and Pierre Berini[c,d,e]

[a]Department of Biological and Chemical Engineering, University of Ottawa, 161 Louis Pasteur, Ottawa, Ontario, K1N 6N5, Canada
[b]Department of Pathology and Laboratory Medicine, Mount Sinai Hospital, University of Toronto, 600University Ave., Toronto, M5G1X5, Canada
[c]School of Electrical Engineering and Computer Science, University of Ottawa, 800 King Edward Ave., Ottawa, K1N6N5, Canada
[d]Department of Physics, University of Ottawa, 150 Louis Pasteur, Ottawa, K1N 6N5, Canada
[e]Centre for Research in Photonics, University of Ottawa, Ottawa, K1N 6N5, Canada

Abstract

A novel optical biosensor based on long-range surface plasmon-polariton (LRSPP) waveguides is demonstrated for the detection of leukemia markers in patient serum using a functionalization strategy based on Protein G. The sensor consists of thin straight Au waveguides (5 μm×35 nm×3.2 mm) embedded in fluoropolymer CYTOP™ with a fluidic channel etched into the top cladding. B-cell leukemia is characterized by a high B-cell count and abnormal distribution of immunoglobulin G kappa (IgGκ) and lambda (IgGλ) light chains in serum. The detection of leukemic abnormalities in serum was performed based on determining IgGκ-to-IgGλ ratios (κ:λ). Three patient sera were tested: high kappa (HKS, κ:λ ~12.7:1), high lambda (HLS, λ:κ ~6.9:1) and normal (control) sera (NS, κ:λ ~1.7:1). Au waveguides were functionalized with Protein G and two complementary immobilization approaches were investigated: a) the reverse approach, where the Protein G surface is functionalized with patient serum and then tested against goat anti-human IgG light chains in buffer, and b) the direct approach, where the Protein G surface is functionalized with goat anti-human IgGs first and then tested against patient serum. The reverse approach was found to be more effective and robust because Protein G-functionalized surface performs as an "immunological filter" by capturing primarily IgGs out of the pool of serum proteins. For the reverse approach, the ratios measured were 3.7:1 (κ:λ), 9.7:1 (λ:κ) and 1.9:1 (κ:λ) for HKS, HLS and NS, respectively, which compare favorably with corresponding protein densitometry measurements. The respective ratios for the direct approach were 2.6:1 (κ:λ), 2.6:1 (λ:κ) and 1.7:1 (κ:λ). The binding strength and cross-reactivity of goat anti-human IgGs light chains were also determined using pure solutions. The LRSPP biosensor along with the innovative "reverse approach" can provide a low-cost and compact solution to B-cell leukemia screening.

Lab Chip, 2015, **15**, 4156–4165

Introduction

B-cell tumors such as Waldenström's disease, plasma cell neoplasms, chronic lymphocytic leukemia (CLL) and lymphomas, are often associated with monoclonal immunoglobulin production. Currently, there is no standard procedure for early leukemia detection,[1] and most of the diagnostic tests include complex procedures such as blood cell morphology, bone marrow biopsy or flow cytometry. While the normal immunoglobulin G (IgG) kappa–lambda light chain ratio in serum ranges from 1.4–2:1,[2] due to overproduction of monoclonal IgGs in B-cell tumors, either lambda or kappa immunoglobulins can dominate. Recent studies in this area suggested the possibility of detecting B-cell tumors based on the proportion of immunoglobulin kappa (IgGκ) and lambda (IgGλ) light chains in serum.[2–4] In addition, it has been shown that patients with an abnormal light chain ratio are prone to more aggressive disease progression and require early treatment.[5] Traditional tests for the IgGκ:IgGλ ratio are serum or urine protein electrophoresis (SPE, UPE) and turbidimetric methods such as densitometry. Although these methods may be satisfactory, there are existing problems. One example is the case where immunoglobulin bands overlie other proteins (such as transferrin) and are detectable only by immunofixation electrophoresis (IFE), which is nonquantitative.[6] Thus, new methods of immunoglobulin light chain detection in serum are of interest.

Optical biosensors have become appealing in the past 20 years due to their ability to quickly detect biomolecules in real-time without prior labeling. Other additional benefits such as the small consumption of analytical ingredients and no requirements for well-trained personnel make optical biosensors competitive to common clinical diagnostic techniques such as ELISA, flow cytometry or bacterial culture. Still, the main current application of optical biosensors remains in the pharmaceutical field, where kinetics extraction of biomolecular interactions is the main interest.[7] The field of optical biosensors is currently dominated by the methods of surface plasmon resonance (SPR), which utilizes the Kretschmann–Raether configuration.[8,9]

Long-range surface plasmon-polaritons (LRSPPs) are surface plasmon waves that can propagate over appreciable lengths along a thin metal slab or stripe, bounded by dielectrics of similar refractive index (RI), upon optical excitation.[10] The LRSPP propagation length can extend to centimetres, whereas that of single-interface SPR is ~80 μm, so the former provides a longer interaction length with the sample to be measured leading to high-sensitivity.[11] The LRSPP field penetration depth is ~1 μm, and is significantly larger than that of SPR (~200 nm), which provides advantages when sensing large objects such as cells. Furthermore, a thicker layer of hydrogel dextran matrix can be deposited on the waveguide to capture more analyte thus further increasing the sensitivity of an LRSPP sensor.

LRSPP wave propagation along a metal stripe requires that the top and bottom dielectrics serving as claddings have similar refractive indices. Since most biological solutions are aqueous and have a low RI (~1.32), low-RI polymers such as CYTOP (Asahi) and Teflon (Dupont) have been utilized as a bottom cladding to maintain optical symmetry.[12–14]

LRSPPs have been investigated for biosensing by modifying an SPR prism-based sensor with Teflon, demonstrating increased sensitivity for bulk RI sensing,[12] showing a 5.5-fold increase in sensitivity for E. coli detection,[15] and in studying the effect of toxins on HEK-293 cells.[16] Due to wave confinement in the plane transverse to the direction of propagation, various waveguide configurations such as Y-junctions, S-bends and Mach–Zehnder Interferometers (MZIs) can be constructed.[17,18] Au MZIs with one etched arm have been successfully demonstrated for bulk sensing.[19]

The LRSPP biosensor described in this paper consists of a straight Au waveguide (SWG) embedded in CYTOP with a fluidic channel etched into the top cladding to expose the top surface of the Au stripe.[20] The LRSPP wave can be excited by butt-coupling an optical fibre to the waveguide input allowing the sensor to be potentially miniaturized. Our LRSPP sensor has been previously demonstrated for the detection of RI changes in bulk solutions and non-specific bovine

serum albumin (BSA) adsorption.[21] Immunological detection of human red blood cells based on the ABO group demonstrated a limit of detection (LOD) one order of magnitude lower than SPR.[22] Dengue infection detection in patient plasma showed similar and better results compared to ELISA.[23] We also demonstrated the detection of Gramnegative and Gram-positive bacteria in urine.[24] In addition, the sensitivity[25] and optimization[26] of SWG LRSPP sensors has been investigated.

Non-metallic waveguides have also been used for biosensing applications.[27–29] However Au is a preferred surface for biosensing because it is chemically stable, it is the most studied, and it can be easily functionalized with sensing chemistries, especially thiol-based.[30]

Protein G is a streptococcal protein that has a strong affinity to the crystallizable fragment (Fc) of IgG and is commonly used for the purification of immunoglobulins. This property of Protein G becomes even more valuable for planar biosensors where the reacting immunoglobulins orient themselves "upward" thus exposing the fragment antigen-binding site (Fab) to the flowing solution carrying analyte. The application of Protein G for Au surface functionalization with IgG has been well-studied in SPR sensors. Different strategies have been explored for Protein G attachment to Au surface such as covalent attachment to alkanethiol self-assembled monolayer (SAM).[31] However, the simple adsorption of Protein G on Au at room temperature through Au–N interactions has also been shown to be successful for IgG functionalization,[32] and the kinetics of this interaction has been studied using SPR.[33]

The purpose of this study is to demonstrate the ability of LRSPP waveguide sensors to detect abnormalities in immunoglobulin kappa–lambda ratios in leukemic patient sera. Protein G surface functionalization was used for capturing IgGs. Experiments with pure analytes were performed as a proof-of-concept followed by testing of patient sera. Two different testing approaches were taken: the direct approach, where goat anti-human IgGs were injected on the Protein G surface, followed by the injection of patient serum, and the reverse approach, where the patient serum was injected over Protein G surface, followed by the injection of goat antihuman IgGs. We used the reverse approach to perform three repeats for each test. We prefer the reverse approach because it was found to have significant advantages such as: a) Protein G captures primarily IgGs out of the large variety of serum proteins, and b) the last sensing step involves flowing goat anti-human IgGs in clear buffer, which reduces (or completely eliminates) non-specific binding.

LRSPP waveguide biosensors define a new paradigm for the field – they are very sensitive and compact integrated optical structures, leveraging the attractive features of a Au sensing surface. An investigation of such sensors for detecting a relative ratio of similar proteins (immunoglobulins kappa and lambda) in a complex fluid (serum) is of interest. In addition, to our knowledge, only one study has investigated the detection B-cell leukemia based on measuring the κ–λ ratio with a biosensor (SPR).[34] Although strategies based on Protein G-functionalization are known, no attempt has been made to use the Protein G surface to "filter out" immunoglobulins from sera using biosensors. The reverse approach reported in this work suggests this strategy to be beneficial and promising for a variety of detection problems that involve immunoglobulins in complex fluids, irrespective of the biosensor type.

Experimental

Bio(chemicals)

2-Isopropanol (733458), acetone (270725), glycerol (49767), lyophilized bovine serum albumin (A0281), heptane (34873), sodium dodecyl sulfate (71725) and phosphate buffered saline (PBS, P5368) 0.01 M, pH 7.4 were obtained from Sigma-Aldrich. PBS solution was prepared by dissolving packaged salts in 1 L of distilled/deionized ($DDIH_2O$) water. Distilled water was deionized using Millipore filtering membranes (Millipore, Milli-Q water system at 16 MΩ•cm). Purified human IgG/kappa (P80-111) and purified human IgG/lambda (P80-112) were purchased

from Bethyl Laboratories. Both samples contained all the isotypes of IgG. Goat anti-human kappa (GWB-8C381A) and goat anti-human lambda (GWB-298B63) were purchased from GenWay.

Patient samples

Three serum samples were used, collected from two patients with monoclonal immunoglobulin and a normal control. The sera were previously tested at the clinical laboratory of Mount Sinai Hospital, Toronto, Canada: 1) serum with highly abnormal concentration of IgG-kappa (HKS, total [IgG]=21.6 g/L, monoclonal [IgG-kappa]=17.4 g/L); 2) serum with highly abnormal concentration of IgG-lambda (HLS, total [IgG] = 75.2 g/L, monoclonal [IgG-lambda]=60 g/L); and 3) serum with normal ratio of IgG-kappa and IgG-lambda (NS, total [IgG]=17.0 g/L). The data was obtained by protein densitometry – the standard clinical laboratory method that combines serum protein electrophoresis (SPE) for quantification of monoclonal protein and immunofixation electrophoresis (IFE) for identification of κ or λ chains of monoclonal immunoglobulins. The calculated κ–λ ratios for the three samples are presented in Table 1. The average values for the ratios arise from the variations in the distribution of the polyclonal IgGκ and IgGλ, which ranges from 1.4 to 2.0. The use of patient's samples was approved by Institutional Research Ethics Board.

Table 1 Monoclonal and polyclonal immunoglobulins in leukemic and normal patient samples

Patient Sample	Polyclonal IgG, g/ml	Monoclonal IgG, g/ml	Average ratio	Estimated Error
High Kappa Serum (HKS)	4.2	17.4	12.7:1 (κ:λ)	±1.5
High Lambda Serum (HLS)	15.2	60.0	6.9:1 (λ:κ)	±0.5
Normal Serum (NS)	17.0	0	1.7:1 (κ:λ)	±0.3

Sensor description

A wafer, consisting of ~300 sensors was lithographically fabricated,[20,35] diced, and individual dies were used to perform the experiments. The sensing chip (3.2 mm×6.4 mm) is comprised of Au waveguides (5 μm wide, 35 nm thick) embedded in CYTOP (Fig. 1).

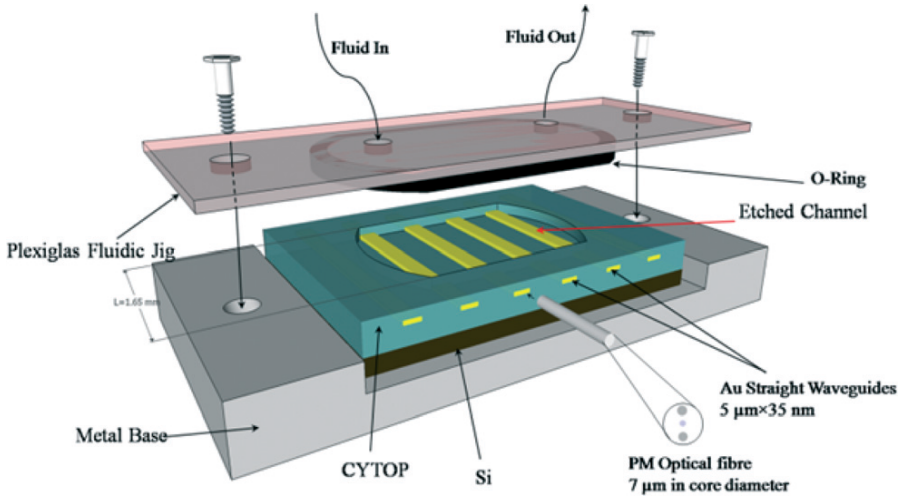

Fig. 1 Schematic representation of the sensor on the metal base with fluidic jig; the volume of the fluidic cell is 20 μL (adapted from ref. 22).

Fluidic channels were fabricated by etching the top CYTOP cladding down to the top Au surface. The plexiglas fluidic jig included a fluorocarbon O-ring (Apple Rubber Products Inc.) to provide a soft seal around the channel and two through holes inside the O-ring area for fluidic access. The whole assembly was fixed by two screws to a metal base. More details on the general sensing approach, the sensor, and our optical interrogation setup can be found in ref. 21 and 22.

Sensor preparation

Initially the whole wafer was covered with photoresist SPR-220 for surface protection during wafer dicing. Fiber-to-waveguide coupling is a delicate procedure, during which any mild contamination on the facet of the sensor can produce significant instability of the output signal. The facets were cleaned in an ultrasonic bath (Fisherbrand FB11201) in heptane for 5 minutes at 37 Hz (50% power). SPR-220 is resistant to heptane, thus keeping the etched surface protected from physical damage during ultrasonic cleaning. SPR-220 was removed by two acetone baths, the first for 5 min, and the second for 30 min, followed by an extensive IPA wash, and drying with N_2. Finally, the sensor was placed into a UV/Ozone chamber (Novascan, PSD-UV4) for 15 min with the UV lamp on and 15 min with the UV lamp off to remove any possible organic contaminants.

Surface functionalization and sensing protocols

As a sensing buffer, a mixture of PBS and glycerol (PBS/Gly) having a RI of n=1.338 was used throughout all experiments.[26] After full integration with fluidics and optics, the Au waveguides were functionalized with Protein G by injecting 50 µg/ml of protein in PBS/Gly for 25 min at a flowrate of 20 µl/min into the fluidic cell.

After Protein G functionalization, one of two different sensing strategies was applied as schematically presented in Fig. 2.

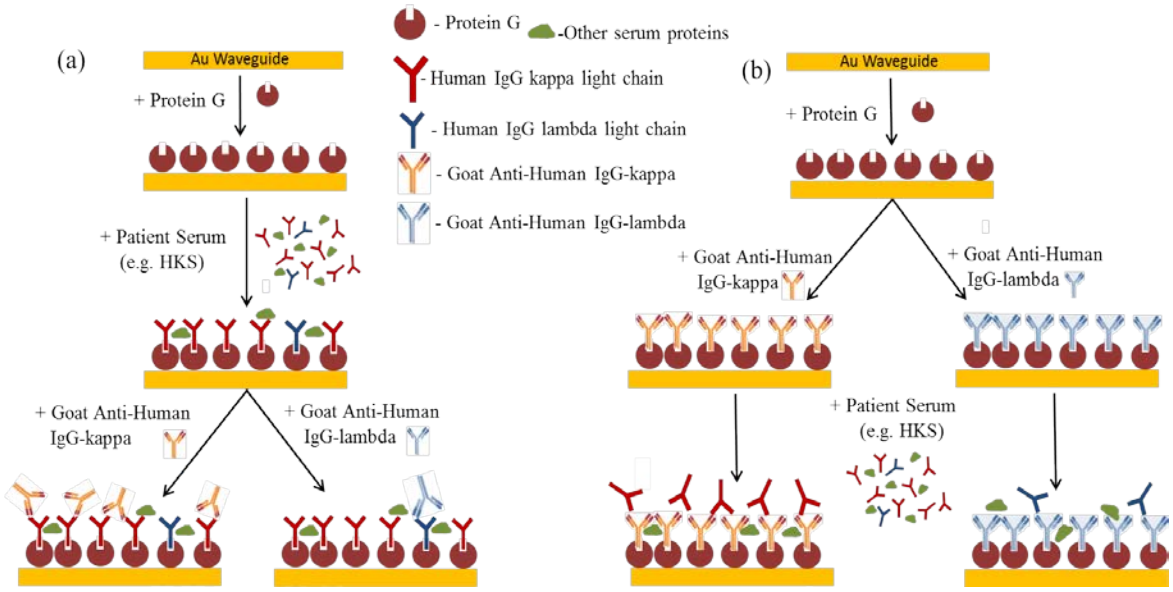

Fig. 2 Schematic illustration of two approaches for patient sample testing. (a) Reverse approach: the Au waveguide is functionalized with Protein G, followed by the immobilization of patient serum (example with HKS is shown), and finally, sensing with recognition goat antihuman kappa light chain IgG. The same waveguide is cleaned down to the Au level, and the whole experiment is repeated but the patient functionalized surface is tested against goat anti-human lambda IgG. (b) Direct approach: the Au waveguide is functionalized with Protein G, followed by the immobilization of goat anti-human kappa IgG, and finally, sensing of patient serum (e.g. HKS). The same waveguide is cleaned down to Au level, and the experiment is repeated but with goat anti-human lambda IgG on the Protein G surface.

The reverse approach (Fig. 2a) first involved the injection of patient serum (1:150 dilution with PBS/Gly) for capturing immunoglobulins out of the sample followed by the injection of goat anti-human light chain IgGs (either anti-kappa or anti-lambda). Patient serum was injected for 40 min at a 10 μl/min flowrate to ensure full surface coverage, and goat anti-human light chain IgGs (50 μg/ml) was flowed for 20 min at 10 μl/min. The direct approach (Fig. 2b), on the contrary, first involved functionalization of the Protein G layer with goat anti-human light chain IgGs (50 μg/ml, 40 min at 10 μl/min) and the subsequent introduction of the patient serum. In the direct approach, the three patient sera had different dilutions to produce a concentration of the prevailing IgG light chain type (kappa or lambda) to 5 μg/ml. Details on the rationale of choosing dilution factors are provided later in this section.

After each experimental stage, the surface was washed with PBS/Gly for ~10 min at a 20 μl/min flowrate to remove unbound analyte and re-establish the baseline. Regeneration of the surface down to the Au level after an experiment was performed by flushing the fluidic cell with SDS (0.5% w/w) for 20 min, then DDI H_2O for 20 min, then the sensor was removed from the fluidic cell, washed with plenty of IPA, dried with N_2 and placed into a UV/Ozone chamber with 15 min lamp on and 15 min lamp off.

During fabrication, small imperfections might result in waveguides not being identical. To eliminate potential inconsistencies in response, the same waveguide was used to test a single patient serum using surface regeneration and full re-functionalization for both approaches. Preliminary experiments and overall analysis suggest the reverse approach to be more sensitive and more robust than the direct approach (see the Results and discussion section). We thus exploited primarily the reverse approach by carrying out three repeats for each experiment. Single measurements were taken for the direct approach. A single batch for each IgG purchased was used throughout all experiments to maintain consistency.

Preliminary experiments for the direct strategy also incorporated a step consisting of the injection of BSA (1 μg/ml in PBS/Gly) to block non-specific binding sites. Blocking was tested after Protein G functionalization or after IgG functionalization (with no prior blocking). BSA injections did not produce any signal changes, indicating the surface was fully functionalized with Protein G or IgGs; the blocking step was therefore eventually abandoned to reduce the overall time of the experimental procedure. The results of BSA blocking are presented in the ESI† (Fig. S1).

Rationale for dilution factors and concentrations

Concentrations of analyte for functionalization of Protein G layer. The kinetics of the Protein G–IgG interaction was studied using SPR, by adsorbing 50 μg/ml of Protein G on a Au surface, then injecting different concentrations of IgG.[33] Their study demonstrated that the Protein G surface was saturated with IgG molecules within 10 min, and the concentration sensitive region was below 667 nM (100 μg/ml). However, the concentration of 337 nM (50 μg/ml) produced a slightly (~3%) lower saturation level. Since in our study the final experimental step is to also capture IgGs, it is highly desirable to maintain the concentration of total IgG in the first injection step to above 50 μg/ml to completely saturate the Protein G surface. Otherwise, the IgGs to be detected in the final step will bind to Protein G instead, thus producing misleading results.

In the direct approach, in order to conserve the antibodies and consequently be able to use the same batches throughout all the experiments, a concentration of 50 μg/ml of goat anti-kappa and goat anti-lambda IgG was used to functionalize the Protein G surface.

The total IgG concentration in an adult is ~10 mg μg/ml.[36] For the reverse approach, all three patient sera were diluted to the dilution factor of 1:150 (serum : PBS/Gly). Thus, a 1:150 dilution of the average adult serum will result in at least ~67 μg/ml of total IgG, which is above the minimum desired value of 50 μg/ml. The 1:150 dilution of the three patient sera resulted in the following total IgG concentrations: NS = 113.3 μg/ml, HKS = 144.0 μg/ml and HLS = 501.3 μg/ml.

Concentrations of analyte used for functionalization and detection. For the direct approach, the last step is the introduction of patient serum. Preliminary experiments suggested that the concentration sensitive region ranges from 1 μg/ml to 10 μg/ml for pure human IgG-κ and IgG-λ, which is similar to the range previously measured by SPR.[34] Thus, for experiments with standard immunoglobulins, 5 μg/ml of either human IgG-κ or IgG-λ were used. For testing patient serum, all three sera were diluted to have a concentration of the dominant IgG light chain of μg/ml: NS = 1:3400 dilution (~5 μg/ml of IgG-κ and ~2.9 μg/ml of IgG-λ), HKS = 1:4000 dilution (~5 μg/ml of IgG-κ and ~0.4 μg/ml of IgG-λ) and HLS = 1:15000 dilution (~5 μg/ml of IgG-λ and ~0.7 μg/ml of IgG-κ).

Preliminary results demonstrated that the concentration-dependent region for the interaction of human IgG and goat anti-human IgG ranged from 5 μg/ml to 30 μg/ml of goat anti-human IgG. In order to ensure full surface saturation for the direct approach, a concentration of 50 μg/ml of the goat anti-kappa and anti-lambda IgGs was used.

Due to the complexity of the experiments, a color scheme was applied to assist in the description of the results. It is presented in Table 2, along with the abbreviations. Generally, all solutions associated with a high content of kappa light chain are colored red and the ones associated with a high content of lambda light chain are blue. Goat anti-human kappa and anti-human lambda are also often referred to as recognition IgGs.

Table 2 Abbreviations and color schemes used throughout the paper

Sample	Abbreviation
High Kappa Serum	HKS
High Lambda Serum	HLS
Normal Serum	NS
Goat anti-human kappa IgG light chain	AK
Goat anti-human lambda IgG light chain	AL
Human IgG-kappa	IgGκ
Human IgG-lambda	IgGλ
Protein G	PG

Results and discussion

Validation with pure analyte

Tests with standard analytes in clean solutions were performed to verify the specificity and cross-reactivity of recognition IgGs (AK and AL). The full experiments are presented in the ESI† (Fig. S2), and summarized in what follows.

Fig. 3 presents the experimental responses for both approaches including cross-reactivity. For the reverse approach, IgGκ- (Fig. 3a) and IgGλ-functionalized (Fig. 3b) surfaces were tested by injecting either AK or AL for 20 min. The responses in both cases are as expected: high signal change for the matching immunoglobulin pairs (IgGκ-AK and IgGλ-AL) and low signal change for the opposite pairs (IgGκ-AL and IgGλ-AK). The same effect is observed for the direct approach (Fig. 3c and d), where the human IgGs were injected over AK- and AL-functionalized surfaces. For the complementary immunoglobulins a clear binding curve is observed confirming a specific and strong interaction. Very little change in baseline is observed for the opposite immunoglobulins suggesting a weak reaction due to cross-reactivity.

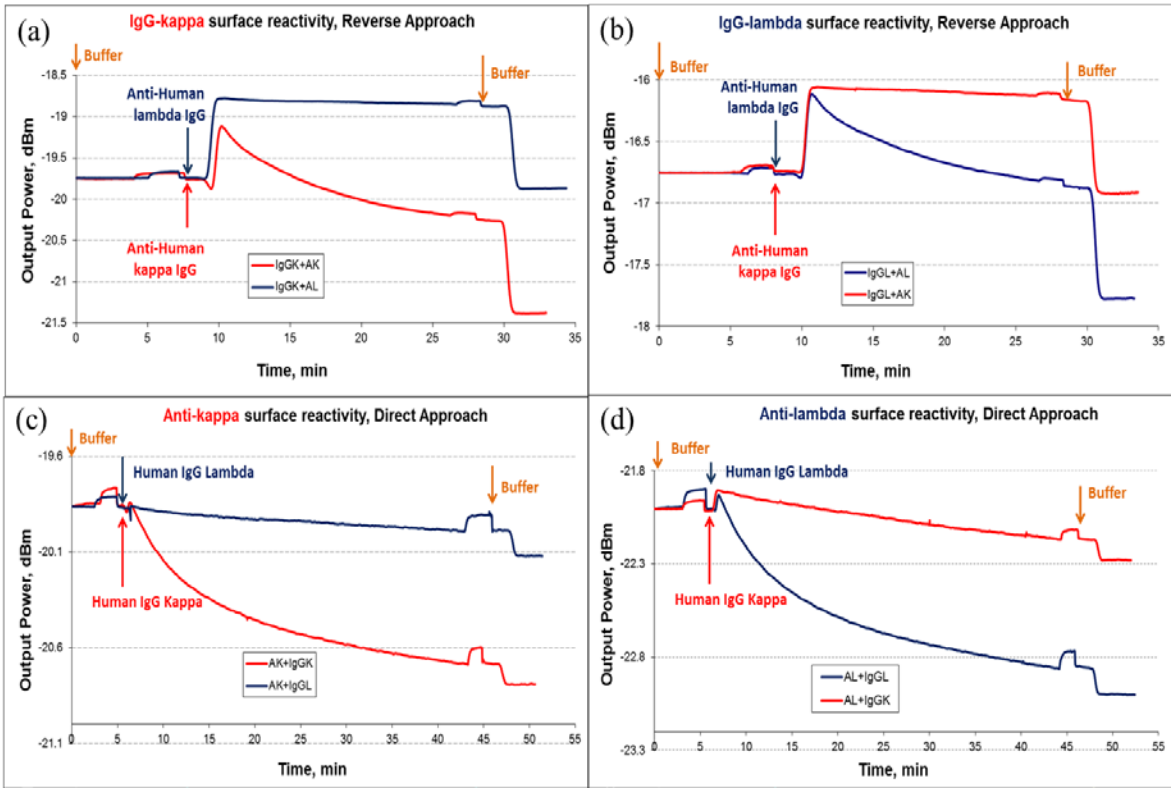

Fig. 3 Real time interaction of human IgG kappa/lambda and goat anti-human kappa/lambda for both approaches. Reverse approach: (a) reactivity of IgGκ-functionalized surface for AK and AL. (b) Reactivity of IgGλ-functionalized surface for AK and AL. Direct approach: (c) reactivity of AK-functionalized surface for IgGκ and IgGλ, (d) reactivity of AL-functionalized surface for IgGκ and IgGλ.

Purchased IgGs (both human and anti-human) already contained a buffer that had a significantly different RI than the sensing buffer (n=1.338). Upon dilution with PBS/Gly of AK and AL down to 50 µg/ml, the overall refractive index remained far from 1.338, producing a bulk step in the responses as seen in Fig. 3a and b. However, for the direct approach, the bulk step is much less significant because the initial solution of immunoglobulins was diluted down to 5 µg/ml. Small bulk steps that can be observed at the beginning and the end of each experiment are due to the stop/start of the flow. CYTOP is a mildly compressible polymer, and when the pressure in the system changes, the top cladding either becomes compressed or decompressed slightly changing the overall refractive index of the top cladding.

The results for both approaches are summarized in Fig. 4. The details of the binding strength calculations are presented in the patient testing section and the computed data are presented in ESI† (Table S3A and S3B). For the reverse approach, the ratio of the complementary response to the cross-reactivity is 15.2 and 9.0 for kappa and lambda surfaces respectively. For the direct approach the ratios are 6.4 and 3.3, which are significantly lower and likely attributed to the limitations of the direct approach when concentrations of the tested analyte (human IgGs) have to be in the concentration-sensitive region, thus the overall response of the matching IgGs is lowered. In addition, the binding strength for kappa-anti-kappa and lambda-anti-lambda interactions is also significantly stronger using the reverse approach compared to the direct approach (~60 g/g vs. ~20 g/g).

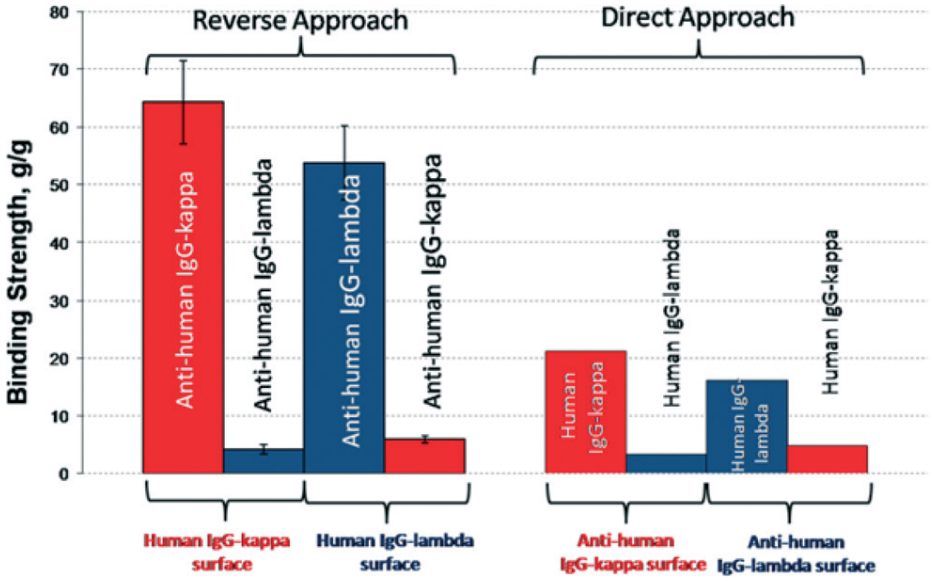

Fig. 4 Validation and comparison of both approaches using standard human IgGκ and IgGλ. The binding strength here is a measure of the mass of the recognition IgG bound, per mass of IgG reacted to Protein G [g/g].

Patient sample testing

Examples of full experiments for both approaches are presented in Fig. 5.

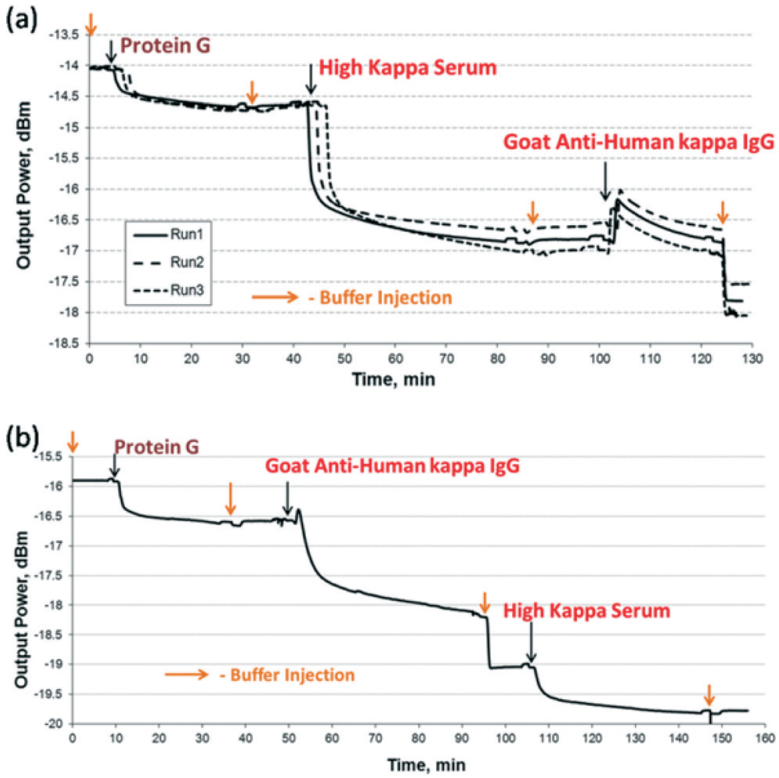

Fig. 5 Full experimental runs for testing HKS using both approaches: (a) reverse approach showing three repeats; (b) direct approach.

For the reverse approach three repeated runs for determining the response of the HKS sample to AK are shown in Fig. 5a. Slight power level adjustments were performed at the initial baseline to align the responses (t = 0, power output ~0.5 dBm), and the timescale for run 2 was adjusted to fit those of the other two runs. Although all three experiments were performed using three different sensors, the repeatability is very satisfactory showing only slight deviations in power output at the end of the experimental runs. One full experimental run for the direct approach, also for the HKS-AK test, is shown in Fig.5b. In all cases the response for Protein G is significantly lower than for the next immunoglobulin functionalization step (~0.5 dB vs. ~2 dB). This is in agreement with the fact that Protein G is a smaller protein with a MW of ~65 kDa compared to IgG (~150 kDa), and since the attenuation of the LRSPP wave on the waveguide is proportional to the adsorbed mass,[26] larger molecules should produce stronger responses.

Visually the main difference between the two approaches is the bulk RI mismatch of the goat anti- human IgG solution, which creates a bulk step at the solution injection point and after the PBS/Gly wash (~100–120 min in the reverse, and ~45–95 min in the direct approaches respectively). It is hard to visually compare the responses of the final binding curves (anti-kappa in reverse and HKS in direct approaches) because of the bulk step in the reverse approach. The fluid exchange time in the system is ~2 min,[21] therefore, during this time period both binding and fluid exchange occur simultaneously, and if there is an RI mismatch between the sensing solution and the sensing buffer, the first two minutes do not represent the actual binding event. In this case, the anti-human kappa IgG solution has a lower RI than the PBS/Gly pulling the overall optical symmetry closer to the CYTOP RI, thus increasing the output power. On the other hand, binding of the IgGs to the surface increases the attenuation lowering the output power. The actual responses for all the three patient samples using both approaches are presented in the ESI† (Fig. S4).

Slight variations in the quality of an individual sensor over the wafer are possible due to uneven gold evaporation, CYTOP distribution on the surface, and other fabrication imperfections. These variations can potentially create differences in the response such as seen in Fig. 5a. Since the purpose of the study is to compare the ratio of the amounts of two different analytes in the same solution, these slight variations can produce misleading results. In order to minimize the effect of variable sensor quality, a response was normalized to the response of the first immunoglobulin functionalization step (goat anti-human IgGs for direct or human IgGs for reverse approaches).

A mathematical expression relating the surface mass density to the power change due to adlayer formation on a straight waveguide is:[26,37]

$$\Delta\Gamma = \frac{1}{k_2}\frac{(n_a - n_c)}{\delta n/\delta c}\left(\frac{P_{out}(a_1)}{P_{out}(a_0)} - 1\right)$$

where $\Delta\Gamma$ is a change in surface mass density, k_2 is a constant that is specific for an individual sensor and is a function of variations in fabrication, n_a and n_c are the refractive indices of the adlayer material and the sensing fluid respectively, $\delta n/\delta c$ is a partial change of refractive index relative to a change in concentration of the adlayer matter in fluid. For proteins n_a ~1.5 and $\delta n/\delta c$ is relatively constant and equal to 0.185 mm^3/mg,[38] $P_{out}(a_0)$ and $P_{out}(a_1)$ are the output powers (in watts) before and after adlayer formation respectively.

Normalization of the response was performed by taking a ratio of $\Delta\Gamma$ of the second IgG step to $\Delta\Gamma$ of the first IgG step:

$$\frac{\Delta\Gamma(analyte)}{\Delta\Gamma(surface)} = \frac{\left(\frac{P_{out}(a_1)}{P_{out}(a_0)} - 1\right)_{analyte}}{\left(\frac{P_{out}(a_1)}{P_{out}(a_0)} - 1\right)_{surface}}$$

The term $\frac{1}{k_2}\frac{(n_a-n_c)}{\delta n/\delta c}$ cancels out because these parameters remain constant during a single experiment. From the biochemical point of view the ratio $\Gamma(analyte)/\Gamma(surface)$, if taken as a function of time, describes the rate of analyte binding to the surface and can be taken as the binding strength. Thus, $\Delta\Gamma(analyte)/\Delta\Gamma(surface)$ is an overall binding strength and is entirely related to the responses produced on the waveguide regardless of the sensor quality. Finally, in order to estimate the κ-λ ratio in a patient sample, the ratio of the binging strengths for kappa and lambda was computed. The detailed results of the aforementioned computations for HKS, HLS and NS are presented in Table 3.

Table 3 Experimental results and computational analysis to obtain κ–λ ratio for HKS, HLS and NS; reverse approach

Patient Sample	Replicate	Step	Response $\left[\frac{P_{ao}}{P_{a1}}-1\right]\times 100$	Binding Strength, g/g $\left[\frac{\Delta\Gamma(\text{recognitionIgG})}{\Delta\Gamma(\text{serum response})}\right]\times 100$	IgG light chain Ratio
High Kappa Serum	1	PG+HKS	**59.96**	**47.09**	3.17 (κ:λ)
		HKS +AK	**28.23**		
		PG+HKS	**58.12**	**14.87**	
		HKS+AL	**8.64**		
	2	PG+HKS	**52.41**	**49.96**	3.37 (κ:λ)
		HKS +AK	**26.18**		
		PG+HKS	**49.97**	**14.81**	
		HKS+AL	**7.40**		
	3	PG+HKS	**51.71**	**48.16**	3.38 (κ:λ)
		HKS +AK	**23.88**		
		PG+HKS	**54.17**	**13.66**	
		HKS+AL	**7.40**		
Average Ratio					**3.31 (κ:λ)**
Standard Deviation					**0.12**
High Lambda Serum	1	PG+HLS	**65.20**	**38.83**	11.32 (λ:κ)
		HLS+AL	**25.31**		
		PG+HLS	**61.06**	**3.43**	
		HLS+AK	**2.09**		
	2	PG+HLS	**64.44**	**33.55**	8.08 (λ:κ)
		HLS+AL	**21.62**		
		PG+HLS	**61.81**	**4.15**	
		HLS+AK	**2.57**		
	3	PG+HLS	**60.32**	**40.06**	9.83 (λ:κ)
		HLS+AL	**24.17**		
		PG+HLS	**62.93**	**4.08**	
		HLS+AK	**2.57**		
Average Ratio					**9.74 (λ:κ)**
Standard Deviation					**1.62**
Normal Serum	1	PG+NS	**64.44**	**41.54**	1.87(κ:λ)
		NS +AK	**26.77**		
		PG+NS	**71.40**	**22.24**	
		NS+AL	**15.88**		
	2	PG+ NS	**65.96**	**42.36**	1.72(κ:λ)
		NS +AK	**27,94**		
		PG+NS	**61.06**	**24.70**	
		NS+AL	**15.08**		
	3	PG+ NS	**58.12**	**44.55**	1.84(κ:λ)
		NS +AK	**25.89**		
		PG+NS	**67.88**	**24.18**	
		NS+AL	**16.41**		
Average Ratio					**1.81(κ:λ)**
Standard Deviation					**0.08**

Computed data for all three sera for the direct approach is presented in ESI† (Table S5).

Replicates for the reverse approach also demonstrate the quality of the experimental repeatability. For the HKS sample the $[P_{out}(a_1)/P_{out}(a_0) - 1] \times 100$ term for the HKS response on the Protein G surface varies from ~50 to ~60, which represents a ~18% difference. However, when taking the ratio of $\Delta\Gamma(analyte)/\Delta\Gamma(HKS)$ for each experimental run, the percentage difference is reduced to ~6% supporting the validity of the "binding strength approach" to analyze the data. For normal and high kappa serum the ratios of κ:λ were calculated, whereas for high lambda serum it was the reverse ratio (λ:κ).

The final results for patient testing are summarized in Fig. 6 (extracted from Tables 3 and S5†) and compared to the data provided by the Mount Sinai Hospital laboratory (Table 1). The yellow stripe indicates the region of normal light chain immunoglobulin ratios: 1.4–2:1 for κ:λ and 0.5–0.7:1 for λ:κ. Overall, both approaches demonstrated the ability to detect abnormality in the IgGκ–IgGλ ratio in patient sera, as well as producing a normal ratio for the control (normal) patient serum.

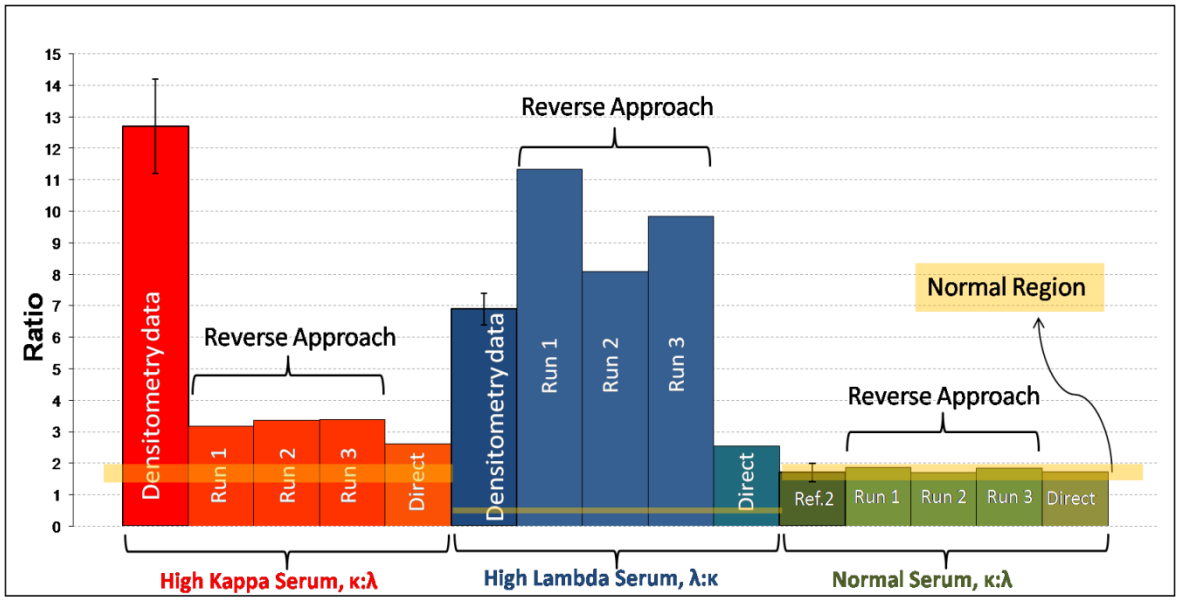

Fig. 6 Kappa–lambda ratios for HKS, HLS and NS obtained using LRSPP sensors. HKS and HLS data are compared to the densitometric data provided by Mount Sinai Hospital laboratory, and NS data is compared to the data in ref. 2.

For HKS, the three experimental repeats of the reverse approach show similar results with the average κ:λ being 3.3:1 and a low standard deviation of 0.12. However, these results are lower than the densitometric result which is 12.7 ± 1.5. This disagreement is not related to the difference in affinities and cross-reactivities of recognition IgGs (Fig. 4), since if it were the case, the experimental ratios would result in higher κ:λ values due to overrated kappa and underrated lambda responses.

For HLS, the results are opposite from those of the HKS, and show a higher λ:κ ratio than the densitometric method: 9.7 ± 1.6 versus 6.9 ± 0.5. Again, as in the case with HKS, this difference cannot be attributed to the difference in anti-kappa and anti-lambda IgG specificities. In this case the sensor demonstrates a higher sensitivity than the densitometric method suggesting possible limitations in the laboratory approach. The possibility of non-specific binding can be excluded because generally it decreases specificity, and consequently, sensitivity. Another potential explanation, which consists of sensing larger immunoglobulins instead of IgG, should also be excluded because Protein G has no affinity for IgM or IgA.[39] For the direct approach the ratios are

lower compared to the reverse approach: 2.6:1 for HKS and 2.6:1 for HLS (Table S5†), however in both cases they are still above the normal range suggesting that the direct approach is also applicable.

Reference data for normal serum was not measured but rather estimated based on the 1.4–2.0:1 κ–λ ratio. The experimental κ:λ was 1.8 ± 0.08:1 (Table 3) and 1.7:1 (Table S5†) using the reverse and direct approaches respectively, and both fall into the normal region.

Evaluation of the approaches

Since Protein G has a strong affinity for IgG, when applied in the reverse approach, the Protein G-functionalized surface performs as an immunological filter to capture specifically the analyte of interest (IgG) from the pool of various proteins in serum. As a result, this approach has great potential for reducing non-specific binding since the final recognition step involves purified IgGs in clean buffer and the binding corresponds to immunoglobulin interactions only. Alternatively, in the direct approach, the final sensing step is serum injection and non-specific binding to the anti-human IgG-functionalized surface may occur. Protein G-IgG interaction is limited by the IgG concentration, where the latter must be greater than 50 μg/ml,[33] thus the only requirement for serum dilution is for it to be less than 1:150 for the reverse approach. This is a significant advantage over the direct approach since no prior information on the kappa and lambda immunoglobulin concentration in patient serum is required. For the direct approach, additional information is necessary: a) the initial concentration of IgGκ and IgGλ in patient sera, and b) the sensitivity of the sensor for human:anti-human IgG interaction so that sera can be properly diluted into the linear range to achieve a significant difference in IgGκ and IgGλ responses. Thus, when the reverse approach is applied, detection of B-cell leukemia becomes independent of other preliminary tests and detection techniques. As a summary, from the practical point of view, any patient serum can be diluted with PBS/Gly using a standard dilution factor (<1:150) and used as is. All of the aforementioned points lead to a higher sensitivity of the reverse approach compared to the direct one, which is confirmed by the experimental results. In addition, due to slower binding kinetics of the final analyte in the direct approach (immunoglobulins in patient serum), a longer exposure is preferable (~40 min vs. ~20 min in reverse approach) suggesting another advantage of the reverse approach where the total experimental time is reduced.

The only minor disadvantage of the reverse approach is that the extraction of kinetics becomes difficult during the final step due to the RI bulk difference of the sensing buffer and goat anti-human IgG solutions. However, this could be resolved by utilizing lyophilized immunoglobulins mixed with a buffer of controlled RI. The interaction kinetics are primarily of interest for research purposes and do not at present impact diagnosis.

Overall evaluation

Our LRSPP biosensor demonstrated the capability of differentiating between three patient sera with various κ–λ IgG ratios. The results were compared to densitometric measurements, and found to agree qualitatively but not quantitatively. Nevertheless, the sensor can be used for leukemia biomarker screening. An important advantage of using the sensor compared to common techniques such as densitometry, electrophoresis gel and ELISA is a low consumption of ingredients. Generally, for a half experiment (e.g. only IgGκ detection), 10 μg of Protein G, ~3 μL of patient serum and 10 μg of antihuman IgG are required. The total experimental run duration can also be decreased from 130 to ~100 min by reducing the time for Protein G and human serum immobilization steps, illustrating a further advantage of the sensor relative to lab techniques. Finally, the sensors could be manufactured cheaply and interrogated with an integrated benchtop unit.

Conclusions

LRSPP biosensors were demonstrated for the detection of leukemic biomarkers in patients with B-cell tumors. Three patient sera (two leukemic and one control) were tested for relative concentrations of kappa and lambda light chain immunoglobulins. Two opposite sensing approaches were evaluated and the results were compared to the densitometric data provided by the serum supplier. The reverse approach, where the Au waveguide was functionalized with patient serum first, was found to be more sensitive and more efficient. Several advantages were found for the reverse approach using a Protein G-functionalization surface: a) specific capture of the immunoglobulins out of the pool of serum proteins, b) reduction in non-specific binding during the last sensing step where purified goat anti-human light chain IgGs in clean buffer are injected, and c) no preliminary tests with patient serum are required to determine the κ–λ IgG ratio. Although the LRSPP results differed quantitatively from the laboratory data, a clear differentiation between normal and leukemic sera was achieved. Along with potential miniaturization, the demonstrated LRSPP biosensor can provide a cheap and rapid solution to B-cell tumor screening for clinical diagnostics.

Acknowledgements

The authors gratefully acknowledge NSERC (BiopSys Network) for funding and are grateful to Ritch Dusome and other employees of Cisco (Ottawa) for a philanthropic donation in support of the work. The authors are also grateful to Ewa Lisicka-Skrzek, Sa'ad Hassan and Anthony Olivieri for assistance in carrying out the experiments.

Notes and references

1 American cancer society, Leukemia-Chronic Lymphocytic, American Cancer Society, 2013.

2 J. A. Katzmann, R. J. Clark, R. S. Abraham, S. Bryant, J. F. Lymp, A. R. Bradwell and R. A. Kyle, Clin. Chem., 2002, 48(9), 1437–1444.

3 A. Bradwell, S. Harding, N. Fourrier, C. Mathiot, M. Attal, P. Moreau, J. L. Harousseau and H. Avet-Loiseau, Leukemia, 2013, 27(1), 202–207.

4 J. P. Campbell, M. Cobbold, Y. Wang, M. Goodall, S. L. Bonney, A. Chamba, J. Birtwistle, T. Plant, Z. Afzal, R. Jefferis and M. T. Drayson, J. Immunol. Methods, 2013, 391(1–2), 1–13.

5 K. M. Charafeddine, M. N. Jabbour, R. H. Kadi and R. T. Daher, Am. J. Clin. Pathol., 2012, 137(6), 890–897.

6 A. R. Bradwell, S. J. Harding, N. J. Fourrier, G. L. F. Wallis, M. T. Drayson, H. D. Carr-Smith and G. P. Mead, Clin. Chem., 2009, 55(9), 1646–1655.

7 M. A. Cooper, Nat. Rev. Drug Discovery, 2002, 1, 515–528.

8 J. Homola, Chem. Rev., 2008, 108, 462–493.

9 S. Lofas, Assay Drug Dev. Technol., 2004, 2, 407–416.

10 P. Berini, Adv. Opt. Photonics, 2009, 1, 484–588.

11 P. Berini, New J. Phys., 2008, 10, 1–36.

12 R. Slavík and J. Homola, Sens. Actuators, B, 2007, 123, 10–12.

13 Y. H. Joo, S. H. Song and R. Magnusson, Appl. Phys. Lett., 2010, 97, 201105.

14 A. W. Wark, H. J. Lee and R. M. Corn, Anal. Chem., 2005, 77, 3904–3907.

15 M. Vala, S. Etheridge, J. Roach and J. Homola, Sens. Actuators, B, 2009, 139, 59–63.

16 V. Chabot, Y. Miron, M. Grandbois and P. G. Charette, Sens. Actuators, B, 2012, 174, 94–101.

17 A. Boltasseva, T. Nikolajsen, K. Leosson, K. Kjaer, M. S. Larsen and S. I. Bozhevolnyi, J. Lightwave Technol., 2005, 23, 413–422.

18 R. Charbonneau, C. Scales, I. Breukelaar, S. Fafard, N. Lahoud, G. Mattiussi and P. Berini, J. Lightwave Technol., 2006, 24, 477.

19 A. Khan, O. Krupin, E. Lisicka-Skrzek and P. Berini, Appl. Phys. Lett., 2013, 103, 111108.

20 C. Chiu, E. Lisicka-Skrzek, R. N. Tait and P. Berini, J. Vac. Sci. Technol., B, 2010, 28(4), 729–735.

21 O. Krupin, H. Asiri, C. Wang, R. N. Tait and P. Berini, Opt. Express, 2013, 21, 698–709.

22 O. Krupin, C. Wang and P. Berini, Biosens. Bioelectron., 2013, 53, 117–122.

23 W. R. Wong, O. Krupin, S. D. Sekaran, F. R. Mahamd Adikan and P. Berini, Anal. Chem., 2014, 86, 1735–1743.

24 P. Beland, O. Krupin and P. Berini, Biomed. Opt. Express, 2015, 6(8), 2908–2922.

25 W. R. Wong, F. R. M. Adikan and P. Berini, Appl. Phys. A: Mater. Sci. Process., 2014, 117, 527–535.

26 W. R. Wong, O. Krupin, F. R. M. Adikan and P. Berini, J. Lightwave Technol., 2015, 33(15), 3234–3242.

27 R. Heideman and P. Lambeck, Sens. Actuators, B, 1999, 61, 100–127.

28 B. Shew, Y. Cheng and Y. Tsai, Sens. Actuators, A, 2008, 141, 299–306.

29 D. Xu, A. Densmore, A. Delâge, P. Waldron, R. McKinnon, S. Janz, J. Lapointe, G. Lopinski, T. Mischki, E. Post, P. Cheben and J. H. Schmid, Opt. Express, 2008, 16, 15137–15148.

30 J. C. Love, L. A. Estroff, J. K. Kriebel, R. G. Nuzzo and G. M. Whitesides, Chem. Rev., 2005, 105, 1103–1170.

31 J. M. Fowler, M. C. Stuart and D. K. Y. Wong, Anal. Chem., 2007, 79, 350–354.

32 B. N. Johnson and R. Mutharasan, Langmuir, 2012, 28(17), 6928–6934.

33 K. Saha, F. Bender and E. Gizeli, Anal. Chem., 2003, 75, 835–842.

34 M. Maisonneuve, C. Valsecchi, C. Wang, A. G. Brolo and M. Meunier, Biosens. Bioelectron., 2015, 63, 80–85.

35 H. Asiri, Master's Thesis, Department of Chemistry and Biological Engineering, University of Ottawa, Ottawa, 2012.

36 J. W. Stoop, B. J. M. Zegers, P. C. Sander and R. E. Ballieux, Clin. Exp. Immunol., 1969, 4, 101–112.

37 O. Krupin, C. Wang and P. Berini, “Strategies for leukemic biomarker detection using long-range surface plasmon-polaritons”, SPIE 9288OW, 2014.

38 A. D. Feijter, J. Benjamins and F. A. Veer, Biopolymers, 1978, 17(7), 1759–1772.

39 L. Bjorck and G. Kronvall, J. Immunol., 1984, 133(2), 969–974.

Supplementary Material

Detection of leukemia markers using long-range surface plasmon waveguides functionalized with Protein G

Oleksiy Krupin[a], Chen Wang[b] and Pierre Berini[c,d,e]

[a]Department of Biological and Chemical Engineering, University of Ottawa, 161 Louis Pasteur,Ottawa,Ontario, K1N 6N5, Canada
[b]Department of Pathology and Laboratory Medicine, Mount Sinai Hospital, University of Toronto, 600University Ave., Toronto, M5G1X5, Canada
[c]School of Electrical Engineering and Computer Science, University of Ottawa, 800 King Edward Ave.,Ottawa, K1N6N5, Canada
[d]Department of Physics, University of Ottawa, 150 Louis Pasteur, Ottawa, K1N 6N5, Canada
[e]Centre for Research in Photonics, University of Ottawa, Ottawa, K1N 6N5, Canada

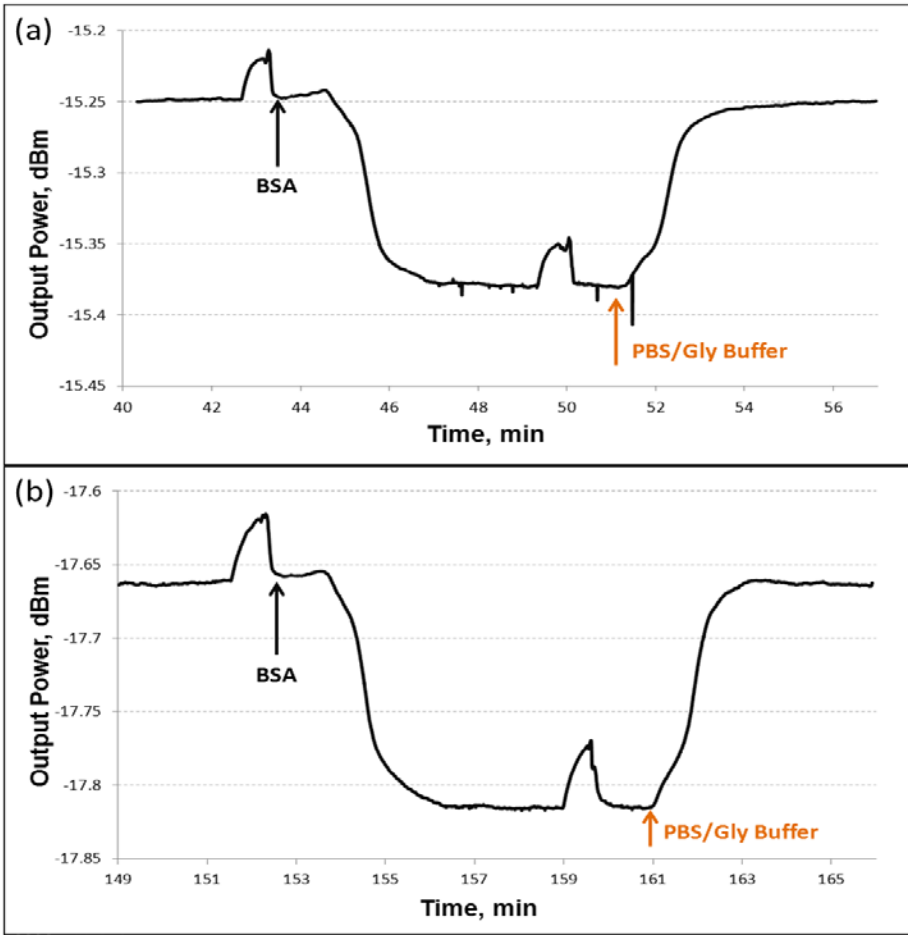

Fig. S1 Blocking non-specific binding sites with bovine serum albumin (BSA, 1 mg/ml): (a) after Protein G functionalization step and (b) after first IgG functionalization step (no prior BSA blocking). Shown results are for validation experiments of human IgGκ:AK using direct approach. Decreased output power after BSA injection is due to the RI bulk effect.

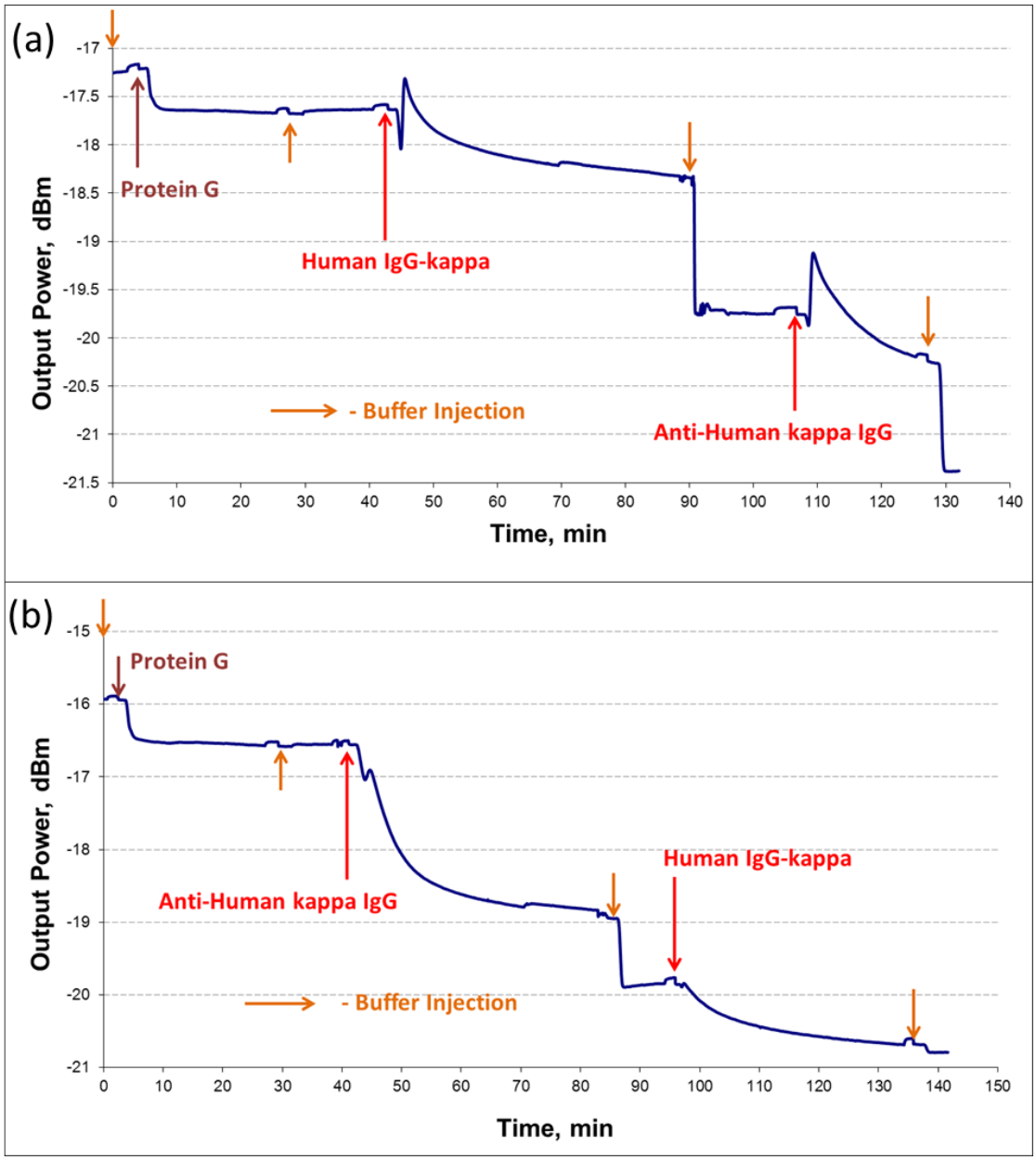

Fig. S2 Full experimental procedures for validation with standard human IgGκ and AK using both approaches: (a) Reverse approach; (b) Direct approach.

Table S3A Experimental results and computational analysis to obtain binding strength for validation of human IgGκ/λ and goat anti-human κ/λ interactions for Fig. 4 in the main text. Reverse approach.

Surface Testing	Test	Replicate	Step	Response $\left[\frac{P_{ao}}{P_{a1}} - 1\right] \times 100$	Binding Strength, g/g $\left[\frac{\Delta\Gamma(analyte)}{\Delta\Gamma(surface)}\right] \times 100$
KAPPA	Kappa Binding Strength	1	PG+IgGκ	**62.55**	**72.27**
			IgGκ+AK	**45.21**	
		2	PG+IgGκ	**86.64**	**58.47**
			IgGκ+AK	**50.66**	
		3	PG+IgGκ	**46.89**	**62.10**
			IgGκ+AK	**29.12**	
	Average Binding Strength				**64.28**
	Standard Deviation				**7.15**
	Kappa-Lambda Cross-reactivity	1	PG+IgGκ	**68.27**	**14.81**
			IgGκ+AL	**2.33**	
		2	PG+IgGκ	**73.78**	**48.16**
			IgGκ+AL	**3.04**	
		3	PG+IgGκ	**36.14**	**13.66**
			IgGκ+AL	**1.86**	
	Average Binding Strength				**4.22**
	Standard Deviation				**0.87**
LAMBDA	Lambda Binding Strength	1	PG+IgGλ	**77.83**	**48.06**
			IgGλ+AL	**37.40**	
		2	PG+IgGλ	**52.05**	**52.54**
			IgGλ+AL	**27.35**	
		3	PG+IgGλ	**43.55**	**60.79**
			IgGλ+AL	**26.47**	
	Average Binding Strength				**53.80**
	Standard Deviation				**6.46**
	Lambda-Kappa Cross-reactivity	1	PG+IgGλ	**75.79**	**5.84**
			IgGλ+AK	**4.42**	
		2	PG+IgGλ	**34.28**	**5.12**
			IgGλ+AK	**1.76**	
		3	PG+IgGλ	**53.11**	**6.95**
			IgGλ+AK	**3.69**	
	Average Binding Strength				**5.96**
	Standard Deviation				**0.75**

Table S3B Experimental results and computational analysis to obtain binding strength for validation of human IgGκ/λ and goat anti-human κ/λ interactions for Fig. 4 in the main text. Direct approach.

Test	Step	Response $\left[\frac{P_{ao}}{P_{a1}} - 1\right] \times 100$	Binding Strength, g/g $\left[\frac{\Delta\Gamma(analyte)}{\Delta\Gamma(surface)}\right] \times 100$
Kappa Binding Strength	PG+AK	**113.80**	**21.24**
	AK+IgGκ	**24.17**	
Kappa-lambda Cross-reactivity	PG+AK	**106.54**	**3.30**
	AK+IgGλ	**3.51**	
Lambda Binding Strength	PG+AL	**162.42**	**16.12**
	AL+IgGλ	**26.18**	
Lambda-Kappa Cross-reactivity	PG+AL	**137.68**	**4.84**
	AL+IgGκ	**6.66**	

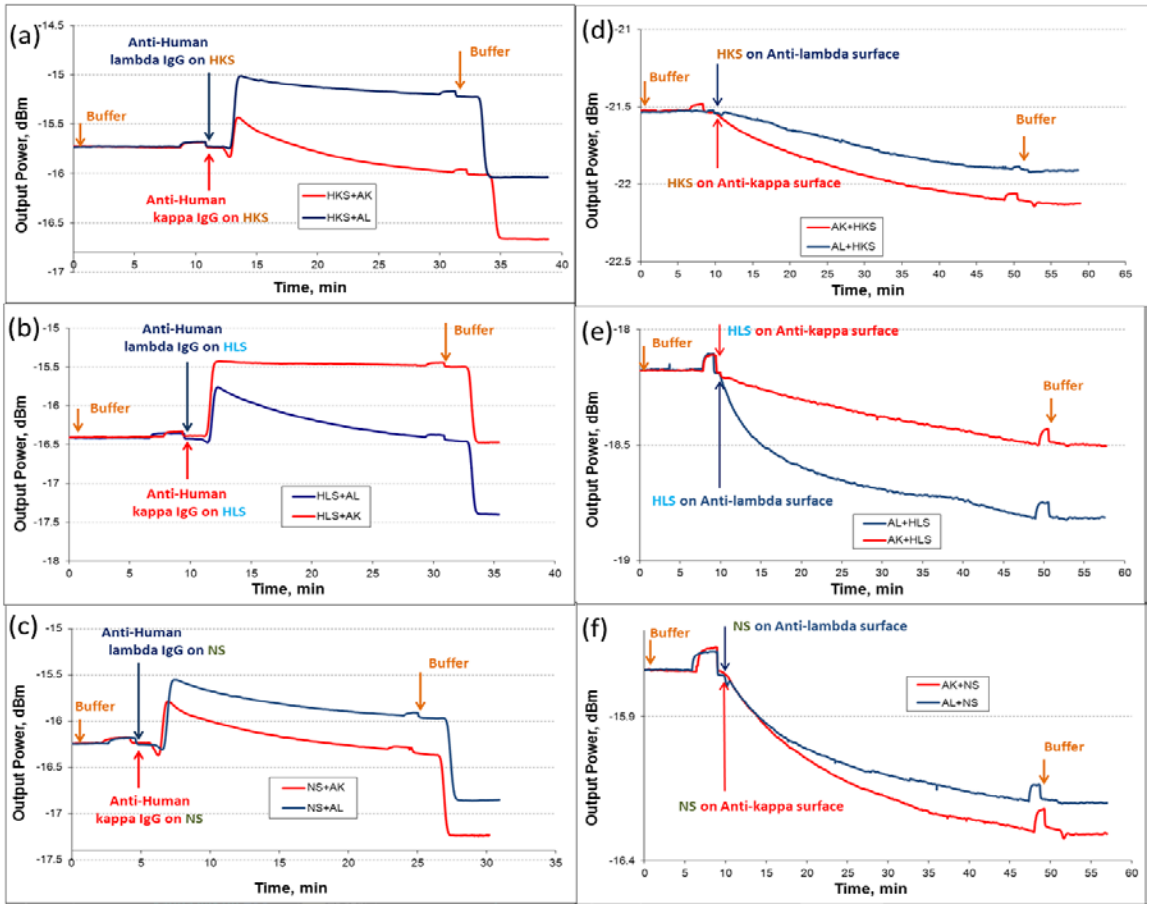

Fig. S4. Real-time responses for HKS, HLS and NS. Reverse approach: (a) Response of HKS-functionalized surface for AK and AL. (b) Response of HLS-functionalized surface for AK and AL. (c) Response of NS-functionalized surface for AK and AL. Direct approach: (d) Response of AK- and AL-functionalized surface for HKS, (e) Response of AK- and AL-functionalized surface for HLS, (f) Response of AK- and AL-functionalized surface for NS.

Table S5. Experimental results and computational analysis to obtain κ-λ ratio for HKS, HLS and NS; direct approach.

Patient Sample	Step	Response $\left[\frac{P_{ao}}{P_{a1}} - 1\right] \times 100$	Binding Strength, g/g $\left[\frac{\Delta\Gamma(recognition\ IgG)}{\Delta\Gamma(serum\ response)}\right] \times 100$	IgG light chain Ratio
High Kappa Serum	PG+AK	**53.11**	**26.41**	2.61 (κ:λ)
	AK+HKS	**14.02**		
	PG+AL	**53.82**	**10.11**	
	AL+HKS	**5.44**		
High Lambda Serum	PG+AL	**84.93**	**19.01**	2.55 (λ:κ)
	AL+HLS	**16.14**		
	PG+AK	**102.77**	**7.44**	
	AK+HLS	**7.65**		
Normal Serum	PG+AK	**52.76**	**27.08**	1.72 (κ:λ)
	AK+NS	**14.29**		
	PG+AL	**71.00**	**15.74**	
	AL+NS	**11.17**		

Chapter 5

Optimization of LRSPP waveguides for biosensing

5.1. Summary

This chapter presents both theoretical and experimental approaches to investigate and optimize the LRSPP waveguide sensitivity for biosensing applications. The theoretical part describes the optimization by modeling of waveguide parameters (thickness, length) and experimental conditions (sensing buffer RI). Optimal designs suggested a potential detection limit of < 0.1pg/mm^2. The experimental part investigates the system noise and the effects of sensing buffer refractive index on the waveguide sensitivity. Investigation of the system noise was performed by varying the input power into the sensor and was found to be independent of the optoelectronics. The effect of the buffer RI was studied by adsorbing BSA in buffer of different refractive indices on a bare Au waveguide. The minimum experimental LOD was found to be 4.1 pg/mm^2, however a better performance can be obtained by reducing the system noise (1.7 pg/mm^2).

5.2. Contribution

The results provided in this chapter were accepted as an article in the *Journal of Lightwave Technology*. The sensors were fabricated by Sa'ad Hassan. I performed and analyzed the experiments in the experimental section. Theoretical modeling and analysis

was performed by Wei Ru Wong. I wrote the manuscript for the experimental section and Wei Ru Wong wrote for the theoretical section. Dr. Berini revised the manuscript.

5.3. Article

Copyright statement from IEE: **The IEEE does not require individuals working on a thesis to obtain a formal reuse license, however, you may print out this statement to be used as a permission grant:** *Requirements to be followed when using an entire IEEE copyrighted paper in a thesis:*

Reprinted, with permission, from [Wei Ru Wong, Oleksiy Krupin, Faisal Rafiq Mahamd Adikan, and Pierre Berini, Optimization of long-range surface plasmon waveguides for attenuation-based biosensing, Journal of Lightwave Technology, (2015)].

The article follows verbatim.

Optimization of long-range surface plasmon waveguides for attenuation-based biosensing

Wei Ru Wong, *Student Member*, IEEE, **Oleksiy Krupin**, **Faisal Rafiq Mahamd Adikan**, and **Pierre Berini**, *Fellow*, IEEE

W. R. Wong and F. R. Mahamd Adikan are with the Integrated Lightwave Research Group, Department of Electrical Engineering, University of Malaya, Kuala Lumpur 50603, Malaysia.

O. Krupin is with the Department of Biological and Chemical Engineering, University of Ottawa, Ottawa, ON K1N 6N5, Canada.

P. Berini is with the School of Electrical Engineering and Computer Science, Department of Physics, and Centre for Research in Photonics, University of Ottawa, Ottawa, ON K1N 6N5, Canada.

Manuscript received March 4, 2015; revised April 28, 2015; accepted May 5, 2015. Date of publication May 7, 2015; date of current version June 20, 2015.

Abstract

The design and optimization of straight long-range surface plasmon waveguides to maximize attenuation surface sensitivity in biochemical sensing applications is discussed. The sensor consists of a Au stripe embedded in CYTOP, with a microfluidic channel etched into the top cladding to expose the surface of the Au stripe and define the sensing channel. The attenuation α_s of the structure changes as a biological adlayer grows on the Au surface. The dimensions of the stripe (thickness, width), the sensing length and the refractive index of the sensing buffer were varied in order to understand their impact on sensor performance. The attenuation sensitivity $\partial\alpha_s/\partial a$ dominates over a wide range of waveguide designs, so we define a parameter $K = (\partial\alpha_s/\partial a)/\alpha_s$ where maximizing $|K|$ and selecting the optimal sensing length as $L_{opt} = 1/(2\alpha_s)$ maximizes the overall sensitivity of the structure. Experimental results based on observing the physisorption of bovine serum albumin (BSA) on bare Au waveguides agree qualitatively and quantitatively with theory. Detection limits of $\Delta\Gamma_{min} < 0.1$ pg/mm^2 are predicted for optimal designs, and a detection limit of $\Delta\Gamma_{min} = 4.1$ pg/mm^2 (SNR = 1) is demonstrated experimentally for a sub-optimal structure.

Index Terms—Attenuation, biosensor, optimization, sensitivity, surface plasmon.

JOURNAL OF LIGHTWAVE TECHNOLOGY, VOL. 33, NO. 15, AUGUST 2015

I. Introduction

Current clinical detection techniques such as ELISA and flow cytometry are based on fluorescence detection, which requires labelling of biomolecules, well-trained personnel, and often many hours (or days) to perform detection. Optical biosensors, on the other hand, are label-free and provide responses in real-time, and furthermore require only a small amount of analytical ingredients which is advantageous as the latter can be very expensive (*e.g.*, antibodies). Real-time

detection is especially useful if the interaction kinetics of a biochemical reaction are of interest [1]. The field of optical biosensors is dominated by the methods of Surface Plasmon Resonance (SPR). SPR biosensors utilize the Kretschmann-Raether configuration, which is comprised of a prism with a thin Au layer deposited on one side, integrated fluidics and a CCD detector [2, 3].

Long-range surface plasmon polaritons (LRSPPs) are transverse magnetic (TM) propagating surface waves supported by a thin metal stripe or slab bounded by dielectrics of similar refractive index (insulator-metal-insulator) [4]. The LRSPP propagation length can extend to centimetres, which is significantly longer than the propagation length of single-interface SPPs (~80 μm), but with reduced confinement. For biosensing applications the reduced confinement leads to a lower modal sensitivity, but the longer propagation length means that a longer sensing surface can be used. As the propagation length of LRSPPs increases more rapidly than the confinement reduction, sensors with a better overall sensitivity compared to SPR are possible [5]. Also the penetration depth of LRSPPs is larger than that of single-interface SPPs (~1 μm *vs.* ~200 nm), which provides additional advantages such as the ability to observe changes occurring inside biological cells [6], or capturing more analyte (*e.g.* protein) perpendicular to the sensing surface via the use of a dextran hydrogel matrix. LRSPP sensing has been investigated by modifying a conventional SPR prism-based sensor with Teflon, leading to significant improvements in bulk sensing [7] and the demonstration of E.*Coli* detection [8].

In order to maintain the optical symmetry of the mode along the waveguide, the dielectrics surrounding the metal stripe must have a similar refractive index (RI). Since biologically compatible sensing fluids are generally aqueous and have a low RI (~1.32), polymers with a low RI are required as the bottom cladding, with the most common ones used being fluoropolymers CYTOP (Asahi) and Teflon (Dupont) [7, 9, 10]. The sensor of interest in this paper consists of a straight Au waveguide embedded in CYTOP with an etched channel for sensing. LRSPPs can be easily excited by butt-coupling an optical fibre to the waveguide allowing this structure to be potentially miniaturized. Non-metallic waveguides have also been used for biosensing applications [11-13], although Au is preferred as a sensing surface as, *e.g.*, thiol-based surface chemistries are easily applied [14].

We previously demonstrated LRSPP straight waveguide (SWG) biosensors to be capable of detecting small changes in the bulk RI of solutions and the non-specific adsorption of Bovine Serum Albumin (BSA) [15]. Immunological blood typing of human red blood cells was also demonstrated with a limit of detection (LOD) one order of magnitude better than that of an SPR sensor [16]. Dengue antibody detection in patient plasma was also demonstrated and the results were found to be comparable to, or better than, those obtained using ELISA [17]. The sensitivity of SWG LRSPP biosensors was discussed in [18], however, optimization of the biosensors was not discussed and supporting experiments were not available.

LRSPPs are confined to the waveguide in the plane transverse to the direction of propagation making it possible to construct various integrated circuits such as Y-junctions, S-bends and Mach-Zehnder Interferometers (MZIs) [19, 20]. Au MZIs embedded in CYTOP with one arm etched to create a microfluidic channel have been successfully tested for refractive index changes in solution [21]. Although such sensors hold the promise of greater sensitivity, they are not as simple to fabricate and operate as SWG sensors.

In this paper we report a theoretical model for the sensitivity of SWG LRSPP biosensors aiming to optimize their performance. We consider the effect of various structural parameters and of the RI of the sensing buffer on performance. We also give experimental results corroborating some of our theoretical findings, and we discuss noise contributions to our baseline signals. The theoretical results are presented in Section II, and the experimental results in Section III. A brief conclusion is presented in Section IV.

II. Theoretical

A. Sensor Structure

Our straight LRSPP waveguide biosensor is illustrated in Fig. 1. The structure is fabricated on a silicon (Si) wafer. The waveguides which comprise a thin Au stripe of width w and thickness t are embedded in CYTOP claddings. The thickness of the top and bottom cladding is 8 and 6.7 μm, respectively. A fluidic channel of sensing length L is etched down to the Au stripes through the top CYTOP cladding. Due to slight over-etching, the Au stripe is situated on a pedestal of height ~400 nm. During a biosensing experiment, a sensing fluid of refractive index n_c which carries the analyte of interest will be passed through the sensing channel. As analyte binds to the surface of the Au stripe it forms an adlayer. The adlayer is modelled as a thin uniform layer of thickness a with a RI of n_a = 1.5 which is typical of biochemical material [5].

The finite element method (FEM) was used to model the sensor structure at an operating wavelength of λ_0 = 1310 nm (exp(+$j\omega t$) time-harmonic form implied). The modal characteristics of the LRSPP propagating along the cladded and sensing sections were computed and used to quantify the sensing performance of the structure. The RI of CYTOP and Si at our wavelength of interest is 1.3348 [22] and 3.5029 [23], respectively, and the relative permittivity of Au is -86.06 - j8.322 [23]. The RI of the sensing fluid n_c can be easily manipulated by mixing glycerol with phosphate buffered saline (PBS) in different proportions. The RI of the sensing fluids considered in the theoretical part of this study are slightly below (n_c = 1.3303), equal to (n_c = 1.3348) and slightly above (n_c = 1.3393) the RI of CYTOP. RIs near these values were used in the experiments.

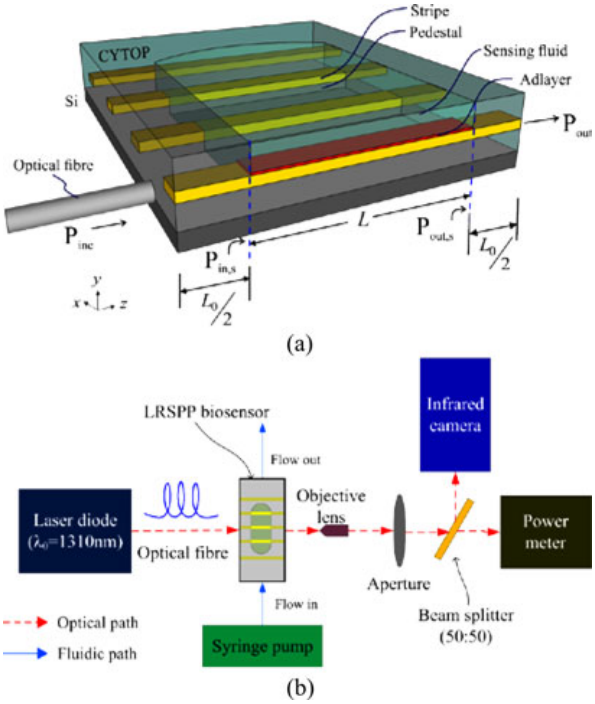

Fig. 1. (a) Schematic of the LRSPP straight waveguide biosensor. The Au stripe (yellow) is of thickness t and width w, and the adlayer (red) forming on the Au stripe is of thickness a. (b) Schematic of the test set-up.

B. Surface sensitivity, mass density and detection limit

The incident light of power P_{inc} emerges from a polarisation-maintaining single-mode optical fibre aligned to the sensor input, as illustrated in Fig. 1. The polarisation of the incident light is aligned to the TM-polarisation of the LRSPP. The LRSPP then propagates in the +z direction along the input access waveguide of length $L_0/2$, the sensing section of length L, and the output access waveguide of length $L_0/2$ (both access waveguides are embedded in Cytop). The output power from the sensor (P_{out}) is then:

$$P_{out}(a) = P_{inc} \cdot |C_i|^2 \exp(-2\alpha L_0) \cdot |C(a)|^4 \exp(-2\alpha_s(a)L) \quad (1)$$

where C_i is the overlap factor between the field of the optical fibre and the LRSPP field at the input facet of the sensor [20], α is the LRSPP field attenuation coefficient in the cladded sections, $C(a)$ is the overlap factor between the LRSPP fields in the input or output access waveguides and the sensing waveguide, and $\alpha_s(a)$ is the LRSPP field attenuation coefficient along the sensing waveguide. Although not explicitly shown in (1), it is noted that $C(a)$ and $\alpha_s(a)$ also depend on the

RI of the sensing fluid, n_c.

For reference, Fig. 2(a) plots the mode power attenuation (MPA = $(20/1000)\alpha_s(a)\log_{10}e$ [dB/mm]) and effective index (n_{eff}) of the LRSPP propagating along the sensing section filled with a sensing solution index-matched to CYTOP (n_c = 1.3348), as a function of metal stripe thickness t, with and without an adlayer of thickness a = 10 nm. Fig. 2(b) plots the total coupling loss $2C_{dB}$ ($C_{dB}(a) = -20\log_{10}|C(a)|$ [dB]) at the input and output of the sensing channel. The distribution of the main transverse electric field component of the LRSPP (E_y) over the waveguide cross-section is shown as the insets to Fig. 2(b). It is apparent from Fig. 2 that the adlayer perturbs all modal properties over a broad range of stripe thickness. In attenuation-based biosensing it is important to understand, in particular, the dependencies $C(a)$ and $\alpha_s(a)$.

The first and second terms in (1) remain constant during a sensing experiment. The last term is the transmittance of the sensing channel, $T_s(a)$:

$$T_s(a) = P_{out,s}(a) / P_{in,s} = |C(a)|^4 \exp(-2\alpha_s(a)L) \tag{2}$$

where $P_{in,s}$ and $P_{out,s}(a)$ are the power incident on, and emerging from, the sensing channel at reference planes just inside the input and output access waveguides (Fig. 1). The transmittance of the sensing section depends on a.

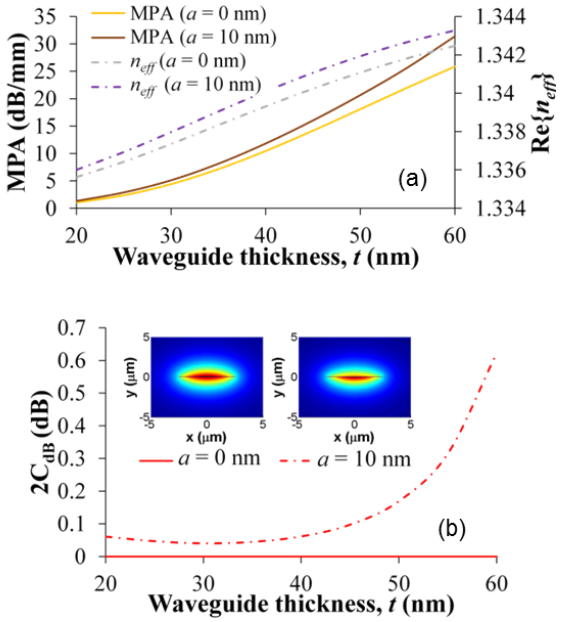

Fig. 2 (a) Mode power attenuation (MPA) and n_{eff} of the LRSPP propagating along the sensing channel filled with a sensing solution index-matched to CYTOP (n_c = 1.3348), as a function of metal stripe thickness t, with and without an adlayer of thickness a = 10 nm. (b) Total coupling loss $2C_{dB}$ at the input/output of the sensing channel and the access waveguides. The distribution of the main transverse electric field component of the LRSPP (E_y) over the waveguide cross-section is shown in inset.

The surface sensitivity of the sensor is obtained by taking the derivative of the measurand, $P_{out}(a)$, with respect to a:

$$\frac{\partial P_{out}(a)}{\partial a} = P_{inc} \cdot |C_i|^2 \exp(-2\alpha L_0) \cdot \frac{\partial T_s(a)}{\partial a} \tag{3}$$

where (1) and (2) were used. From the above, we note that to increase the sensitivity we should

increase the incident power, P_{inc}, maximise the overlap factor at the sensor input ($|C_i| \sim 1$), and minimise the loss of the input and output access waveguides, say, by choosing their length ($L_0/2$) as short as is practically possible. Making $|C_i| \sim 1$ is particularly important because any uncoupled light propagates essentially in the forward direction and contributes noise at the power sensor. We also note that we should seek to maximise the sensitivity of the sensing channel, $|\partial T_s(a)/\partial a|$; we have introduced the absolute value because the latter may be positive or negative.

The surface mass density (in g/m^2) that accumulates on the surface of the waveguide as binding occurs is related to the adlayer optical model via [24]:

$$\Gamma = \frac{a(n_a - n_c)}{\partial n / \partial c} \tag{4}$$

where $\partial n/\partial c$ is the change in RI with analyte concentration (usually $\partial n/\partial c \sim 0.185$ mm^3/mg).

The change in surface mass density $\Delta\Gamma$ is related to the change in adlayer thickness Δa via the above:

$$\Delta\Gamma = \frac{\Delta a(n_a - n_c)}{\partial n / \partial c} \tag{5}$$

Changes in output power ΔP_{out} are related to Δa through:

$$\Delta P_{out} = \frac{\partial P_{out}(a)}{\partial a}\Delta a \tag{6}$$

We obtain the detection limit as the smallest detectable change in surface mass density $\Delta\Gamma_{\min}$ by combining (5) and (6):

$$\Delta\Gamma_{\min} = \frac{(n_a - n_c)}{\partial n / \partial c}\frac{1}{\left|\partial P_{out}(a)/\partial a\right|}\Delta P_{out,\min} \tag{7}$$

where $\Delta P_{out,\min}$ is the smallest detectable change in output power which is related to the standard deviation of the baseline output power (often taken as a factor of the latter). The detection limit is observed to decrease as the surface sensitivity $|\partial P_{out}(a)/\partial a|$ increases and as the smallest detectable change in output power $\Delta P_{out,\min}$ decreases.

C. Surface sensitivity of the sensing channel

Based on (3), optimising the surface sensitivity of the sensing channel, $\partial T_s(a)/\partial a$, is key. Taking the derivative of (2) yields:

$$\frac{\partial T_s(a)}{\partial a} = 2\left|C(a)\right|^3 \exp(-2\alpha_s(a)L)\left(2\frac{\partial\left|C(a)\right|}{\partial a} - \left|C(a)\right|L\frac{\partial\alpha_s(a)}{\partial a}\right) \tag{8}$$

In previous work [18], we suggested two possible simplifying cases for (8). In the first case, the first term dominates:

$$2\left|\frac{\partial\left|C(a)\right|}{\partial a}\right| >> \left|C(a)\right|L\left|\frac{\partial\alpha_s(a)}{\partial a}\right| \tag{9}$$

so (8) simplifies to:

$$\frac{\partial T_s(a)}{\partial a} \cong 4\left|C(a)\right|^3\frac{\partial\left|C(a)\right|}{\partial a}\exp(-2\alpha_s(a)L) \tag{10}$$

where the coupling sensitivity $\partial|C(a)|/\partial a$ is the key factor determining the sensor performance.

In the second case, the second term dominates:

$$2\left|\frac{\partial|C(a)|}{\partial a}\right| << |C(a)|L\left|\frac{\partial\alpha_s(a)}{\partial a}\right| \tag{11}$$

so (8) simplifies to:

$$\frac{\partial T_s(a)}{\partial a} \cong -2|C(a)|^4 \frac{\partial\alpha_s(a)}{\partial a} L\exp(-2\alpha_s(a)L) \tag{12}$$

where the attenuation sensitivity $\partial\alpha_s(a)/\partial a$ and the sensing length L are the key factors determining sensor performance. The sensitivity of the stripe at initial adlayer growth is then given by setting $a = 0$ in (12):

$$\frac{\partial T_s(0)}{\partial a} \cong -2|C(0)|^4 \frac{\partial\alpha_s(0)}{\partial a} L\exp(-2\alpha_s(0)L) \tag{13}$$

Choosing $L=1/(2\alpha_s(0))$ maximises the product $L\exp(-2\alpha_s(0)L$) as is deduced by taking the derivative w.r.t L and setting it to zero (following [5]), so this length is taken as the optimal sensing length L_{opt}. Substituting this length into (13) yields for the channel sensitivity at $a = 0$:

$$\left.\frac{\partial T_s(0)}{\partial a}\right|_{L=L_{opt}} \cong -|C(0)|^4 \frac{1}{e}\frac{\partial\alpha_s(0)}{\partial a}\frac{1}{\alpha_s(0)} = -|C(0)|^4 \frac{1}{e}K \tag{14}$$

where:

$$K = \frac{\partial\alpha_s(0)}{\partial a}\frac{1}{\alpha_s(0)} \tag{15}$$

K is analogous to the parameter G that was defined in [5] for phase sensing. Maximising the surface sensitivity in this case (*i.e.*, where (11) holds) thus requires maximising $|K|$.

We now investigate the channel surface sensitivity numerically, by varying the thickness of the stripe t and the refractive index of the sensing fluid n_c, seeking regions where (8) must be used or where (10) or (12) can be used, along with optimal designs. Fig. 3 plots $\partial|C(0)|/\partial a$, $\partial\alpha_s(0)/\partial a$, and K as a function of t for three sensing fluid RIs.

The values of $\partial|C(0)|/\partial a$ and $\partial\alpha_s(0)/\partial a$ were approximated via second-order error $O(h^2)$ equidistant forward-difference formulae [25]:

$$\partial|C(a_i)|/\partial a = (-3|C(a_i)| + 4|C(a_{i+1})| - |C(a_{i+2})|/2h \tag{16}$$

$$\partial\alpha_s(a_i)/\partial a = (-3\alpha_s(a_i) + 4\alpha_s(a_{i+1}) - \alpha_s(a_{i+2})/2h \tag{17}$$

where $h = a_{i+1} - a_i$. In the computations of $\partial|C(0)|/\partial a$ and $\partial\alpha_s(0)/\partial a$, we set h = 1 nm and $a_i = 0$, and use the finite-element method to compute the modal properties of the LRSPP for each a_i in (16) and (17).

In order to assess the inequalities (9) and (11), we must assume order-of-magnitude values for $|C(a)|$ and L to be used therein. For this purpose we choose $|C(a)| \sim 1$ and $L \sim 2$ mm, which are typical values, and furthermore allow the inequalities to be assessed by comparing the left axes of Figs. 3(a)-(c) directly to the right axes.

For n_c = 1.3303 (Fig. 3(a)), we find that (11) is satisfied for $t \geq 35$ nm so (12) can be used. For t < 35 nm, both terms are significant so (8) must be used. Due to the signs of the partial derivatives $\partial|C(0)|/\partial a$ and $\partial\alpha_s(0)/\partial a$, the terms are additive and the surface sensitivity (8) is always positive. This result agrees with experimental observations where the output power increases during adlayer formation (Section III and [15]).

In the case of n_c = 1.3348 (Fig. 3(b)), we find that (11) is satisfied over the full range of Au thickness; (12) can thus be used throughout.

Similar trends as in n_c = 1.3303 are observed for n_c = 1.3393 (Fig. 3(c)) where (11) is satisfied for $t \geq 35$ nm, so (12) can be used. Both terms are comparable below this thickness, so (8) must be used. As $\partial|C(0)|/\partial a$ crosses over zero at $t \sim 40$ nm, its contribution to the sensor performance goes from subtractive to additive.

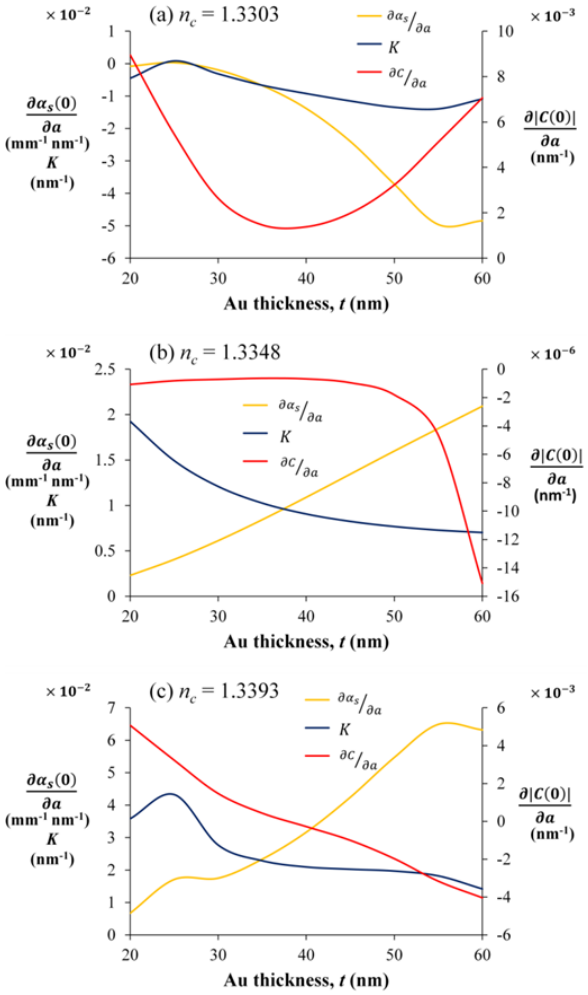

Fig. 3. $\partial|C(0)|/\partial a$, $\partial\alpha_s(0)/\partial a$, and K as a function of Au thickness for (a) n_c = 1.3303, (b) n_c = 1.3348, and (c) n_c = 1.3393.

We can deduce optimal designs for the biosensor based on the maximum value of $|K|$ while ensuring that the LRSPP remains well-guided throughout the structure (non-radiative with $|C(a)| \sim 1$). For n_c = 1.3303, maximum $|K|$ is observed at t = 55 nm. For n_c = 1.3348, $|K|$ increases with decreasing t, so a good Au thickness is taken as t = 20 nm (for practical reasons as a high-quality film thinner than 20 nm may be difficult to achieve). For n_c = 1.3393, maximum $|K|$ occurs at t = 25 nm.

D. Optimal Sensing Length L_{opt}

As discussed in the previous subsection (11) is satisfied and the attenuation sensitivity $\partial\alpha_s(a)/\partial a$ dominates the surface sensitivity for a wide range of Au thickness. Thus, (12) often holds, and the optimal sensing length $L_{opt} = 1/(2\alpha_s(0)$ should generally be selected. Fig. 4 plots L_{opt} as a function of Au thickness for three waveguide widths (w = 4, 5 and 6 μm) and three RI of the sensing fluid (n_c = 1.3303, 1.3348 and 1.3393). For all n_c, the sensing length decreases rapidly with increasing stripe thickness. Also, the waveguide width and sensing RI have significant effects on L_{opt} for t < 30 nm, but as t increases, L_{opt} tends to ~ 1 mm for $t \sim 30$ nm in all cases. Thicknesses of

25 to 30 nm do not induce too much propagation loss (Fig. 2(a)), yet remain suitable for miniaturized biosensors. However, the sensing length must remain long enough to allow radiative modes, if induced by uncoupled light at the input of the sensing waveguide, to spread. L_{opt} for n_c = 1.3348 is always greater than for the other sensing RI as the attenuation is lowest when the sensing RI is matched to that of CYTOP.

Table I summarizes the performance of some designs for n_c = 1.3303, 1.3348 and 1.3393 using n_a = 1.5, $\partial n/\partial c$ = 0.185 mm^3/mg, w = 5 µm and L_0 = 1 mm (selected to allow length for handling and interfacing with external fluidics). The incident power and the minimum detectable power were taken as P_{inc} = 12 mW and $\Delta P_{out,\min}$ = 6.2 nW following typical values observed in experiments ([15] and Section III). The thickness of the Au stripe was selected in each case to maximise $|K|$ as determined in the previous section, and the corresponding L_{opt} was taken as the length of the sensing channel ($L = L_{opt}$). $\partial P_{out}(a)/\partial a$, $\partial T_s(a)/\partial a$ and $\Delta\Gamma_{\min}$ were computed using (3), (8) and (7).

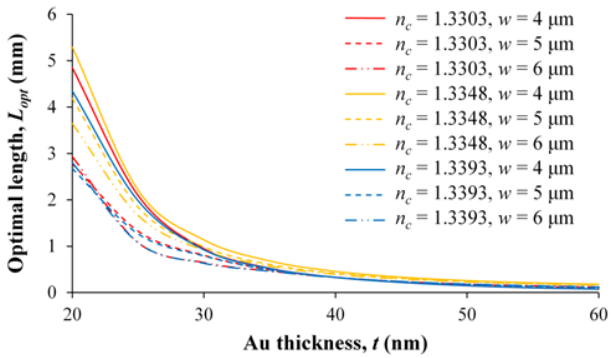

Fig. 4. Optimal sensing length as a function of Au stripe thickness for various stripe widths and RI of the sensing fluid.

TABLE I
SUMMARY OF DESIGNS AT n_c = 1.3303, 1.3348 AND 1.3393

n_c	1.3303	1.3348	1.3393
t (nm)	55	20	25
C_i	0.8179	0.9717	0.9604
α (mm^{-1})	2.5370	0.1195	0.2714
$C(0)$	0.9448	1.0000	0.9344
$\alpha_s(0)$ (mm^{-1})	3.5584	0.1195	0.3949
L_{opt} (mm)	0.1405	4.1858	1.2661
$\partial\lvert C(0)\rvert/\partial a$ (nm^{-1})	5.119×10^{-3}	-1.0748×10^{-6}	3.2352×10^{-3}
$\partial\alpha_s(0)/\partial a$ (mm^{-1}·nm^{-1})	-4.9634×10^{-2}	2.3011×10^{-3}	1.7088×10^{-2}
$\lvert\partial T_s(a)/\partial a\rvert$ (nm^{-1})	1.0441×10^{-2}	7.0884×10^{-3}	8.2497×10^{-3}
$\lvert\partial P_{out}(a)/\partial a\rvert$ (µW nm^{-1})	0.5245	63.2518	53.0677
$\Delta\Gamma_{\min}$ (pg·mm^{-2})	10.8438	0.0875	0.1015

It is observed from Table I that the design for t = 55 nm at n_c = 1.3303 has the highest channel surface sensitivity $|\partial T_s(a)/\partial a|$ but the lowest power sensitivity $|\partial P_{out}(a)/\partial a|$ and thus the worst detection limit ($\Delta\Gamma_{\min}$); this is due to attenuation along the access lines, on either side of the sensing channel, which must be fixed to some practical minimum length (e.g., L_0 = 1 mm, see (3)). The other designs in Table I produce very compelling detection limits of about $\Delta\Gamma_{\min}$ = 0.1 pg/mm^2.

E. Linear model for sensing channel transmittance

In an attenuation-based biosensing experiment, we are interested in monitoring the output power before, during and after the formation of an adlayer, and relating the change to the adlayer thickness. A simple linear model for the transmittance of the sensing channel would be convenient.

A typical binding response of a biomaterial sample (*e.g.* protein) is illustrated in Fig. 5. Depending on the RI of the sensing fluid, the output power $P_{out}(a)$ can either increase or decrease during adlayer formation (note the sign of the sensitivities plotted in Fig. 3). If n_c is lower than the RI of CYTOP (n_c < 1.3348), the formation of a high-index adlayer causes the field distribution of the waveguide to become increasingly symmetric which increases the sensing channel transmittance and the output power. The opposite situation applies for $n_c \geq$ 1.3348, where the field distribution becomes increasingly asymmetric during adlayer formation, decreasing the channel transmittance and output power.

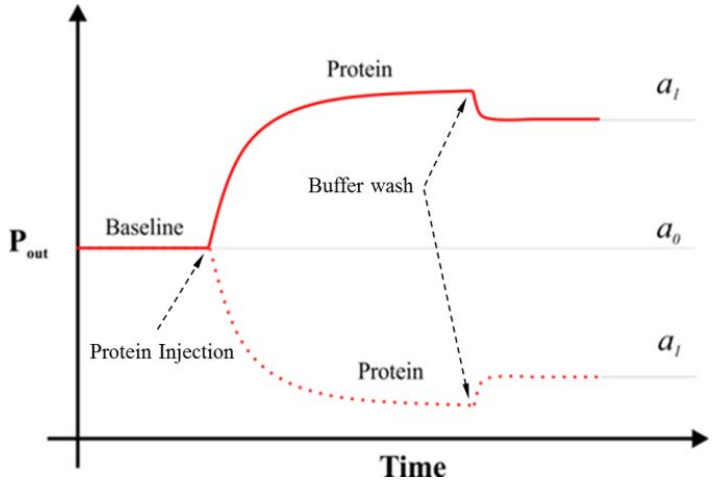

Fig. 5. Schematic showing a typical binding response (output power *vs*. time) for protein adsorption where a_0 is a nominal thickness prior to adlayer growth (representing say immobilised receptor chemistries) and a_1 is the thickness after adlayer formation. A step-in-signal at the washing point may arise either due to a bulk step in refractive index and/or protein dissociation.

The sensing channel transmittance $T_s(a)$ depends weakly on a over a small range of a in biochemical sensing [15]. We can approximate the exponential in (2) as the first two terms of its Taylor series expansion and represent $T_s(a)$ as a linear model:

$$T_s(a) = \left|C(a)\right|^4 \exp(-2\alpha_s(a)L) \cong ma + b \tag{18}$$

The output power before and after adlayer formation (Fig. 5) can then be written by substituting the linear model for $T_s(a)$ in (1) as:

$$P_{out}(a_0) = k_1(ma_0 + b) \qquad \text{and} \qquad P_{out}(a_1) = k_1(ma_1 + b) \tag{19}$$

where we have defined $k_1 = P_{inc}|C_i|^2\exp(-2\alpha L_0)$. k_1 remains constant during a sensing experiment.

The normalised change in output power due to adlayer formation is then written:

$$\frac{P_{out}(a_1) - P_{out}(a_0)}{P_{out}(a_0)} = \frac{m(a_1 - a_0)}{ma_0 + b} \tag{20}$$

If we set $\Delta a = a_1 - a_0$ and $k_2 = m/(ma_0+b)$, then (20) becomes:

$$\frac{P_{out}(a_1) - P_{out}(a_0)}{P_{out}(a_0)} = \frac{m \cdot \Delta a}{ma_0 + b} = k_2 \Delta a \tag{21}$$

The thickness of the adlayer formed Δa is obtained from the output powers $P_{out}(a_0)$ and $P_{out}(a_1)$ by rearranging (21):

$$\Delta a = \frac{1}{k_2}\left(\frac{P_{out}(a_1)}{P_{out}(a_0)} - 1\right) \tag{22}$$

Using (5) to substitute for Δa in (22) yields the relationship between the change in surface mass density to the measured output powers before and after adlayer formation:

$$\Delta\Gamma = \frac{1}{k_2}\frac{(n_a - n_c)}{\partial n/\partial c}\left(\frac{P_{out}(a_1)}{P_{out}(a_0)} - 1\right) \tag{23}$$

Regardless of the sign of the change in output power, the change in adlayer thickness and surface mass density obtained from (22) and (23) are always positive for adlayer growth (because k_2 and m are correspondingly positive or negative).

The sensing channel transmittance $T_s(a)$ computed using (2) with $L = L_{opt}$ is plotted in Fig. 6 as a function of the adlayer thickness a for w = 5 μm, several stripe thicknesses t, and different indices of sensing fluid, n_c. We also plot the linear model of $T_s(a)$ as the dotted curve for the case of t that maximises $|K|$ and give its equation in inset. As argued above, the sensing channel transmittance is well-represented by the linear model of (18), as evidenced by the very good R^2 values obtained for each. Fig. 6 also illustrates the importance of carefully controlling the waveguide thickness during fabrication because an error of ±5 nm will significantly affect the performance of the biosensor.

As discussed previously, the waveguide becomes more symmetric as the adlayer grows for n_c = 1.3303 (Fig. 6(a), sensing fluid RI below CYTOP), causing the transmittance to increase as observed. The trend of the curves for the case n_c = 1.3348 (Fig. 6(b), sensing fluid RI matched to CYTOP) are opposite those of Fig. 6(a) because the waveguide is in symmetry in the absence of an adlayer (a = 0), and during adlayer growth, the waveguide becomes asymmetric, reducing its transmittance. The same qualitative behaviour is observed for n_c = 1.3393 (Fig. 6(c), sensing fluid RI above CYTOP).

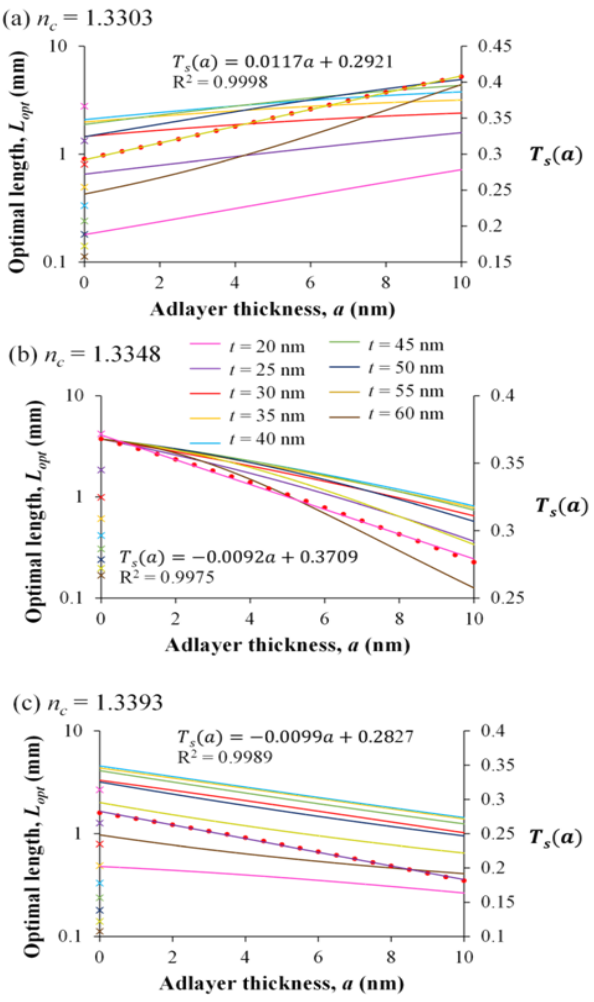

Fig. 6. Optimal sensing length L_{opt} (marked as ×) and channel transmittance $T_s(a)$ (solid lines) as a function of the adlayer thickness a for different Au thicknesses t and sensing fluids of RI (a) n_c = 1.3303, (b) n_c = 1.3348 and (c) n_c = 1.3393. the linear fit for $T_s(a)$ is plotted as the red dotted line in each case, for the Au thickness that maximises $|K|$ ((a) t = 55 nm, (b) t = 20 nm, (c) t = 25 nm); the equation of the linear model and R^2 goodness of fit are given in inset.

III. Experimental

A. Chemicals

2-Isopropanol semiconductor grade (IPA), acetone HPLC grade ≥ 99.9%, glycerol (electrophoresis grade), Bovine Serum Albumin (BSA), heptane and Phosphate buffer saline (PBS) 0.01 M, pH 7.4 were obtained from Sigma-Aldrich. PBS solution was prepared from the package by dissolving containing salts in 1 L of deionized water. Distilled water was deionized using Millipore filtering membranes (Millipore, Milli-Q water system at 16 MΩ·cm).

B. Experimental procedures

A detailed description of the sensor and the experimental setup can be found in [15]. Cleaning procedures and assembly can be found in [26]. The waveguide used in all the experiments (Fig. 7) had the following parameters: w = 5 μm, t = 35 nm (as measured by AFM), L = 1.65 mm etched length and 3.2 mm total length including the access waveguides (L_0 = 1.55 mm).

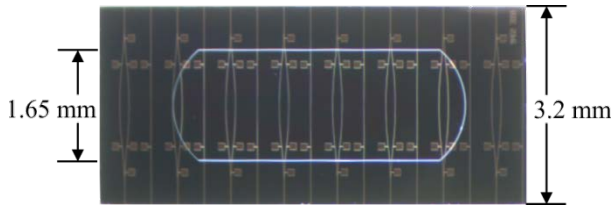

Fig. 7. Microscope image of a sensor with straight waveguides of the following parameters: w = 5 μm, t = 35 nm, L = 1.65 mm etched length and 3.2 mm total length. MZIs are also present but not used in the experiments.

Throughout the experiments, the sensing buffer was phosphate buffered saline (PBS, pH 7.4 - biologically compatible) mixed with glycerol (Gly) to vary n_c.

The CYTOP RI varies very slightly from wafer to wafer because during sensor fabrication the solvent evaporation rate is not very well controlled and the distribution of the CYTOP monomers is Gaussian. To estimate the actual RI of CYTOP, a simple bulk sensing experiment with various RI solutions was carried out, following [15], and the buffer RI that produced highest output power was taken as having the RI of CYTOP. For the sensor used here the RI of CYTOP was found to be 1.3355 as determined in this manner.

In order to estimate the effect of the input power on the noise measured at the output power meter, a PBS/Gly solution matching the RI of CYTOP (n_c = 1.3355) was injected into the fluidic cell with a freshly cleaned sensor installed. The experiment was performed under static conditions (no flow) by varying the input power.

To determine the effect of n_c on the sensor response, the RI of the PBS/Gly solution was varied, while keeping the BSA concentration constant at ~100 μg/ml. Five experiments were performed on the same waveguide using the following PBS/Gly RIs: n_c = 1.3306, 1.3355 (CYTOP matching), 1.3369, 1.3400 and 1.3440. At the beginning of each experiment a baseline was established for ~5 minutes with PBS/Gly under flow to ensure stability and to estimate the noise. After each experiment, the sensor was cleaned with plenty of sodium dodecyl sulphate (SDS) and DDI H_2O, then by cleaning in a UV/Ozone chamber for 30 minutes. BSA experiments were performed under flow (20 μL/min) at λ_0 = 1315.89 nm, with the incident power set to P_{inc} = 10.7 dBm. All solutions were filtered through Millex-GP filters (PES membrane 0.22 μm).

C. Results and discussion

1) System Noise Characterization

A cleaned sensor with a bare Au stripe was installed into the setup with PBS/Gly buffer index-matched to CYTOP (n_c = 1.3355). The input fiber was aligned to the waveguide in order to produce maximum output power, the incident power was varied by varying the laser current, and the output power was recorded, as plotted in Fig. 8, after drift-free stability was observed. The range over which the input power varied was chosen to include our operating power for biosensing experiments (10.73 dBm, level 1) and an input power that produces a barely detectable output power level (-23.42 dBm, level 8). Selected portions of the stable region of levels 1, 5 and 7 of the response are presented as insets.

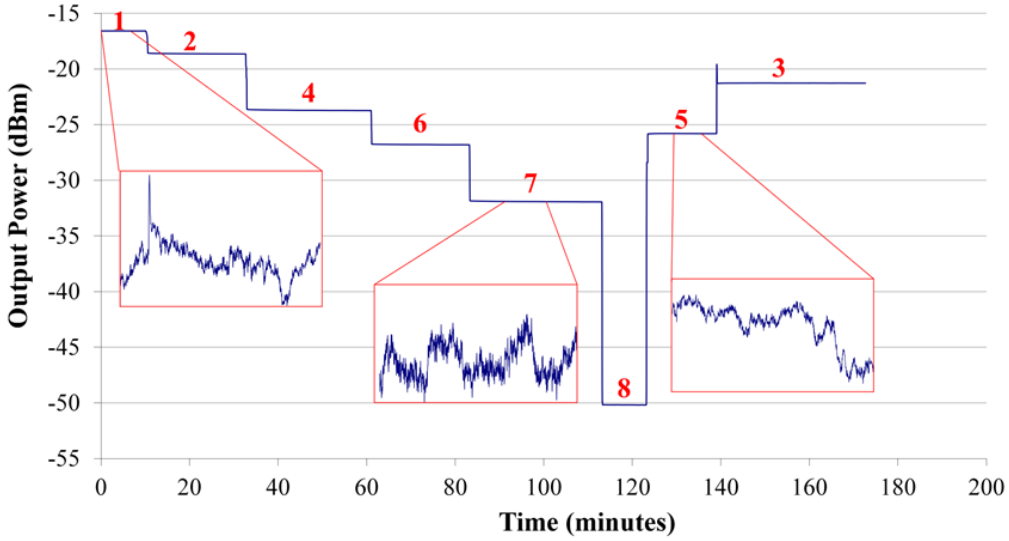

Fig. 8. Power output versus time as the incident power P_{inc} was varied: (1) 10.730 dBm (11.8 mW); (2) 8.796 dBm (7.6 mW); (3) 6.5 dBm (4.5 mW); (4) 3.74 dBm (2.36 mW); (5) 2.14 dBm (1.63 mW); (6) 0.709 dBm (1.18 mW); (7) -3.98 dBm (0.40 mW); (8) -23.42 dBm (4.55 μW). Conditions: λ_0 = 1315.89 nm, n_c = 1.3355 (PBS/Gly, CYTOP matching), no flow. The vertical full scale of all insets was set to 0.005 dBm.

The standard deviation σ and signal-to-noise ratio (SNR) measured at each level are plotted in Fig. 9. Considering the threshold for the diode laser (10 mA), level 7 was on the edge (9.8 mA) and level 8 (5 mA) was below threshold, so level 8 was removed from the plot. The standard deviation as a function of input power shows a general increasing trend, however it lacks any specific pattern. The SNR shows neither trend nor pattern. Both the standard deviation and SNR results suggest that the noise level is independent of the input power, implying that it does not originate with the optoelectronics. Other possible sources of noise are mechanical and thermal. Nonetheless, noise levels of a few nW and SNR's of several thousand are achievable.

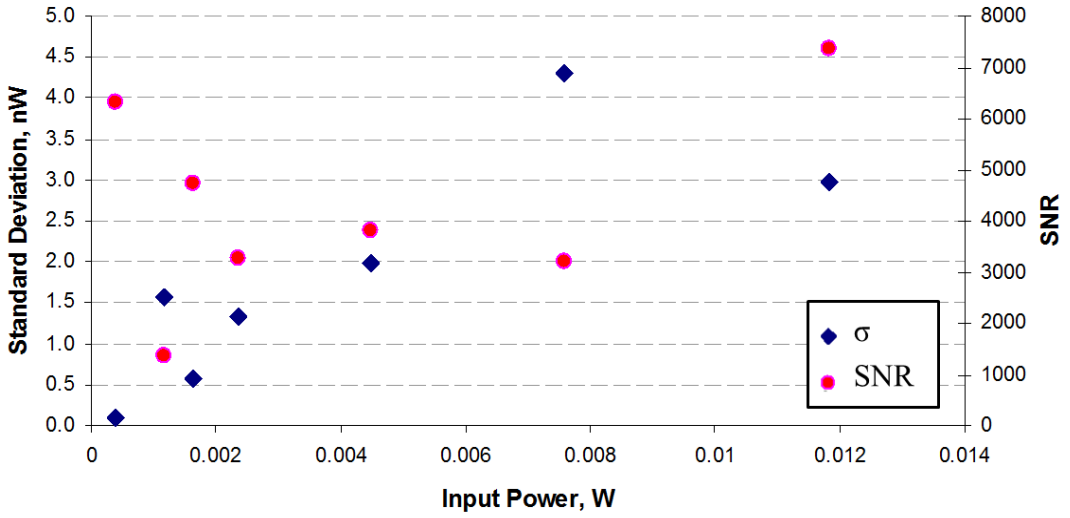

Fig. 9. Scatter plot of the standard deviation (σ) and the signal-to-noise ratio (SNR) as the input power was varied. The standard deviation and corresponding SNR were calculated using the most stable (drift free) portion of the response of Fig. 8 at each level. The SNR was computed by taking a ratio of the average response to the standard deviation of the same response.

2) Effect of n_c on the surface sensitivity

Fig. 10 demonstrates the response of the same waveguide exposed to BSA in different PBS/Gly solutions of different n_c. The waveguides were cleaned after every experiment following the procedure outlined under sub-section III.B. The output power (W) was normalized to the corresponding baseline for each case by taking a ratio of the each data point of the response to the first data point. The trend of the responses agrees qualitatively with the sketch of Fig. 5 and the results of Fig. 6. The transmittance increases during adlayer formation for a sensing fluid RI below that of CYTOP and decreases for a sensing fluid RI matched to or above CYTOP.

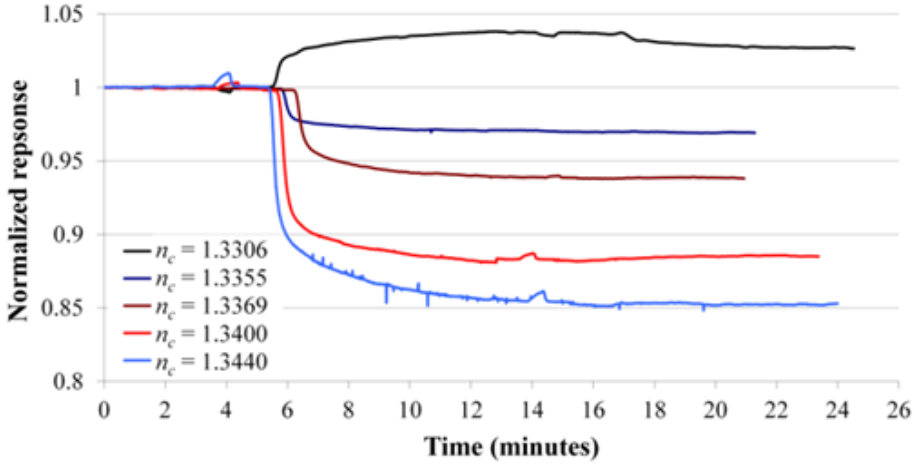

Fig. 10. Normalized response of a straight waveguide when 100 µg/ml of BSA in PBS/Gly with different refractive indices n_c is introduced.

The power change due to adlayer formation can be translated to a change in surface mass density using (23). The value of k_2 which varies with the sensing index n_c was computed theoretically. The computation was carried out by considering the actual dimension of the sensor used (verified through AFM measurements) and the actual wavelength of the laser diode supplied by the manufacturer λ_0 = 1315.89 nm. The Au waveguide is of similar dimension (w = 5 μm, t = 35 nm) as described initially except for the pedestal height of 435 nm. k_2 was computed using (21) with $a_0 = 0$ as $k_2 = m/b$ and used for the calculation of the surface mass density plotted in Fig. 11. The values of m and b were obtained through a linear fit of the sensing transmittance $T_s(a)$ over $0 \le a \le 10$ nm ((18), as discussed in subsection II.*E*). The values of m, b and k_2 obtained for each sensing index are summarized in Table II.

TABLE II
SUMMARY OF m, b AND k_2 FOR DIFFERENT SENSING INDEX n_c

n_c	m (nm^{-1})	b	k_2 (nm^{-1})
1.3306	0.0009	0.0363	0.0248
1.3355	−0.0025	0.0679	−0.0368
1.3369	−0.0028	0.0584	−0.0479
1.3400	−0.0017	0.0269	−0.0633
1.3440	−0.0005	0.0081	−0.0617

Ideally, the surface mass density should be identical if a BSA monolayer of the same thickness is formed on the sensor surface in every experiment. However, the results in Fig. 11 show a spread. The spread can be explained as random BSA physisorption. A BSA molecule has a cigar-like shape and was shown previously to adsorb onto Au randomly in a mixture of horizontal and vertical orientations [27, 28]. Thus, different packing of BSA on the surface is expected, resulting in different surface mass density.

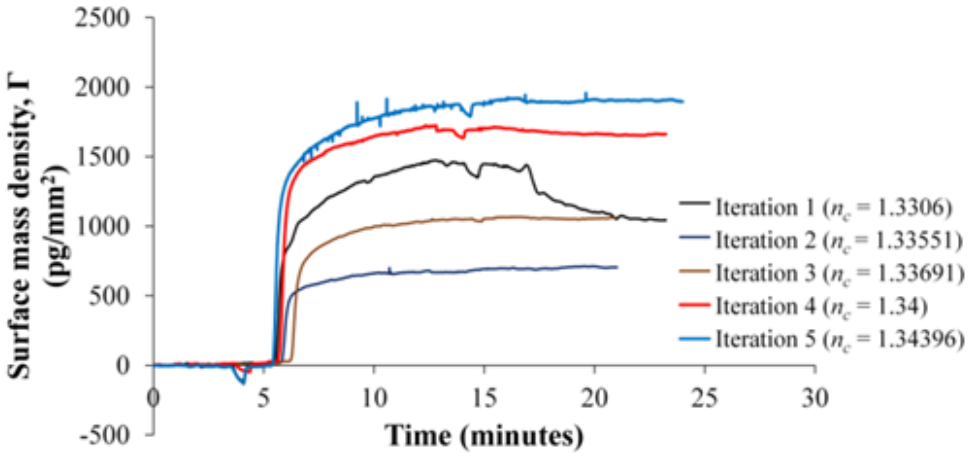

Fig. 11. Surface mass density *versus* time as 100 μg/ml of BSA in buffer is injected. The flowrate was set to 20 μl/min and P_{inc} = 10.7 dBm of optical power was incident on the sensor at λ_0 = 1315.89 nm.

To determine the average effective optical thickness of adlayer formed from the BSA experiments, the experimental results were compared to theory in Fig. 12. The change in insertion loss ΔIL (dB) due to adlayer formation is:

$$\Delta IL(a) = IL_s(a) - IL_s(0) \tag{24}$$

From (2), the insertion loss of the sensing channel $IL_s(a)$ is:

$$IL_s(a) = 2C_{dB}(a) + L \cdot MPA(a) \tag{25}$$

Three adlayer thicknesses (a = 1, 1.5 and 2 nm), which produce ΔIL comparable with the experimental results were considered. The least squares method was used to determine the best fit adlayer thickness formed during the BSA experiments. The sum of squared residuals is computed as:

$$S = \sum_{i=1}^{5} (T_{n_{c,i}} - E_{n_{c,i}})^2 \tag{26}$$

where $n_{c,i}$ = {1.3306, 1.3355, 1.3369, 1.3400, 1.3440}, $T_{nc,i}$ is the theoretical ΔIL at a specific sensing index and $E_{nc,i}$ is the experimental ΔIL at the same sensing index. The best fit adlayer thickness is found to be a = 1.5 nm.

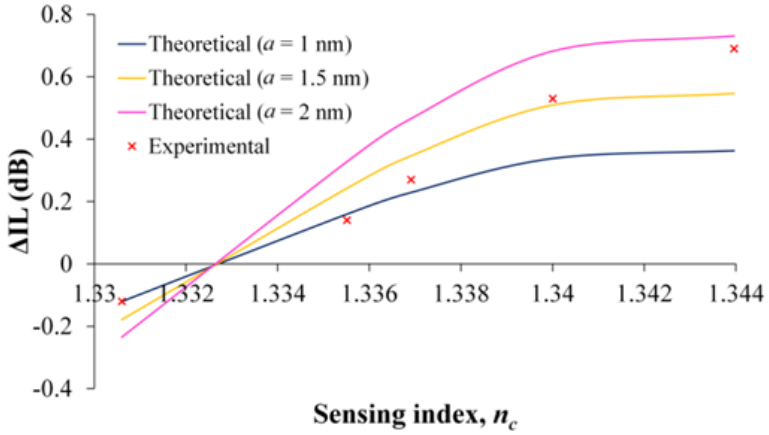

Fig. 12. A change in insertion produced by BSA adsorption on Au waveguide as a function of refractive index of the background buffer.

The accumulated BSA surface mass density (ΔΓ), the noise observed over a 10 minute baseline interval (σ), the SNR (ΔS/σ), and the detection limit ($\Delta\Gamma_{min}$) are summarised in Table III for all of the experiments. The detection limit was taken at the limit of the SNR (SNR = 1, $\Delta P_{out,min} = \sigma$). $\Delta\Gamma_{min}$ is found to be 4.1 pg/mm^2 in the best case of n_c = 1.3355 (CYTOP matching). If the minimum observed σ of 3.1 nW were achieved in all cases, a lower $\Delta\Gamma_{min}$ of 1.7 pg/mm^2 would be observed. If a margin were used to ensure reliable detection (*e.g.*, $\Delta P_{out,min} = 2\sigma$ for SNR = 2) then the detection limit would increase correspondingly.

TABLE III
DETECTION RESULTS AND DETECTION LIMIT $\Delta\Gamma_{min}$ FOR $\Delta S/\sigma = 1$

n_c	ΔΓ (pg/mm^2)	σ (nW)	ΔS/σ	$\Delta\Gamma_{min}$ (pg/mm^2)
1.3306	1000.31	3.1	172	5.8
1.3355	762.29	6.4	185	4.1
1.3369	1184.22	9.9	220	5.4
1.3400	1662.30	6.6	360	4.6
1.3440	2181.14	3.2	467	4.7

IV. Conclusion

The surface sensitivity of straight LRSPP waveguides was investigated by considering sensing fluids of refractive index slightly below, equal to, and slightly above that of CYTOP, the material used as the claddings. The attenuation sensitivity was found to dominate over a wide range of Au thicknesses, so good designs for the sensing waveguide in terms of Au stripe thickness and length can be determined. We demonstrated that optimizing the sensor performance involves maximizing $|K|$ where $K = (\partial\alpha_s/\partial a)/\alpha_s$ and selecting the optimal sensing length as $L_{opt} = 1/(2\alpha_s)$. Optimal designs were predicted to produce very compelling detection limits of $\Delta\Gamma_{min} < 0.1$ pg/mm^2. We proposed a linear model for the sensitivity of the sensing channel and demonstrated its

applicability over a wide range of designs. Experiments involving BSA physisorption on bare Au waveguides were carried out using solutions of different refractive index and the observed trends were noted to agree very well with theory. We also showed that the noise observed during the experiments does not originate with the optoelectronics. Noise levels (σ) of a few nW and SNRs of several thousand were observed in static fluidic baseline experiments. The measured detection limit $\Delta\Gamma_{min}$ was found to be 4.1 pg/mm^2 (SNR = 1) although a lower estimate of $\Delta\Gamma_{min}$ = 1.7 pg/mm^2 can be practically achieved by ensuring a better stability.

REFERENCES

[1] M. A. Cooper, "Optical biosensors in drug discovery," *Nat. Rev. Drug Discov.,* vol. 1, pp. 515-528, 2002.

[2] J. Homola, "Surface plasmon resonance sensors for detection of chemical and biological species," *Chem. Rev.,* vol. 108, pp. 462-493, 2008.

[3] S. Löfås, "Optimizing the hit-to-lead process using SPR analysis," *Assay Drug Dev. Technol.,* vol. 2, pp. 407-416, 2004.

[4] P. Berini, "Long-range surface plasmon polaritons," *Adv. Opt. Photonics,* vol. 1, pp. 484-588, 2009.

[5] P. Berini, "Bulk and surface sensitivities of surface plasmon waveguides," *New J. Phys.,* vol. 10, p. 105010, 2008.

[6] V. Chabot, Y. Miron, M. Grandbois, and P. G. Charette, "Long range surface plasmon resonance for increased sensitivity in living cell biosensing through greater probing depth," *Sens. Actuators, B,* vol. 174, pp. 94-101, 2012.

[7] R. Slavík and J. Homola, "Ultrahigh resolution long range surface plasmon-based sensor," *Sens. Actuators, B,* vol. 123, pp. 10-12, 2007.

[8] M. Vala, S. Etheridge, J. Roach, and J. Homola, "Long-range surface plasmons for sensitive detection of bacterial analytes," *Sens. Actuators, B,* vol. 139, pp. 59-63, 2009.

[9] Y. H. Joo, S. H. Song, and R. Magnusson, "Demonstration of long-range surface plasmon-polariton waveguide sensors with asymmetric double-electrode structures," *Appl. Phys. Lett.,* vol. 97, p. 201105, 2010.

[10] A. W. Wark, H. J. Lee, and R. M. Corn, "Long-range surface plasmon resonance imaging for bioaffinity sensors," *Anal. Chem.,* vol. 77, pp. 3904-3907, 2005.

[11] R. Heideman and P. Lambeck, "Remote opto-chemical sensing with extreme sensitivity: design, fabrication and performance of a pigtailed integrated optical phase-modulated Mach–Zehnder interferometer system," *Sens. Actuators, B,* vol. 61, pp. 100-127, 1999.

[12] B. Shew, Y. Cheng, and Y. Tsai, "Monolithic SU-8 micro-interferometer for biochemical detections," *Sens. Actuators, A,* vol. 141, pp. 299-306, 2008.

[13] D. Xu, A. Densmore, A. Delâge, P. Waldron, R. McKinnon, S. Janz*, et al.*, "Folded cavity SOI microring sensors for high sensitivity and real time measurement of biomolecular binding," *Opt. Express,* vol. 16, pp. 15137-15148, 2008.

[14] J. C. Love, L. A. Estroff, J. K. Kriebel, R. G. Nuzzo, and G. M. Whitesides, "Self-assembled monolayers of thiolates on metals as a form of nanotechnology," *Chem. Rev.,* vol. 105, pp. 1103-1170, 2005.

[15] O. Krupin, H. Asiri, C. Wang, R. N. Tait, and P. Berini, "Biosensing using straight long-range surface plasmon waveguides," *Opt. Express,* vol. 21, pp. 698-709, 2013.

[16] O. Krupin, C. Wang, and P. Berini, "Selective capture of human red blood cells based on blood group using long-range surface plasmon waveguides," *Biosens. Bioelectron.,* vol. 53, pp. 117-122, 2014.

[17] W. R. Wong, O. Krupin, S. D. Sekaran, F. R. Mahamd Adikan, and P. Berini, "Serological diagnosis of dengue infection in blood plasma using long-range surface plasmon waveguides," *Anal. Chem.,* vol. 86, p. 1735−1743, 2014.

[18] W. R. Wong, F. R. M. Adikan, and P. Berini, "Surface sensitivity of straight long-range surface plasmon waveguides for attenuation-based biosensing," *Appl. Phys. A,* vol. 117, pp. 527-535, 2014

[19] A. Boltasseva, T. Nikolajsen, K. Leosson, K. Kjaer, M. S. Larsen, and S. I. Bozhevolnyi, "Integrated optical components utilizing long-range surface plasmon polaritons," *J. Lightw. Technol.,* vol. 23, pp. 413-422, 2005.

[20] R. Charbonneau, C. Scales, I. Breukelaar, S. Fafard, N. Lahoud, G. Mattiussi*, et al.*, "Passive integrated optics elements based on long-range surface plasmon polaritons," *J. Lightw. Technol.,* vol. 24, p. 477, 2006.

[21] A. Khan, O. Krupin, E. Lisicka-Skrzek, and P. Berini, "Mach-Zehnder refractometric sensor using long-range surface plasmon waveguides," *Appl. Phys. Lett.,* vol. 103, p. 111108, 2013.

[22] Asahi Glass Company. Cytop Technical Brochure Available: http://www.agc.com

[23] E. D. Palik, *Handbook of optical constants of solids* vol. 3: Academic press, 1998.

[24] J. A. De Feijter, J. Benjamins, and F. A. Veer, "Ellipsometry as a tool to study the adsorption behavior of synthetic and biopolymers at the air–water interface," *Biopolymers,* vol. 17, pp. 1759-1772, 1978.

[25] C. F. Gerald and P. O. Wheatley, *Applied Numerical Analysis*, 5th ed. Reading, MA: Addison-Wesley Publishing Company, 1994.

[26] O. Krupin, C. Wang, and P. Berini, "Strategies for leukemic biomarker detection using long-range surface plasmon-polaritons," in *Photonics North 2014*, 2014, pp. 92880W-92880W-11.

[27] R. Charbonneau, M. Tencer, N. Lahoud, and P. Berini, "Demonstration of surface sensing using long-range surface plasmon waveguides on silica," *Sens. Actuators, B,* vol. 134, pp. 455-461, 2008.

[28] M. Tencer, R. Charbonneau, N. Lahoud, and P. Berini, "AFM study of BSA adlayers on Au stripes," *Appl. Surf. Sci.,* vol. 253, pp. 9209-9214, 2007.

Chapter 6

Conclusions

Optical biosensors can provide a quick and cheap solution to many problems for the detection and interaction of biological matter. This thesis explored the capabilities of LRSPP SWG sensors for biosensing applications. The objective of the thesis was to present a novel potential optical sensor for the biosensing field. Experimental work presented here demonstrated the ability of the sensor to selectively detect large and small biological entities such as cells and proteins.

6.1. Summary and contributions

In the past decade LRSPPs have been theoretically studied for various applications including biosensing. However, very little investigation has been done in terms of experimental work to test LRSPP waveguides for detection of biological matter. Chapter 2 presented general experiments to demonstrate the capability of LRSPP SWG to detect changes in refractive index in bulk, as well as detect large objects (cells) and small objects (proteins). Bulk sensing was performed by injecting six solutions of different refractive indices in 2×10^{-3} RIU increments. The LOD was found to be 2.3×10^{-6} RIU and is comparable to that of conventional SPR instruments. Demonstration of RBC sensing was performed on anti-A functionalized surface by injecting O-RBCs following A-RBCs. Unrecoverable baseline after A-RBC injection suggested the reaction was specific to A-antigen and that generally cells can be detected. Protein sensing was performed by flowing BSA over two surfaces: carboxyl-terminated and PEG-terminated that respectively promotes and inhibits protein adsorption. The signal-to-noise ratio for a carboxyl-terminated surface was ~300 and that for a PEG-terminated surface was ~45 which suggests not only the capability of LRSPP SWGs to sense proteins, but also supports the validity of the proposed surface functionalization strategy using alkanethiols. In addition, using the data from BSA experiments, a limit of detection of the sensor in terms of mass per area was computed to be 12 pg/mm^2.

Preliminary experiments with human red blood cells in Chapter 2 motivated further investigation. Thus, Chapter 3 presented a deeper study of cell sensing. Employing the same strategy of anti-A and A-RBC interaction, the set of red blood cell samples was broadened to demonstrate the selectivity of an anti-A-functionalized surface to detect cells with A-antigen (groups A and AB), where cells lacking the latter served as a negative control (groups O and B). The LOD for RBC sensing in clear buffer was found to be less than 3×10^5 cells/ml, which was lower than that reported by using an SPR system in the late 1990s. Further experiments suggested that singe cell detection is possible with a signal-to-noise ratio of ~95 per cell. From a practical point of view, this study can be specifically of interest for detection of rare circulating tumor cells in cases of aggressive cancers when tumor cells leach into the blood stream. In addition, regeneration of the surface down to the antibody level up to 10 times was also demonstrated.

The ability to functionalize the Au surface with proper antibodies along with the capability of the LRSPP waveguides to be sensitive enough to detect proteins encouraged the pursuit of actual real-life detection problems of detecting B-cell leukemia markers. Thus, Chapter 4 presented the experimental study on the detection of relative abundance of immunoglobulin kappa and lambda light chains in patient sera, where an abnormal ratio of the latter is indicative of various blood tumors. The work was performed with the collaboration of Dr. Chen Wang from Mount Sinai Hospital, Toronto, who provided deeper insight into the problem along with the patient samples. Three patient sera were tested: normal serum (IgGκ-IgGλ ratio ~1.7), high kappa serum (IgGκ-IgGλ ratio ~12.7) and high lambda serum (IgGλ-IgGκ ratio ~7.0). The surface functionalization strategy to immobilize immunoglobulins was changed from carbodiimide coupling chemistry (Chapters 2 and 3) to Protein G affinity. One of the main rationales behind using Protein G was to create a surface that would be specific to only IgGs, thus performing an "immunological filtering" function to capture specifically immunoglobulins G out from the pool of serum proteins. Prior to testing patient sera, experiments with pure standard analytes were performed to validate the concept and determine reactivities and cross-reactivities of purchased immunoglobulins. Experimental optical responses were translated into mass load based on the sensitivity of straight waveguides (Eq 8.) to compute κ-λ ratios for the three samples. Two approaches were investigated where Protein G was

functionalized with either patient serum (reverse approach) or recognition antibodies (direct approach). Even though the results did not match exactly the ones provided by the Mount Sinai Hospital laboratory, for both approaches the sensor still demonstrated an ability to clearly differentiate between normal, high kappa and high lambda patient sera. Furthermore, for the high lambda patient serum the λ:κratio was higher than that provided (~9.5 *vs.* ~7) suggesting a possibility of the LRSPP SWG sensor to be more sensitive than the laboratory technique. In addition, three repeated runs were performed for each experiment that involved reverse approach, and demonstrated good reproducibility of the results. Experimental work in Chapter 4 increases the significance of the sensor by demonstrating its relevance for medical applications.

Chapter 5 addressed issues other than sensing which were directed towards investigation of improving waveguide performance. The theoretical part described modelling of the waveguide physical parameters and refractive index of the sensing buffer to optimize waveguide sensitivity for biosensing applications. Optimal designs were predicted to produce limits of detection <0.1 pg/mm^2. The experimental section consisted of two parts: investigation of the system noise and determination of waveguide sensitivity as a function of sensing buffer RI. The system noise was studied by varying the laser input power into the waveguide, exposed to the sensing buffer with CYTOP-matching refractive index. Data analysis suggested that the experimental noise does not originate from the optoelectronics but rather is mechanical or thermal in origin. Investigation of the sensitivity of the waveguide was carried out by adsorbing BSA in buffers of different refractive index on bare Au. The measured LOD was found to be 4.1 pg/mm^2, although a better value of 1.7 pg/mm^2 could be achieved by reducing the system noise.

6.2. Suggestions for future work

The specific detection of cells and proteins using LRSPP SWG sensor has been demonstrated, and the performance of such sensors investigated. However, no biomolecular kinetics have been extracted. Experiments involving Protein G and immunoglobulin reaction, such as presented in Chapter 4, by varying IgG concentrations could provide information on kinetics of this biomolecular interaction, and this information could be compared to that obtained via SPR studies.

The disadvantage of using bovine serum albumin to determine the experimental limit of detection for the sensor is that actual BSA adsorption packing on the waveguide is uneven and unpredictable due to its elliptic shape. This created significant uncertainties in our LOD estimates. It has been observed that EDC/NHS activation of carboxyl-terminated SAM can also be detected by the sensor. Thus, a more accurate prediction of detection limit can be performed by carrying out EDC/NHS activation of carboxyl-terminated SAM, when the hydrogen on carboxyl group is replaced by sulfo-NHS.

A number of structural changes of the sensor fluidic architecture have been discussed and implemented outside the scope of the thesis, but not actually tested for biosensing. Such that, employing individual fluidic channels for the waveguide could potentially lower the LOD for cell sensing.

From the practical point of view, a clinical study of the sensor performance could eventually attract the attention of medical community and help to promote the commercialization of the LRSPP SWG sensor.

Bibliography

[1] R. S. Marks, "Handbook of biosensors and biochips," *John Wiley & Sons*, **1**(1) (2007).

[2] C. R. Lowe and M. J. Goldfinch, "Novel electrochemical sensors for clinical analysis," *Biochemical Society Transactions*, **11**, 448–451 (1983).

[3] L. C. Clark and C. Lyons, "Electrode systems for continuous monitoring in cardiovascular surgery," *Annals of the New York Academy of Sciences*, **102**, 29–45 (1962).

[4] J. Wang, "Towards genoelectronics: electrochemical biosensing of DNA hybridization," *Chemistry—A European Journal*, **5**, 1681–1685 (1999).

[5] N. J. Mol and M. J. E. Fischer, "Surface plasmon resonance: methods and protocols," Humana Press (2010).

[6] D. R. Shankaran, V. Gobi, and N. Miura, "Recent advancements in surface plasmon resonance immunosensors for detection of small molecules of biomedical, food and environmental interest," *Sensors and Actuators B*, **121**, 158–177 (2007).

[7] Lofas, S., "Optimizing the hit-to-lead process using SPR Analysis," *Assay and Drug Development Technologies*, **2**(4), 407-415 (2004).

[8] R. Charbonneau, C. Scales, I. Breukelaar, S. Fafard, N. Lahoud, G. Mattiussi, and P. Berini, "Passive integrated optics elements based on long-range surface plasmon polaritons," *Journal of Lightwave Technology*, **24**(1), 477–494 (2006).

[9] A. Boltasseva, T. Nikolajsen, K. Leosson, K. Kjaer, M. S. Larsen, and S. I. Bozhevolnyi, "Integrated optical components utilizing long-range surface plasmon polaritons," *Journal of Lightwave Technology*, **23**(1), 413–422 (2005).

[10] P. Berini, "Bulk and surface sensitivities of surface plasmon waveguide," *New Journal of Physics*, **10**, 1-37 (2008).

[11] S. Takenobu, Y. Kuwana, Y. S. K. Takayama, M. Ono, H. Sato, N. Keil, W. Brinker, H. Yao, C. Zawadzki, Y. Morizawa, and N. Grote, "All-polymer 8x8 AWG wavelength router using ultra low loss polymer optical waveguide material (CYTOP^{TM})," *Optical Society of America*, **978-1-55752-855-1** (2007).

[12] C. Chiu, E. Lisicka-Skrzek, R. N. Tait, and P. Berini, "Fabrication of surface plasmon waveguides and devices in CYTOP with integrated microfluidic channels," *Journal of Vaccuum Science and Technology B*, **28**(4), 729–735 (2010).

[13] H. Asiri, "Fabrication of surface plasmon biosensors in CYTOP. Master's Thesis," *Department of Chemical and Biological Engineering, University of Ottawa*, Ottawa (2012).

[14] O. Krupin, H. Asiri, C. Wang, R. N. Tait, and P. Berini, "Biosensing using straight long-range surface plasmon waveguides," *Optics Express*, **21**, 698-709 (2013).

[15] O. Krupin, C. Wang, and P. Berini, "Strategies for leukemic biomarker detection using long-range surface plasmon-polaritons," *Photonics North-2014*: *proceedings of SPIE*, **9288,** Ottawa, Canada.

[16] A. D. Feijter, J. Benjamins, and F. A. Veer, "Ellipsometry as a tool to study the adsorption behavior of synthetic and biopolymers at the air-water interface," *Biopolymers*, **17**(7), 1759–1772 (1978).

[17] W.R. Wong, O. Krupin, F.R.M. Adikan, and P. Berini, "Optimization of long-range surface plasmon waveguides for attenuation-based biosensing," Accepted by *Journal of Lightwave Technology* on 04.03, 2015, (manuscript ID: JLT-17539-2015).

[18] R. S. Nezlin, "The immunoglobulins: structure and function," *San Diego Academic Press* (1998).

[19] A. Lehninger, M. Cox and D. L. Nelson, "Principles of biochemistry. 5th edition," *W. H. Freeman* (2008).

[20] J. C. Love, L.A. Estroff, R.G.N. Jennah, K. Kriebel, and G. M. Whitesides, "Self-assembled monolayers of thiolates on metals as a form of nanotechnology," *Chemical Reviews*, **105**(4), 1103-1169 (2005).

[21] K. Motesharei and D.C. Myles, "Molecular recognition on functionalized self-assembled monolayers of alkanethiols on gold," *Journal of The American Chemical Society*, **120**, 7328-7336 (1998).

[22] E. Ostuni, R. G. Chapman, R. E. Holmlin, S. Takayama, and G. M. Whitesides, "A survey of structure-property relationships of surfaces that resist the adsorption of protein," *Langmuir*, **17**, 5605-5620 (2001).

[23] D. Samanta and A. Sarkar, "Immobilization of bio-macromolecules on self-assembled monolayers: methods and sensor applications," *Chemical Society Reviews*, **40**, 2567–2592 (2011).

[24] T. G. Hermanson, "Bioconjugate Techniques. 2nd edition," *Academic Press* (2008).

[25] M. D. Boyle and K. J. Reis, "Bacterial Fc receptors," *Biotechnology*, **5**, 697–703 (1987).

[26] Y. M. Bae, B.-K. Oh, W. Lee, W. H. Lee, and J.-W. Choi, "Study on orientation of immunoglobulin G on protein G layer," *Biosensors and Bioelectronics*, **21**, 103–110 (2005).

[27] B. N. Johnson and R. Mutharasan, "pH effect on protein G orientation on gold surfaces and characterization of adsorption," *Langmuir*, **28**, 6928−6934 (2012).

[28] J. M. Fowler, M. C. Stuart, and D. K. Y. Wong, "Self-assembled layer of thiolated protein G as an immunosensor scaffold," *Analytical Chemistry*, **79**, 350-354 (2007).

[29] J. M. Lee, H. K. Park, Y. Jung, J. K. Kim, S. O. Jung, and B. H. Chung, "Direct immobilization of protein G variants with various numbers of cysteine residues on a gold surface," *Analytical Chemistry*, **79**, 2680-2687 (2007).

[30] R. W. Wood, "On a remarkable case of uneven distribution of light in a diffraction grating spectrum," *Physical Society of London*, **18**(1), 269-275 (1902).

[31] E. Kretschann and H. Raether, "Radiative decay of non-radiative surface plasmons excited by light," *Zeitschrift für Naturforschung A*, **23**, 2135 – 2136 (1968).

[32] A. Otto, "Excitation of surface plasma waves in silver by the method of frustrated total reflection," *Zeitschrift für Physik*, **216**, 398 – 410 (1968).

[33] C. Nylander, B. Liedberg, and T. Lind, "Gas detection by means of surface plasmon resonance," Sensors and Actuators, **3**, 79 - 88 (1982).

[34] B. Liedberg, C. Nylander, and I. Lundstrom, "Surface plasmon resonance for gas detection and biosensing," *Sensors and Actuators*, **4**, 299 - 304 (1983).

[35] J. Waswa, J. Irudayaraj, and C. DebRoy, " Direct detection of E. Coli O157:H7 in selected food systems by a surface plasmon resonance biosensor," *Swiss Society of Food Science and Technology*, **40**, 187–192 (2007).

[36] J. Waswa, C. Debroy, and J. Irudayaraj, " Rapid detection of *Salmonella enteritidis* and *Escherichia coli* using surface plasmon resonance biosensor," *Journal of Food Process Engineering*, **29**, 373–385 (2006).

[37] S.-H. Lee, J.-Y. Ahn, K.-A. Lee, H.-J. Uma, S. S. Sekhon, T. S. Park, J. Min, and Y.g-H. Kim, "Analytical bioconjugates, aptamers, enable specific quantitative detection of *Listeria monocytogenes*," *Biosensors and Bioelectronics*, **68**, 272–280 (2015).

[38] H. Chen, Y. Hou, F. Qi, J. Zhang, K. Koh, and Z. Shen, G. Li, "Detection of vascular endothelial growth factor based on rolling circle amplification as a means of signal enhancement in surface plasmon resonance," *Biosensors and Bioelectronics*, **61**,83–87 (2014).

[39] C.-Y. Yang, E. Brooks, Y. Li, P. Denny, C.-M. Ho, F. Qi, W. Shi, L. Wolinsky, B. Wu, D. T. W. Wongbdef, and C. D. Montemagno, "Detection of picomolar levels of interleukin-8 in human saliva by SPR," *Lab on a Chip*, **5**, 1017–1023 (2005).

[40] T. Riedel, C. Rodriguez-Emmenegger, A. S. Pereira, A. Bědajánková, P. Jinoch, P. M. Boltovets, and E. Brynda, "Diagnosis of Epstein–Barr virus infection in clinical serum samples by an SPR biosensor assay," *Biosensors and Bioelectronics*, **55**, 278–284 (2014).

[41] J. He, H. Lai, M, Engle, S. Gorlatov, C. Gruber, H. Steinkellner, M. S. Diamond, and Q. Chen, "Generation and analysis of novel plant-derived antibody-based therapeutic molecules against West Nile Virus," *PLoS ONE*, **9**(3): e93541 (2014).

[42] Y. Lu, Y. Xia, M. Pan, X. Wang, and S. Wang, "Development of a surface plasmon resonance immunosensor for detecting melamine in milk products and pet foods," *Journal of Agriculture and Food Chemistry*, **62**, 12471−12476 (2014).

[43] R. Yatabe, T. Onodera, and K. Toko, "Highly sensitive detection of 2,4,6-trinitrotoluene (TNT) using poly(vinylamine-co-n-vinylformamide)-based surface plasmon resonance (SPR) immunosensor," *Sensors and Materials*, **25**(1), 45–56 (2013).

[44] J. C. Quail, J. G. Rako, and H. J. Simon, "Long-range surface-plasmon modes in silver and aluminum films," *Optics Letters*, **8**(7), 377-379 (1983).

[45] R. Slavík and J. Homola, "Ultrahigh resolution long range surface plasmon-based sensor," *Sensors and Actuators B*, **123**, 10-12 (2007).

[46] M. Vala, S. Etheridge, J. A. Roach, and J. Homola, "Long-range surface plasmons for sensitive detection of bacterial analytes," *Sensors and Actuators B*, **139**, 59–63 (2009).

[47] J. Dostálek, A. Kasry, and W. Knoll, "Long range surface plasmons for observation of biomolecular binding events at metallic surfaces," *Plasmonics*, **2**,97–106 (2007).

[48] A. Khan, O. Krupin, E. Lisicka-Skrzek, and P. Berini, "Mach-Zehnder refractometric sensor using long-range surface plasmon waveguides," *Applied Physics Letters*, **103**, 111108 (1-4) (2013).

[49] M. Weisser, G. Tovar, S. Mittler-Neher, W. Knoll, F. Brosinger, H. Freimuth, M. Lacher, and W. Ehrfeld, "Specific bio-recognition reactions observed with an integrated Mach–Zehnder interferometer," *Biosensors and Bioelectronics*, **14**, 405-411 (1999).

[50] A. Ymeti, J. Greve, P. V. Lambeck, T. Wink, S. Hovell, T. A. M. Beumer, R. R. Wijn, R. G. Heideman, V. Subramaniam, and J. S. Kanger, "Fast, ultrasensitive virus detection using a Young Interferometer sensor," *Nano Letters*, **7**(2), 394-397 (2007).

[51] B. H. Schneider, E. L. Dickinson, M. D. Vach, J. V. Hoijer, and L. V. Howard, "Optical chip immunoassay for hCG in human whole blood," Biosensors and Bioelectronics, **15**, 597–604 (2000).

[52] P. Berini, "Long-range surface plasmon polaritons," *Advances in Optics and Photonics*, **1**, 484–588 (2009).

[53] M. S. Kwon, "Theoretical investigation of an interferometer-type plasmonic biosensor using a metal-insulator-silicon waveguide," *Plasmonics*, **5**, 347–354 (2010).

[54] L. O. Diniz, E. Marega Jr., F. D. Nunes, and B.-H. V. Borges, "A long-range surface plasmon-polariton waveguide ring resonator as a platform for (bio)sensor applications," *Journal of Optics*, **13**, 115001 (7pp) (2011).

[55] Y. H. Joo, S. H. Song, and R. Magnusson, "Long-range surface plasmon-polariton waveguide sensors with a Bragg grating in the asymmetric double-electrode structure," *Optics Expres*s, **17**(13), 10606-10611 (2009).